Low edge safety factor disruptions in the Compact Toroidal Hybrid: Operation in the low-q regime, passive disruption avoidance and the nature of MHD precursors

by

Mihir Divyachakshu Pandya

A dissertation submitted to the Graduate Faculty of
Auburn University
in partial fulfillment of the
requirements for the Degree of
Doctor of Philosophy

Auburn, Alabama
August 6, 2016

Keywords: Compact Toroidal Hybrid (CTH), tokamak-stellarator hybrid, 3-D magnetohydrodynamic (MHD) mode structures, current driven disruptions, low-q disruptions, passive disruption avoidance

Approved by

David A. Maurer, Associate Professor, Department of Physics
Gregory J. Hartwell, Associate Research Professor, Department of Physics
David A. Ennis, Assistant Professor, Department of Physics
James D. Hanson, Professor & Chair, Department of Physics
Allen L. Landers, Professor, Department of Physics

Abstract

The nominally axisymmetric (2-D) magnetic configuration in the form of a tokamak has proven to be the best candidate for a future reactor, and yet it is susceptible to instabilities which lead to a complete loss of the confined plasma. Some of these instabilities are on account of the toroidal plasma current required to establish a magnetic cage to hold the plasma. On the other end of the spectrum is the non-axisymmetric (3-D) magnetic configuration of the stellarators in which the a robust magnetic cage is provided by the external coils, with no need for a plasma current. For the application as a fusion reactor, non-axisymmetric shaping of toroidal plasmas is expected to be incorporated in the design of future experiments (Spong 2015). Small amounts of non-axisymmetric magnetic fields have been used in improving the stability and control of the tokamak plasmas (Spong 2015). The effect of varying amounts of shaping effects in the hybrid configurations of current carrying stellarators, has been demonstrated to suppress unstable magnetohydrodynamic (MHD) modes (W VII-A Team 1980, Hirsch et al. 2008, Atkinson et al. 1976). This thesis presents an understanding of the 3-D structure of the MHD modes observed in the current carrying plasmas of the Compact Toroidal Hybrid (CTH) device. Also presented is the 3-D shaping effect of stellarator fields on the stability of current carrying plasmas.

CTH is a stellarator-tokamak hybrid device designed to investigate the stability of current-carrying plasmas. The magnetic configuration of CTH is non-axisymmetric like that of a stellarator, while on account of a toroidal plasma current, some of the equilibrium properties are similar to that of a tokamak. The flexible CTH magnetic configuration allows varying the amount of 3-D shaping by modifying the twist of the magnetic field lines, known as the rotational transform. In current carrying CTH plasmas when the rotational transform, ι, assumes rational values, fluctuations in equilibrium magnetic field are measured by

the arrays of magnetic probes, some of which were built in the course of the research work presented. These are believed to be associated with specific magnetic flux surfaces inside the plasma, known as rational surfaces. MHD modes that lie on the rational surfaces can drive the confined plasma unstable, especially if they are due to perturbations in the current parallel to the equilibrium magnetic field. Therefore, it is important to understand the structure of these MHD modes detected by the magnetic probes.

The structure of the current driven kink/tearing modes is flute-like, and in the cylindrical geometries their helicity is characterized by the poloidal mode number, m, and the toroidal mode number, n. The interpretation of the structure of these modes is complicated in the toroidal geometry, and even more so in a non-axisymmetric configuration like that of CTH. Information about the plasma equilibrium reconstructed by the V3FIT code (Hanson et al 2009) is used to model these observed MHD modes as helical current filaments within the equilibrium. It has been shown that these MHD modes are indeed a result of helical perturbations within the 3-D plasma equilibrium of CTH, that is their structure is flute-like, and they originate on rational flux surfaces with helicity given by n/m.

Studying the effect of increasing amounts of vacuum rotational transform, that is the rotational transform generated by the external magnet coils, on the stability of current-carrying discharges is an important research topic on CTH. A kink/tearing mode instability constrains the amount of plasma current that can be driven in a tokamak; with the edge safety factor constrained to values greater than two, $q(a) > 2$ (Wesson 2011). The edge safety factor value is inversely proportional to the plasma current. CTH discharges can operate without loss of confinement, even if $q(a) < 2$, if sufficient amounts of 3-D shaping is applied. It is observed that increasing the amount of 3-D shaping by 10% is sufficient to successfully stabilize the CTH discharges operating in the low edge safety factor regime. Additionally, it is observed with the magnetic probes that the unstable modes implicated in the loss of confinement, have mode structures characterized by $m/n = 3/2$, and $4/3$.

Acknowledgments

I would like to begin by expressing my deep gratitude to Prof. David Maurer for guiding me through more than five years of research. He has been very accessible in spite of his tight schedule, helping me prepare for presentations within our group, APS meetings, and job interview. His intuition of physics has been instrumental in the success of my project, and I hope that I've imbibed some of it. The work I've done in the CTH lab would not have been as fruitful without help of Prof. Greg Hartwell who has patiently supported me in my projects, fixed the things I've broken, and made suggestions (lots of them) to improve my thesis. I thank Prof. David Ennis for discussions on my research, and for his suggestions to improve my thesis. I am grateful to Prof. Stephen Knowlton for presenting me with the opportunity of carrying out research on the CTH experiment.

The eight years of graduate school have been smooth partly because of the great staff of the physics department led by Freddie Killian. I also thank John Dawson for making all my electronics work. The support of fellow CTHers, Jeffery Herfindal, Peter Traverso, Matthew ArchMiller, and Xinxing Ma, has been amazing. Thank you guys for running the machine, discussing physics, and of course helping me wind all those solenoids. Ami DuBois, Yogesh Sharma, and Aaron Modic, you all have been very supportive during my time at Auburn.

Thank you Mummy and Papa for standing by me not just these past few years, but also taking all the responsibilities that you've throughout my life to ensure my well being and comfort. I love you. Hershal, more than my little brother, you have been my inspiration all my life! Pavani, thank you for your support, and for marrying Hershal; I may not have met Mansi otherwise! Laxmandada in our last conversation you had told me that there's no way around hard work; I miss you every time I think about that day and of all the stories you used to tell with us sitting on that dining table. Dadaji and Mummyba, thank you for

making path for my tricycle around your house, and for sharing your love and care; I wish I had spent more time with you. Minoo, you have never left; yet, you will always be missed.

My life wouldn't have been the same without you, Mansi. Thank you for being patient, understanding of my occupied mind, and yet pushing me to do better. You of all people know better how this thesis was put together. I love you!

Table of Contents

List of Figures

List of Tables

List of Abbreviations and common Symbols

ι	Rotational transform
$\iota_{tot}(a)$	Rotational transform at the edge of plasma with ohmically driven plasma current. It has contribution from external stellarator fields and the driven plasma current.
$\iota_{vac}(a)$	Rotational transform at the edge in the stellarator phase of CTH in which no plasma current is driven.
I_{p}	Plasma current
n_e	Plasma density
q(a)	Safety factor at the plasma edge
CTH	Compact Toroidal Hybrid
ECRH	Electron Cyclotron Resonance Heating
LCFS	Last Closed Flux Surface
MHD	Magnetohydrodynamics
SXR	Soft X-rays

Chapter 1

Introduction

Thermonuclear fusion research today is carried out with the end goal of achieving controlled steady state fusion reactions to generate electric power. The fusion process involves the merging of light elements such as hydrogen and its isotopes, deuterium (D) and tritium (T). All the stars in the universe, including the sun, are powered by fusion. On the earth, controlled thermonuclear fusion offers the possibility of abundant, environment friendly and safe power.[1] Presently D-T fusion is considered to be of primary interest due to its suitability in production of electricity. The result of D-T fusion reaction is one α-particle (helium nucleus), one neutron, and 17.6 MeV of energy, most of which is carried by this neutron. Energy from neutron has to captured, and transformed into heat, to replacing the heat provided by the fossil fuels in the majority of power plants today, after which this heat is transformed into electricity.

The nuclei of deuterium and tritium must overcome the repulsive electrostatic force before their stored nuclear energy can be tapped. Fusion fuel when heated to high temperatures transforms to the plasma state, and can gain enough energy to fuse together. The plasma being electrically conducting can be confined, and controlled, using magnetic fields to achieve conditions necessary for plasma ignition, that is to say, no external heating sources are required to sustain fusion reactions. The Lawson criterion[2] for an ignited fusion reaction states that the product of density, n, and the energy confinement time, τ_E, must exceed a critical value in the range of, $2-5\times10^{20}\,\mathrm{m}^{-3}\,\mathrm{s}$, with the temperature in the range, $10-20\,\mathrm{keV}$.[3] The energy confinement time can be experimentally determined as ratio of the total plasma energy, W, and the supplied input heating power P_{H}.[3] The total energy stored in the plasma volume, V, at temperature, T, and density n, is given by $W = 3nTV$.[3] The

success of building a fusion reactor depends on achieving a triple product beyond its critical value of,[3]

$$n\tau_E T > 5 \times 10^{21}\,\mathrm{m}^{-3}\,\mathrm{s\,keV}. \tag{1.1}$$

Since early 1950s, significant progress has been made in achieving this goal, with thermonuclear power of more than sixty percent of the input power being generated.[3] Among all the magnetic configurations that have been explored for plasma confinement, the best performance has been achieved in a tokamak.[1] The prominent concepts of plasma confinement being explored today are, the tokamak, stellarator, reverse field pinch, spheromak, field reversed configuration, and the levitated dipole.[1] All of these configurations confine the plasma in a toroidal geometry, and each of them, except the stellarator are axisymmetric, two dimensional (2D) configurations. The stellarator is an inherently non-axisymmetric (3D) configuration.[1] The work presented in this dissertation is performed on the Compact toroidal Hybrid (CTH) device, a stellarator-tokamak hybrid, so physics pertinent to this thesis, concerning a tokamak and a stellarator, will be discussed in this chapter.

The confining force of the magnetic field is perpendicular to the motion of a charged particle, and is given by the Lorentz force, $\mathbf{F} = q(\mathbf{v} \times \mathbf{B})$. In tokamaks and stellarators, the plasma is confined by the application of toroidal and poloidal magnetic fields. The toroidal geometry frequently referred to in this thesis is shown in the figure 1.1. The increments in toroidal or azimuthal angle, φ, and poloidal angle, θ, are indicated by arrows. R is the major radius of the torus, and r is the radius of poloidal cross-section of the torus. The Z-direction is along the axis normal to the plane of the torus. In tokamaks, the confining toroidal magnetic field is supplied by external electromagnetic coils, while most of the poloidal magnetic field is generated by plasma current driven by a voltage in toroidal direction. In a stellarator however, the poloidal and toroidal magnetic fields are generated by external magnet coils.

Equilibrium and stability of plasma are necessary requirements for any plasma confinement scheme. The magnetohydrodynamic (MHD) model is a fluid model that describes the macroscopic equilibrium and stability properties of a plasma. Ideal MHD is the simplest

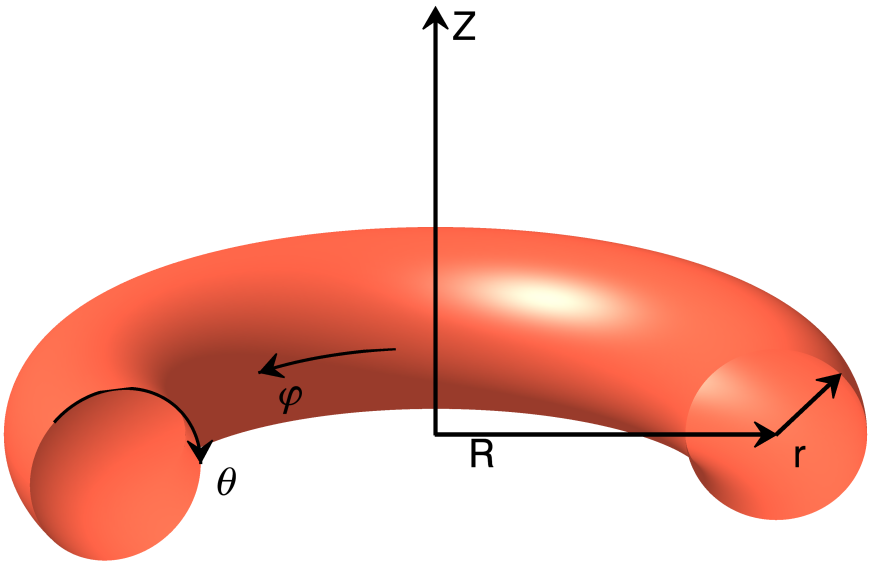

Figure 1.1: Toroidal geometry is used in plasma confinement. R is the major radius of the torus, r is the minor radius, θ is the poloidal angle and ϕ is the toroidal angle. Z-axis is vertical, and normal to the horizontal plane of the torus.

version of it, where the plasma is represented by single fluid with infinite conductivity and zero ion gyro radius.[4] The ideal MHD theory is explained in detail in the book by Freidberg[4]. According to the MHD theory, the magnetic field lines lie on a set of closed nested flux surfaces, which follows from the momentum equation, given by,[4]

$$\rho \frac{d\mathbf{v}}{dt} = \mathbf{J} \times \mathbf{B} - \nabla p, \tag{1.2}$$

where ρ is the mass density, $\mathbf{v}$ is the fluid velocity of the plasma, $\mathbf{J}$ is the current density, $\mathbf{B}$ is the magnetic field, and p is the plasma pressure. In a static MHD equilibrium, the left hand side of the equation is zero as no force is acting on the plasma, and thus,

$$\mathbf{J} \times \mathbf{B} = \nabla p. \tag{1.3}$$

Taking the dot product of the above equation with $\mathbf{B}$ gives,

$$\mathbf{B} \cdot \nabla p = 0. \tag{1.4}$$

This implies that the magnetic field must be tangential to the contours of constant pressure. The pressure is maximum at the center of a poloidal cross-section, and decreases as we move outwards. The only topological shape that satisfies the equation 1.4 is a torus.[5] For such pressure profiles, the contours of constant pressure are nested toroidal surfaces as shown in the figure 1.2. These contours are usually referred to as magnetic flux surfaces, and the limiting flux surface, which approaches single magnetic field line, is called magnetic axis.[4]

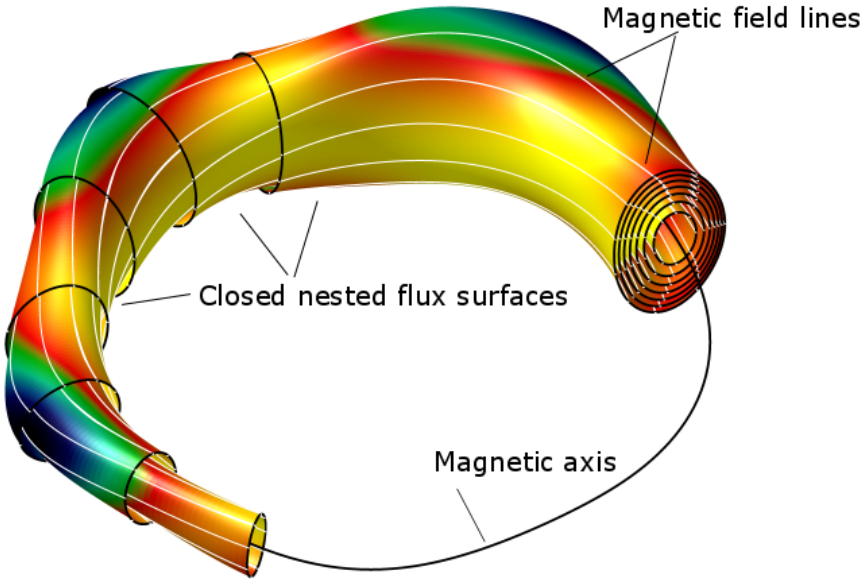

Figure 1.2: Model of magnetic field lines on closed nested flux surfaces in CTH.

The trajectories of magnetic field lines define three classes of magnetic flux surfaces: rational, ergodic, and stochastic. If the magnetic field lines on a flux surfaces close on themselves after finite number of toroidal circuits, then the surface is known as a rational surface. If the magnetic field lines remain on the toroidal surface as it makes infinite number of toroidal transits, but never close upon themselves, then the flux surface is known as an ergodic surface. For the formation of a closed magnetic rational surface an infinite number of field lines are required, whereas on an ergodic surface, a single filed line will define the surface. In the case where the field line does not remain on a surface, but fills the entire volume then the resulting region is stochastic.[4] The rational and ergodic types of flux surfaces, can be characterized in terms of rotational transform. Rotational transform is a

measure of twistedness of the magnetic field line, defined as the average change in poloidal angle, $\langle \Delta\theta \rangle$, after an infinite number of toroidal transits:[4]

$$\iota = \lim_{N\to\infty} \frac{1}{N} \sum_{1}^{N} \frac{\Delta\theta}{2\pi}. \tag{1.5}$$

The factor of 2π is the change in toroidal angle, $\Delta\phi = 2\pi$ for a single transit of the magnetic field line. If the magnetic field line makes n poloidal transits, for every m toroidal transits, then rotational transform, is also given by,

$$\iota = \frac{n}{m}, \tag{1.6}$$

where, if n and m are integers, the magnetic field line lies on a rational surface, otherwise, it lies on an ergodic flux surface. In tokamak research, the twistedness of the magnetic field lines is expressed in terms of the reciprocal of the rotational transform, and is termed as the safety factor, q,

$$q = \frac{1}{\iota}. \tag{1.7}$$

Earlier, we identified a flux surface as a contour of constant pressure, therefore the pressure is termed as a surface quantity. The poloidal and toroidal fluxes are two other surface quantities that are constant on a flux surface. The poloidal and toroidal fluxes, Ψ_p and Ψ_t, are is defined as,

$$\begin{aligned} \Psi_p &= \int \mathbf{B} \cdot d\mathbf{S}_p, \\ \Psi_t &= \int \mathbf{B} \cdot d\mathbf{S}_t, \end{aligned} \tag{1.8}$$

where, $d\mathbf{S}_p$ and $d\mathbf{S}_t$ are the surface elements, with their respective area-normals pointing along the poloidal and toroidal directions. Both Ψ_p and Ψ_t can be used to label a given flux surface. The rotational transform can alternately be shown to be reduce to a ratio of these

fluxes and can be written as,[4]

$$\iota = \frac{d\Psi_p}{d\Psi_t}. \tag{1.9}$$

The rotational transform derived for a screw pinch, the magnetic configuration that confines plasma in a straight cylinder with poloidal and toroidal magnetic fields, is often used to gain intuition of the effect of changing magnetic fields. The rotational transform on the surface of the plasma is given by,[4]

$$\iota(a) = \frac{R_0 B_\theta(a)}{r B_z(a)} = \frac{1}{q(a)} \tag{1.10}$$

where, the length of the cylinder is $2\pi R_0$, a is the minor radius of the plasma, $B_\theta(a)$ is the poloidal magnetic field, $B_z(a)$ is the magnetic field along the axis of the cylinder, and q is the safety factor at the edge defined earlier in equation 1.7. The poloidal magnetic field at the edge of the plasma due to the current, I, flowing along the axis of the cylinder can be computed from Ampere's law, $B_\theta = \mu_0 I/2\pi a$, therefore the rotational transform can be expressed in terms of axial current,

$$\iota(a) = \frac{\mu_0 R_0 I}{2\pi a^2 B_z(a)} = \frac{1}{q(a)}. \tag{1.11}$$

Thus the rotational transform, is proportional to the axial plasma current, which in toroidal plasmas can be replaced with the toroidal plasma current. An important difference between a tokamak and a stellarator is in the way they derive their rotational transform. As mentioned earlier, the poloidal magnetic field in a tokamak is derived from a toroidal plasma current, and this gives rise to the rotational transform. In a stellarator, the rotational transform is entirely derived from the magnetic fields supplied by external coils, and in this dissertation, it will be referred to as vacuum rotational transform, ι_{vac}. In the case tokamak case, $\iota_{\text{vac}} = 0$.

A tokamak equilibrium is subject to MHD instabilities which can lead to sudden loss of plasma confinement known as a disruption. In tokamaks a disruption may occur due to either violation of an operational stability limit or due to technical failures in systems associated with machine or plasma control. The disruption-free operation of a tokamak is

limited with regard to maximum plasma current, maximum electron density and maximum plasma pressure normalized to the magnetic field , $\beta = 2\mu_0 < p > /B^2$.[6] The current limit, also known as the low edge safety factor limit or the low-q limit, restricts the operation of tokamak to an edge safety factor greater than two, $q(a) > 2$, thereby restricting the amount of plasma current achievable for a given toroidal magnetic field (see Eq.1.11). In general, stellarators are not subject such current driven instabilities due to absence of externally driven plasma current.

Another difference between a stellarator and a tokamak is the shape of their equilibrium flux surfaces. The flux surfaces of a tokamak are nominally axisymmetric, that is, their shape is independent of the toroidal angle, φ, whereas stellarator flux surfaces are non-axisymmetric by design. The shape of last closed flux surface for an axisymmetric tokamak plasma, and non-axisymmetric CTH plasma is shown in the figure 1.3. The shape of the plasma is an

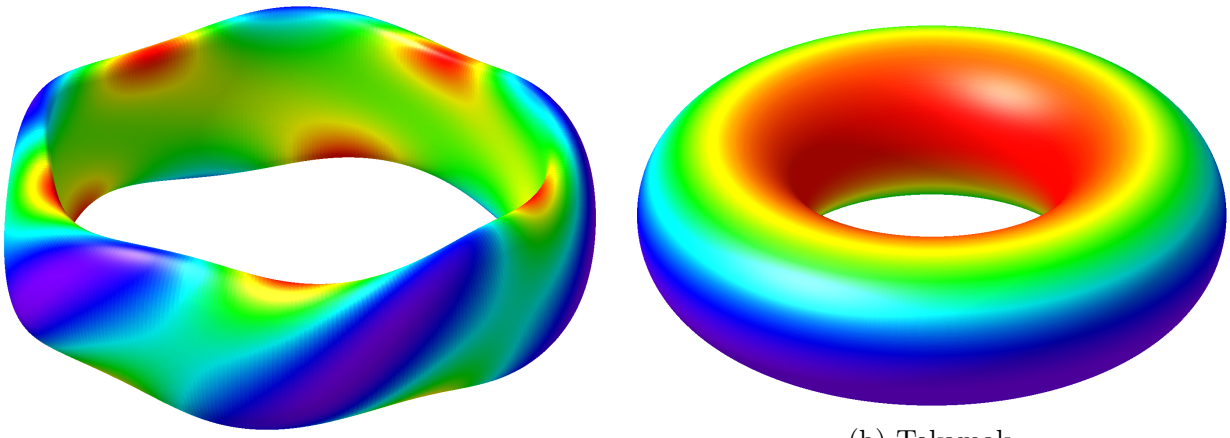

(a) CTH

(b) Tokamak

Figure 1.3: Comparison of non-axisymmetric flux surfaces of (a) CTH stellarator, and the axisymmetric case of (b) tokamak. The colors indicate magnitude of the magnetic field, $\mid B \mid$.

important parameter that determines the stability in tokmaks[7,8]. To mitigate instabilities such as edge localized modes[9,10] and resistive wall modes[11,12], non-axisymmetric magnetic fields are applied to the axisymmetric tokamak equilibrium. The magnitude of these non-axisymmetric fields, B_{3D}, in comparison to the axisymmetric toroidal field, B_0, is small,

$B_{3D}/B_0 \sim 10^{-3}$. Recent theoretical work in this area suggests that some form 3D magnetic field structure is expected in the design of future steady state reactors.[13–16] Stellarator fields are highly non-axisymmetric with the deviation from axisymmetry being on the order of, $B_{3D}/B_0 \sim 10^{-1}$. So, a natural question could be, can intermediate levels of non-axisymmetric fields provide a greater stability than a tokamak plasma? This question can be answered by hybrid magnetic configurations, where a toroidal plasma current can be driven on the flux surfaces of a stellarator equilibrium. Indeed, experiments on current-carrying stellarators have shown improved stability with increasing levels of stellarator rotational transform.[17–19]

CTH device is a stellarator-tokamak hybrid designed to investigate effect of 3-D shaping on current driven instabilities.[20] This dissertation presents research carried out in the current-carrying CTH discharges, and is summarized as follows:

- In the current-carrying plasmas of CTH, strong MHD activity is measured by the magnetic pickup probes when the edge rotational transform, $\iota(a)$, is near rational values. First measurements of the MHD mode structures, using poloidal and toroidal arrays of these probes are presented in this dissertation.

- In cylindrical geometries kink/tearing modes have a flute like structure, which can be expressed in terms of a helical perturbation, $\xi(\mathbf{r}) = \xi_0(r)\ \exp\ i(m\theta + n\phi)$, where m is the poloidal mode number, and n is the toroidal mode number. The interpretation of structure of MHD modes is complicated in a toroidal geometry, and even more so in an non-axisymmetric configuration like that of CTH. The information about the plasma equilibrium reconstructed by the V3FIT code[21] is used to model observed MHD modes as helical current filaments on rational surfaces. Such a model enables interpretation of the MHD modes in terms of Fourier harmonics, m, and n, like in cylindrical plasmas. Results presented for MHD modes with helicities, $m/n =$, 3/2, 4/1, 3/1, and 2/1 show that these modes are indeed flute-like.

- A study is performed to understand the effect of increasing stellarator transform on low edge safety factor disruptions. Current driven kink/tearing mode with the structure, $m = 2/n = 1$, is responsible for low edge safety factor tokamak plasmas, limiting the operation to $q(a) > 2$.[3] In contrast, the current-carrying discharges in CTH are observed to operate disruption-free when the edge safety factor is less than two, $q(a) < 2$, with the addition of a sufficient external rotational transform.[22] When the plasma does disrupt, the MHD precursors implicated in the low edge safety factor disruptions have mode numbers, m/n=3/2, and 4/3 observed on the magnetic probes, and $m/n = 1/1$ activity observed on core soft x-ray emissivity measurements.

The outline of this dissertation is as follows: Chapter 2 describes the magnetic configuration of CTH, along with the diagnostics on CTH that are used for determining the equilibrium, and for measuring fluctuations of magnetic field. Chapter 3 highlights the difficulty in determining the MHD mode numbers in toroidal plasmas, and develops the biorthogonal decomposition technique to identify the MHD modes observed in the current-carrying CTH discharges. Chapter 4 discusses the modeling of these MHD modes as helical current filaments on rational surfaces of the equilibrium. Chapter 5 gives a description of the generic disruption phenomenon, the low edge safety factor disruptions observed in tokamaks, and demonstrates the suppression of low edge safety factor disruptions with increasing amounts of stellarator transform supplied by the external coils of CTH. Chapter 6 provides a summary and discussion of the major results with possible extensions to the presented work.

References

[1] J. Freidberg. *Plasma Physics and Fusion Energy.* Cambridge University Press, 1st edition, 2007.

[2] J D Lawson. Some criteria for a power producing thermonuclear reactor. *Proceedings of the Physical Society. Section B*, 70(1):6, 1957.

[3] John Wesson. *Tokamaks.* Oxford University Press, 4th edition, 2011.

[4] J. Freidberg. *Ideal MHD.* Cambridge University Press, 2014.

[5] Allen H. Boozer. Physics of magnetically confined plasmas. *Rev. Mod. Phys.*, 76:1071–1141, Jan 2005.

[6] T.C. Hender, J.C Wesley, J. Bialek, A. Bondeson, A.H. Boozer, R.J. Buttery, A. Garofalo, T.P Goodman, R.S. Granetz, Y. Gribov, O. Gruber, M. Gryaznevich, G. Giruzzi, S. Gnter, N. Hayashi, P. Helander, C.C. Hegna, D.F. Howell, D.A. Humphreys, G.T.A. Huysmans, A.W. Hyatt, A. Isayama, S.C. Jardin, Y. Kawano, A. Kellman, C. Kessel, H.R. Koslowski, R.J. La Haye, E. Lazzaro, Y.Q. Liu, V. Lukash, J. Manickam, S. Medvedev, V. Mertens, S.V. Mirnov, Y. Nakamura, G. Navratil, M. Okabayashi, T. Ozeki, R. Paccagnella, G. Pautasso, F. Porcelli, V.D. Pustovitov, V. Riccardo, M. Sato, O. Sauter, M.J. Schaffer, M. Shimada, P. Sonato, E.J. Strait, M. Sugihara, M. Takechi, A.D. Turnbull, E. Westerhof, D.G. Whyte, R. Yoshino, H. Zohm, Disruption the ITPA MHD, and Magnetic Control Topical Group. Chapter 3: MHD stability, operational limits and disruptions. *Nuclear Fusion*, 47(6):S128, 2007.

[7] L.L. Lao, J.R. Ferron, R.L. Miller, T.H. Osborne, V.S. Chan, R.J. Groebner, G.L. Jackson, R.J. La Haye, E.J. Strait, T.S. Taylor, A.D. Turnbull, E.J. Doyle, E.A. Lazarus, M. Murakami, G.R. McKee, B.W. Rice, C. Zhang, and L. Chen. Effects of plasma shape and profiles on edge stability in DIII-D. *Nuclear Fusion*, 39(11Y):1785, 1999.

[8] A Scarabosio, A Pochelon, and Y Martin. Plasma shape stabilization of current rise MHD instabilities in TCV. *Plasma Physics and Controlled Fusion*, 49(7):1041, 2007.

[9] T. E. Evans, R. A. Moyer, P. R. Thomas, J. G. Watkins, T. H. Osborne, J. A. Boedo, E. J. Doyle, M. E. Fenstermacher, K. H. Finken, R. J. Groebner, M. Groth, J. H. Harris, R. J. La Haye, C. J. Lasnier, S. Masuzaki, N. Ohyabu, D. G. Pretty, T. L. Rhodes, H. Reimerdes, D. L. Rudakov, M. J. Schaffer, G. Wang, and L. Zeng. Suppression of large edge-localized modes in high-confinement DIII-D plasmas with a stochastic magnetic boundary. *Phys. Rev. Lett.*, 92:235003, Jun 2004.

[10] Y. Liang, H. R. Koslowski, P. R. Thomas, E. Nardon, B. Alper, P. Andrew, Y. Andrew, G. Arnoux, Y. Baranov, M. Bécoulet, M. Beurskens, T. Biewer, M. Bigi, K. Crombe, E. De La Luna, P. de Vries, W. Fundamenski, S. Gerasimov, C. Giroud, M. P. Gryaznevich, N. Hawkes, S. Hotchin, D. Howell, S. Jachmich, V. Kiptily, L. Moreira, V. Parail, S. D. Pinches, E. Rachlew, and O. Zimmermann. Active Control of Type-I Edge-Localized Modes with $n = 1$ Perturbation Fields in the JET Tokamak. *Phys. Rev. Lett.*, 98:265004, Jun 2007.

[11] M. Okabayashi, J. Bialek, A. Bondeson, M.S. Chance, M.S. Chu, A.M. Garofalo, R. Hatcher, Y. In, G.L. Jackson, R.J. Jayakumar, T.H. Jensen, O. Katsuro-Hopkins, R.J. La Haye, Y.Q. Liu, G.A. Navratil, H. Reimerdes, J.T. Scoville, E.J. Strait, M. Takechi, A.D. Turnbull, P. Gohil, J.S. Kim, M.A. Makowski, J. Manickam, and J. Menard. Control of the resistive wall mode with internal coils in the diiid tokamak. *Nuclear Fusion*, 45(12):1715, 2005.

[12] S.A. Sabbagh, J.W. Berkery, R.E. Bell, J.M. Bialek, S.P. Gerhardt, J.E. Menard, R. Betti, D.A. Gates, B. Hu, O.N. Katsuro-Hopkins, B.P. LeBlanc, F.M. Levinton, J. Manickam, K. Tritz, and H. Yuh. Advances in global MHD mode stabilization research on NSTX. *Nuclear Fusion*, 50(2):025020, 2010.

[13] D A Spong. 3D toroidal physics: Testing the boundaries of symmetry breaking. *Physics of Plasmas*, 22(5):055602–1, 2015.

[14] Allen H. Boozer. Use of nonaxisymmetric shaping in magnetic fusion. *Physics of Plasmas*, 16(5), 2009.

[15] Long-Poe Ku and Allen Boozer. Nonaxisymmetric shaping of tokamaks preserving quasiaxisymmetry. *Physics of Plasmas*, 16(8):082506, 2009.

[16] Allen H Boozer. Stellarators and the path from iter to demo. *Plasma Physics and Controlled Fusion*, 50(12):124005, 2008.

[17] W VII-A Team. Stabilization of the (2, 1) tearing mode and of the current disruption in the W VII-A stellarator. *Nuclear Fusion*, 20(9):1093, 1980.

[18] M. Hirsch, J. Baldzuhn, C. Beidler, R. Brakel, R. Burhenn, A. Dinklage, H. Ehmler, M. Endler, V. Erckmann, Y. Feng, J. Geiger, L. Giannone, G. Grieger, P. Grigull, H-J Hartfuß, D. Hartmann, R. Jaenicke, R. König, H. P. Laqua, H. Maaßberg, K. McCormick, F. Sardei, E. Speth, U. Stroth, F. Wagner, A. Weller, A. Werner, H. Wobig, S. Zoletnik, and for the W7-AS Team. Major results from the stellarator Wendelstein 7-AS. *Plasma Physics and Controlled Fusion*, 50(6):053001, 2008.

[19] D. W. Atkinson, A. N. Dellis, R. D. Gill, D. J. Lees, W. Millar, B. A. Powell, P. A. Shatford, and D. R. A. Webb. Comparison between tokamak and ohmically heated stellarator plasmas. *Phys. Rev. Lett.*, 37:1616–1619, Dec 1976.

[20] J. D. Hanson, S. F. Knowlton, B. A. Stevenson, and G. J. Hartwell. Equilibrium and stability of current-carrying discharges in the non-axisymmetric cth experiment. *Contributions to Plasma Physics*, 50(8):724, 2010.

[21] J D Hanson, S. P. Hirshman, S F Knowlton, L.L. Lao, E.A. Lazarus, and J. M. Shields. V3FIT: a code for three-dimensional equilibrium reconstruction. *Nuclear Fusion*, 49(7):075031, 2009.

[22] M. D. Pandya, M. C. ArchMiller, M. R. Cianciosa, D. A. Ennis, J. D. Hanson, G. J. Hartwell, J. D. Hebert, J. L. Herfindal, S. F. Knowlton, X. Ma, S. Massidda, D. A. Maurer, N. A. Roberds, and P. J. Traverso. Low edge safety factor operation and passive disruption avoidance in current carrying plasmas by the addition of stellarator rotational transform. *Physics of Plasmas*, 22(11), 2015.

Chapter 2

The Compact Toroidal Hybrid experiment

2.1 Introduction

The Compact Toroidal Hybrid (CTH) is a torsatron-tokamak hybrid, in which a closed, nested flux-surface equilibrium can be generated solely with external magnetic field coils. In addition, CTH has a central solenoid, that when energized can drive a plasma current in the pre-established equilibrium. A combination of these externally and internally generated magnetic fields provides the rotational transform necessary for confinement. Rotational transform and its radial variation, or shear, are fundamental parameters that affect the stability of toroidal plasmas. A wide variety of magnetic configurations can be obtained in CTH by varying the ratio of rotational transform from the external stellarator coils to that generated by internal plasma current. This flexible magnetic configuration of CTH is designed to investigate the stability of three-dimensional current-carrying plasmas.

An overview of the CTH magnetic configuration is presented in section 2.2, and magnetic diagnostics is presented in section 2.3. The structure of magnetic fluctuations observed in CTH has been analyzed in this thesis using five arrays of pickup coils, one of which was built as part of this work. The design, construction and calibration of these pick-up coils is presented in section 2.3.1. Details of equilibrium reconstruction relevant to this dissertation are presented in section 2.4.

2.2 CTH magnetic configuration

CTH is low aspect ratio five-field period torsatron with ten auxiliary toroidal field coils to vary the vacuum rotational transform. CTH is termed a torsatron type of stellarator because

Parameter	Dimension
Major radius (R_0)	0.75 m
Inner vacuum vessel radius (a_{vessel})	0.29 m
Toroidally averaged B-field along the magnetic axis (B_0)	0.64 T
Input ECRH heating	$\leq$ 15 kW
Input OH heating	100 kW
Average plasma minor radius (a_0)	0.2 m
Line-averaged density (n_e)	$\leq 5.0 \times 10^{19}\,\text{m}^{-3}$
Electron temperature (T_e)	$\leq$ 200 eV

Table 2.1: Major parameters of the CTH design and operation

its primary magnetic field is generated by a single helical field coil that carries current in only one direction.[1] The vacuum vessel is a torus having a major radius of $R_0 = 0.75\,\text{m}$, and a circular cross-section of minor radius $a_{\text{vessel}} = 0.29\,\text{m}$, giving a design aspect ratio of $R_0/a_{\text{vessel}} = 2.6$. The average plasma radius in CTH is about $a_0 = 0.2\,\text{m}$ and so the plasma aspect ratio is approximately $R_0/a_0 \sim 4$. Major CTH design and operation parameters are listed in table 2.1.

The CTH magnetic configuration is generated by the six, independently controlled, magnet coil sets shown in figure 2.1. The primary magnetic field generating coil is a single, 96-turn, continuously wound helical field (HF) coil. The HF coil has a toroidal periodicity of $\ell = 2$, so it makes two toroidal circuits, and $N_p = 5$, that is, it makes five poloidal circuits as it encloses the vacuum vessel. Like other torsatrons, in order to obtain closed vacuum flux surfaces, an additional vertical field is required. The flux surfaces obtained with only the external magnetic coils are referred to as vacuum flux surfaces. In the case of CTH, this vertical field is provided by the main vertical field (MVF) coil that is electrically in series with the HF. A pair of trim vertical field (TVF) coils, provide radial position control of the magnetic axis. A set of toroidal field (TF) coils are used to add to, or subtract from, the toroidal component of the HF field, giving the ability to change the rotational transform over a wide range. A shaping vertical field (SVF) coil set provides a quadrupole field for controlling the vertical elongation and shear of the plasma, and a radial field (RF) coil set

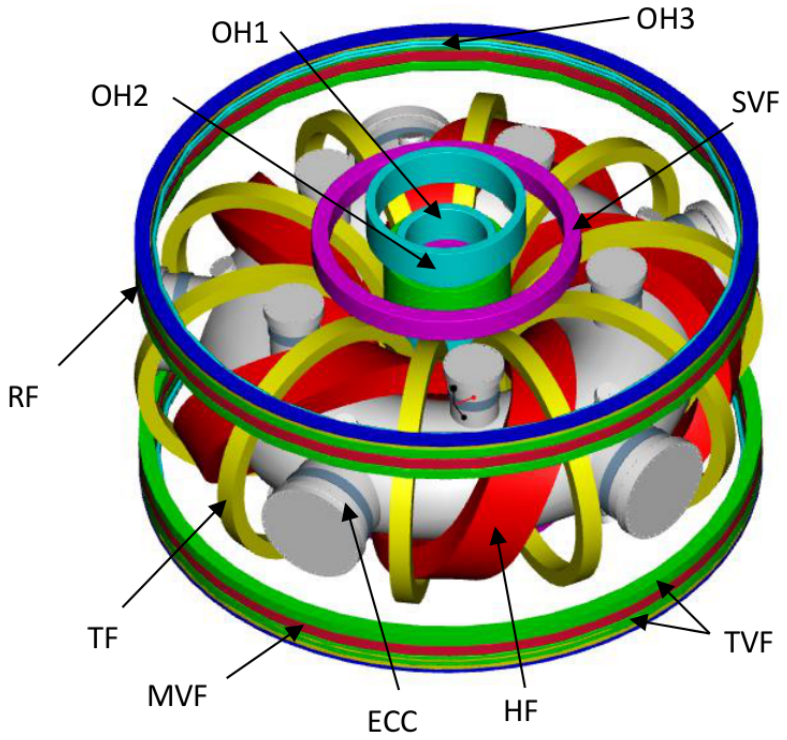

Figure 2.1: Closed magnetic flux surfaces are produced in CTH using the helical field coil (HF), the main vertical field (MVF) coil which is in series with HF, and the trim vertical field (TVF) coil. The TVF also controls the horizontal position of the magnetic axis. Toroidal field (TF) coils generate a toroidal field which either adds or subtracts from the field produced by the HF to give different values of vacuum rotational transform. The vertical elongation and shear are controlled by the shaping vertical field (SVF) coil whereas vertical position of the magnetic axis is controlled by the radial field (RF) coil. The ohmic (OH) coil in the center stack is used to drive toroidal current in the plasma. The poloidal field coil packs shown on top and bottom of the figure are identical.

is used for controlling the vertical position of the plasma. Lastly, an ohmic heating (OH) solenoid is used to induce voltages in the toroidal direction to drive plasma current in the pre-established stellarator equilibria.

The HF coil was wound to ensure existence of closed magnetic flux surfaces within the CTH vacuum vessel.[2,3] The nested, closed magnetic surfaces within the CTH vacuum equilibrium are field-periodic, that is to say that cylindrical coordinates describing the magnetic

flux surfaces have the property,[4]

$$[R(s,u,v), Z(s,u,v)] \leftrightarrow \left[R\left(s,u,v+\frac{2\pi N}{N_p}\right), Z\left(s,u,v+\frac{2\pi N}{N_p}\right)\right] \tag{2.1}$$

where s, u and v specify the location of a point in the flux coordinate system, a coordinate system used in plasma physics to describe closed nested flux surfaces.[5] The coordinate s is a radial-like coordinate that is constant on a flux surface, u is a poloidal angle like coordinate and v is the same as the geometric toroidal angle. In the equation above, N is any integer and $N_p = 5$ for CTH, thus making the CTH magnetic configuration five fold symmetric. This five fold symmetry is on account of the fact that the HF coil is wound to make a total of five poloidal rotations. In addition, CTH possesses stellarator symmetry, in that, $[R(s,u,v), Z(s,u,v)] \leftrightarrow [R(s,u,v), -Z(s,u,-v)]$.

The vacuum magnetic field configuration of CTH is referenced by the value of vacuum rotational transform at the last closed flux surface, $\iota_{\rm vac}(a)$, and can be varied within the range $0.02 \leq \iota_{\rm vac}(a) \leq 0.4$. Since, $\iota \propto B_\theta/B_\phi$, adding or subtracting the toroidal field supplied by the TF coil to the helical field from the HF coil, adjusting the ratio of the currents in the TF, and the HF coils changes the rotational transform of the system. Rotational transform profiles obtained for different ratios of currents in the TF and HF coils, $\mathrm{I_{TF}/I_{HF}}$, are shown in figure 2.2. These profiles are obtained with equilibrium reconstructions of CTH equilibria which is described later in the section 2.4. When the current ratio is negative, indicated by solid lines in the figure, the magnetic field produced by the TF coil adds to the toroidal field component of the HF coil, lowering the rotational transform profile. When the ratio is positive, indicated by dashed lines, the field from the TF coil subtracts from the HF coil increasing the transform. The dotted line indicates zero TF coil current in Fig.2.2.

In addition to the flexibility of the vacuum configuration, CTH can substantially change the vacuum fields by the addition of induced plasma current. In a typical CTH discharge, nested closed magnetic flux surfaces are first obtained with appropriate fields from the main

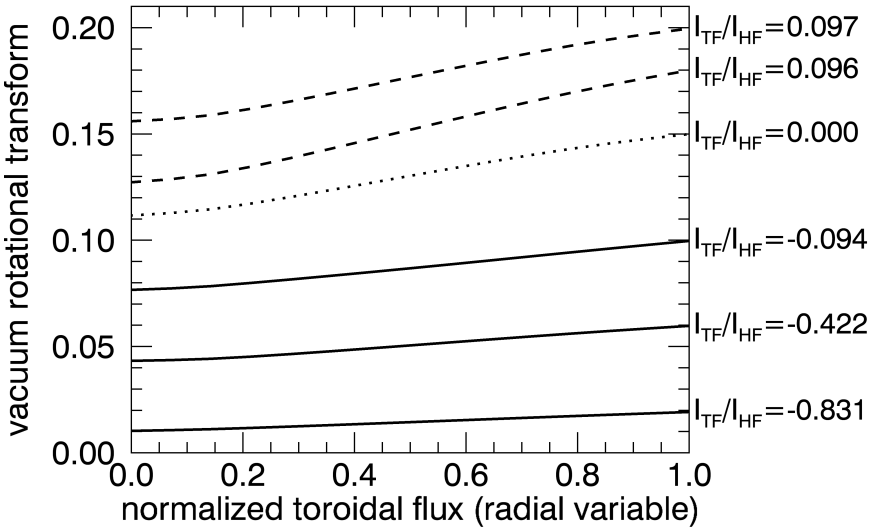

Figure 2.2: Vacuum rotational transform profiles in CTH are obtained by varying the ratio of currents in the TF and HF coils, I_{TF}/I_{HF}. The rotational transform values at different radial locations is shown for each value of I_{TF}/I_{HF}. The normalized toroidal flux is 1 at the last closed flux surface and 0 at the magnetic axis. The current ratio is negative, indicated by solid lines in the figure, if the magnetic field produced by TF adds to the total toroidal field component of HF. The positive TF current is indicated by dashed lines, and dotted line indicates zero TF current.

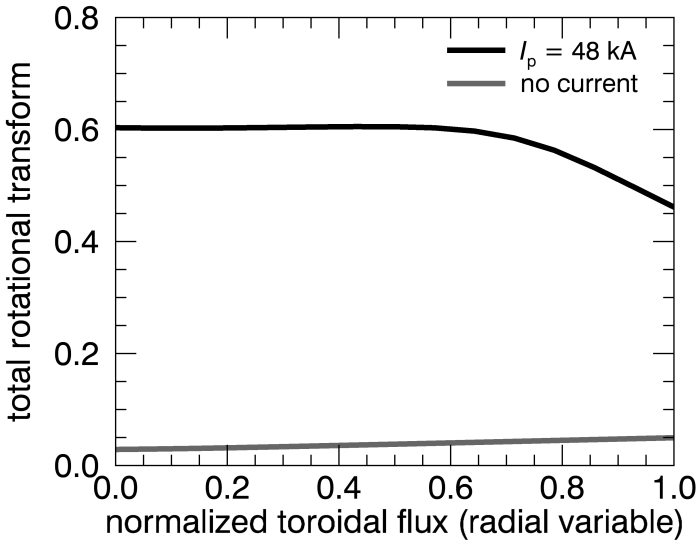

Figure 2.3: The toroidal plasma current strongly modifies the rotational transform profile of CTH equilibrium. The vacuum rotational transform profile, shown in gray, is monotonically increasing with $\iota_{\rm vac}(a) \sim 0.05$. With toroidally driven plasma current the rotational transform profile is monotonically decreasing, tokamak like, with $\iota_{\rm tot}(\rm a) \sim 0.45$.

magnet coils. Next, a hydrogen plasma is produced in this magnetic configuration by electron cyclotron resonance heating (ECRH). This is what is referred to as "pure" stellarator plasma. In this stellarator equilibrium, a large toroidal loop voltage is inductively applied with the OH coil, resulting in a toroidally driven plasma current, giving rise to the hybrid phase of the discharge. The resulting rotational transform thus has contributions from both the vacuum field and the poloidal field generated by the toroidal plasma current, $I_{\rm p}$ (recall that $\iota \propto B_\theta/B_\phi$ and $B_\theta \propto I_{\rm p}$). The total rotational transform is the sum of the vacuum rotational transform and that generated by the plasma current, $\iota_{\rm tot}(r) = \iota_{\rm vac}(r)+\iota_{\rm p}(r)$, with the toroidal plasma current contributing as much as 95% to the total rotational transform. Figure 2.3 shows rotational transform profiles with and without the plasma current. The rotational transform profile in the stellarator phase is fairly flat and monotonically increasing, with an edge rotational transform of $\iota_{\rm vac}(a) \sim 0.05$. With the additional rotational transform from to the plasma current, the profile is peaked at the center and monotonically decreases with $\iota_{\rm vac}(a) \sim 0.5$. This transform profile is more like that of a tokamak and is an important feature of hybrid equilibria of CTH used to study tokamak relevant MHD stability issues.

2.3 CTH Diagnostics

Diagnosis of plasma parameters such as temperature, pressure and density is essential to determine properties of a plasma equilibrium. The principles of plasma diagnostics have been reviewed in numerous references[6–8], and are generally classified on the basis of the physical quantities they are used to measure. Magnetic diagnostics are used for basic measurements such as plasma current, loop voltage, plasma position and shape, stored plasma energy and current distribution. A three-channel $1-$ mm microwave interferometer measures line-integrated plasma density in CTH.[9] A multi camera soft-Xray (SXR) diagnostic on CTH is employed to measure the equilibrium electron temperature profile and electron temperature fluctuations resulting from MHD activity.[10] An array of seven H_α detectors that measuring the Balmer line of wavelength 656.28 nm, are installed to study edge fluctuations

and measure neutral density. Spectrometers from the near-ultraviolet to visible region are present to measure emission from impurities such as carbon, oxygen, nitrogen, etc. besides the dominant hydrogen lines. A SXR spectrometer is used to measure central electron temperature. A Thomson scattering system has been designed, and is presently being installed on CTH to measure localized electron temperature and density.[11] Magnetic diagnostics in conjunction with the internal diagnostics that measure SXR emission and plasma density are used on CTH to investigate equilibrium and fluctuating quantities in the plasma. In this section we shall discuss the magnetic diagnostics used in the measurement of perturbed magnetic fields used to characterize MHD instabilities.

Magnetic diagnostics on CTH are inductive in nature and are installed external to the plasma, either on the inside or outside wall of the vacuum vessel. A Hall probe array[4,12] was fabricated for internal measurement of the poloidal magnetic field in the edge of low temperature CTH stellarator plasmas. However, it was found to perturb ohmic CTH discharges and it has not been used in the work presented in this thesis. The inductive response of a magnetic coil is given by the Faraday's law,

$$V = -\frac{d\Phi}{dt} = -NA\frac{dB}{dt} \tag{2.2}$$

where N is the number of turns of the coil, A is the cross-section area of the coil, B is the component of magnetic field along the area-normal, and V is the voltage measured at the ends of the solenoid. The signals from the diagnostics which are used for equilibrium reconstructions are electronically integrated, whereas the signals from probes that are used to study fluctuating components of magnetic field associated with the MHD instabilities are not integrated to retain the high frequency oscillations within the signal, and are given simply by equation 2.2.

A majority of the magnetic diagnostics on CTH are employed for measurement of the plasma equilibrium. These diagnostics include full and partial Rogowski coils, saddle coils,

and poloidal and radial pick-up coils, shown in figure 2.4. These diagnostics measure magnetic fields generated by both the external coils and those generated by the driven plasma current. A Rogowski is a solenoidal coil that closes on itself, measuring the magnetic field

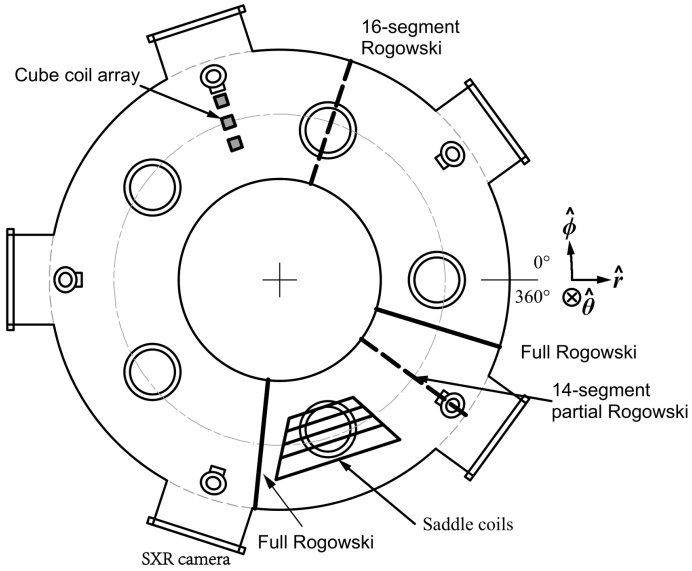

Figure 2.4: Magnetic diagnostics used in equilibrium reconstructions of CTH plasmas include full Rogowskis that measure plasma current, multi-part Rogowskis that cover complete or partial poloidal cross-sections, saddle coils to measure the radial field and an array of cube coils that measures the poloidal and radial magnetic field.

due to the current through the plane defined by the coil. Assuming that the magnetic field variation along the length of the solenoid is negligible, the total flux through the coil is given by $\Phi = NA\mu_0 I$, where N, A, and I are respectively the number of turns per unit length of the Rogowski, the cross-sectional area of the solenoid, and the current through the plane defined by the coil. The Rogowski coils are installed around the current feeds of all the magnet coils, and a section of the helical coil frame. A uniformly wound full Rogowski coil installed on the inner wall of the vacuum vessel at $\Phi = 264°$ is used to measure the toroidal plasma current. A coil exterior to the toroidal vacuum vessel is use to measure the vacuum vessel current induced by the ohmic transformer. A uniformly wound full Rogowski is insensitive to the shape or position of the plasma. In contrast, multi-part Rogowskis or partial Rogowskis are composed of multiple pick-up coils which provide local measurements

of the spatial variations of the current. These being sensitive to position and shape of the plasma are used in equilibrium reconstructions.

Poloidal flux loops are installed outside the vacuum vessel to measure poloidal flux near the plasma boundary. They consist of a conducting loop in a horizontal plane and are used to measure loop voltage created by the ohmic system. Saddle coils are installed at $\Phi = 288°$ shown in the figure 2.4 to measure the local radial field, the field normal to the vacuum vessel wall in this case. Saddle coils are rectangular loops whose area normals are in the radial direction.

Poloidal and radial pick-up coils referred to as Cube coils on CTH located at $\Phi = 108°$ in the figure 2.4, are used for local measurements of B_θ and B_r. Cube coils are turns of wire wound on rectangular pieces of Teflon®. In addition to their use in equilibrium reconstruction, they are used to determine the vertical position of the plasma.[13]

2.3.1 Magnetic diagnostics for fluctuation measurements

Strong MHD activity is observed in CTH plasmas when the value of the edge rotational transform, $\iota_{\mathrm{vac}}(a)$, is near low order rational values like 1/4, 1/3, etc. This can occur during the initial plasma current ramp phase of ohmic discharges. MHD modes can also be responsible for sudden loss of plasma confinement with strong fluctuations being observed on multiple diagnostics prior to plasma termination. These loss of confinement events are termed disruptions. MHD modes can be observed as perturbations to the equilibrium magnetic field by the magnetic pick-up coil diagnostics installed on the inner or outer wall of vacuum vessel. The structure of the MHD fluctuations in CTH is discussed in detail later in this dissertation, while the magnetic sensors built as part of this thesis work will be described in detail in this section.

On CTH, poloidal and toroidal arrays of magnetic pick-up coils are installed inside the vacuum vessel to study the structure of the MHD activity. There are three poloidal arrays installed at $\Phi = 23°,\ 223°,$ and $240°$ consisting of 16, 16, and 36 probes respectively. The

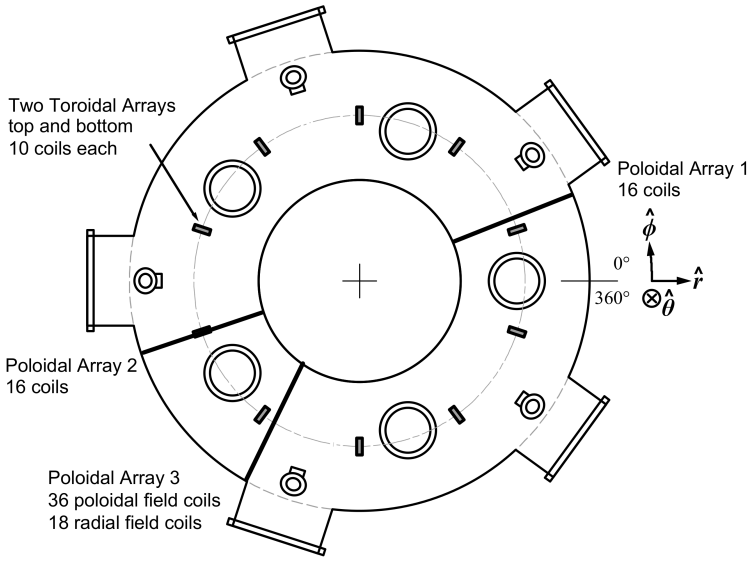

Figure 2.5: Three poloidal and two toroidal arrays of pick-up coils are installed on the inner CTH vacuum vessel wall to study magnetic fluctuations. The two toroidal arrays are nominally placed at top and bottom inside the vacuum vessel with a separation of about 36° between adjacent B-dot probes.

two toroidal arrays, with coils spaced 36° apart, are located approximately at ±90° with respect to mid-plane of CTH vacuum vessel. Nominally they are placed at $\Phi = 18° + n36°$, where $n = 0, \ldots, 9$. The precise location of these probes is given in appendix B.

The poloidal array at $\Phi = 240°$ was constructed as a part of this thesis work to measure the detailed poloidal structure of MHD modes with higher spatial resolution than the previously installed poloidal arrays. These probes are wound on custom Teflon® forms, shown in the photograph in figure 2.6(a). The design of the forms is given in appendix B.1. Over 50 coil forms were built, with 36 of them were installed in the poloidal array and rest were built to augment the toroidal array. Eighteen of the 36 probes have dual windings to measure both the poloidal and radial components of the magnetic field, B_θ and B_r.

The coil forms are designed to increase the effective NA relative to the previous probes while maintaining ease of winding and convenience in measurement of the coil position after they were installed in the machine. The product NA measures the response of the coil with changing magnetic field (see eqn. 2.2). However care must be taken to keep the probes small

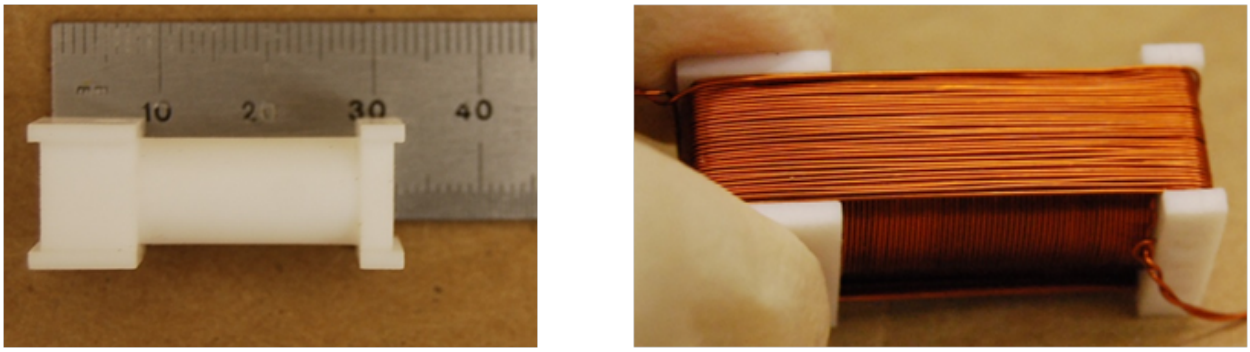

(a) (b)

Figure 2.6: (a) The installed pick-up coils are wound on custom designed Teflon® forms about 2 cm in length and 1 cm in diameter. (b) Insulator coated copper wire is wound on the form, in two perpendicular directions to measure two components of the fluctuating magnetic field. The circular cross-section is aligned along so as to measure $\dot{B}_\theta$ whereas the rectangular coil wound over it measures $\dot{B}_\mathrm{r}$.

enough that the measurement is considered local, and that the measured magnetic field does not change substantially over the volume the coil. The measured effective NA for all the probes built for this thesis are listed in appendix B. The ends of the coil form have tapped holes used to hold them in place while being wound, and to measure the their position once installed on the machine.

The coils are wound with 30 AWG magnet wire coated with a polymide resin insulation. The winding leads are then twisted to minimize stray pickup. The magnet wire is sourced from MWS wire industries with specification NEMA MW1000-1997 with quadruple insulation coating to prevent exposure of bare copper, which could lead to shorting of the coil.

A magnetic field generated by a Helmholtz coil was used to calibrate the probes. Shown in figure 2.7 is a linear relationship between the magnetic field, B, generated by the current, I_0, through the Helhmholtz coil. The magnetic field is measured using a Hall probe as a calibration standard. The slope of the line, α, is used later to relate the current in the coil to the magnetic field.

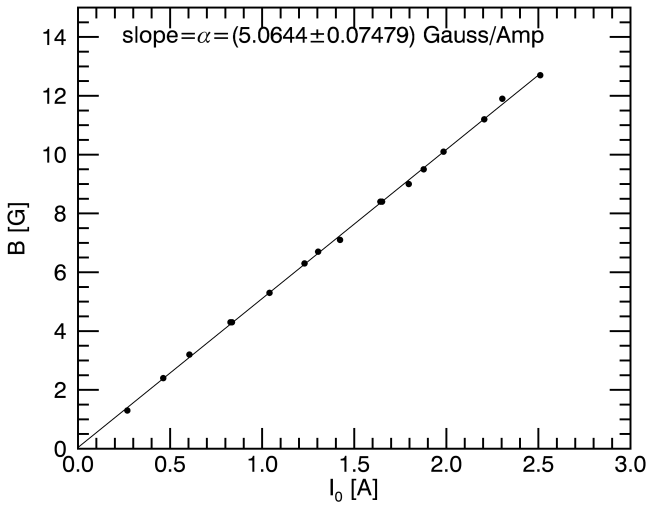

Figure 2.7: The magnetic field at the center of the Helmholtz coil is measured with a hall probe as a function of current in the coils. The dots represent the measurements of the B-field for different current values whereas the solid line is the linear fit to the data.

The calibration of the effective response, NA, of these B-dot probes is accomplished by suspending them in a time varying magnetic field generated by the Helhmoltz coil. The B-dot probe is suspended in such a fashion that the axis of the Helhmholtz coil coincides with the axis of the B-dot probes. The magnetic field is measured to be uniform at the location inside the bore of the Helmholtz coil where these B-dot probes are suspended, while the Hall probe measurements are accurate to within 0.2 G. The current source to the Helmholtz coil is connected to the sinusoidal voltage output of a function generator and the voltage response of the B-dot probe is measured across the leads of the probe. The current through in the Helmholtz coil was found by measuring the voltage drop, $V_{\rm r}$, measured across an $R = 5\Omega$, high precision, $\sim 0.1\%$ resistor, in series with the Helhmholtz coil. The response of the B-dot probe, $V_{\rm c}$, to the sinusoidally varying magnetic field, $B = B_0 \sin(2\pi f t + \delta)$ is given by equation 2.3.

$$\begin{aligned} V_{\rm out} &= -NA\frac{dB}{dt} \\ &= -2\pi f NAB_0 \cos(2\pi f t + \delta) \end{aligned} \tag{2.3}$$

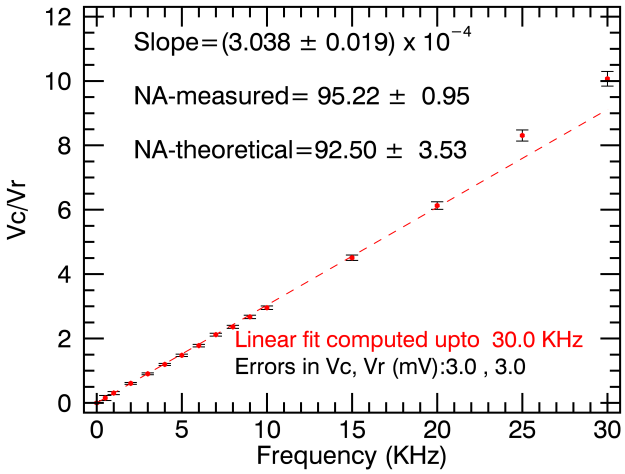

Figure 2.8: The ratio of the voltage measured at the ends of the B-dot probe, V_c, and the resistance r, V_r, is plotted against the frequency of the changing current or magnetic field. NA can be computed from the slope of the line.

For simplicity we pick an instant to measure the voltage at the B-dot probe and using the relation, $B_0 = \alpha I_0$, gives us the relation in Eq.2.4, from which NA is determined.

$$\begin{aligned} (V_{\text{out}})_{\text{peak}} &= 2\pi f NAB_0 \\ &= (2\pi f \alpha I_0)\, NA \end{aligned} \tag{2.4}$$

The current in the calibration circuit, I_0, is known from the measurement of voltage, V_r, across the resistance, R. Solving for NA, equation 2.4 can be written as,

$$\begin{aligned} NA &= \frac{R}{2\pi\alpha} \times \frac{\frac{V_{\text{out}}}{V_r}}{f} \\ &= \frac{R}{2\pi\alpha} \times \text{slope} \end{aligned} \tag{2.5}$$

where the slope is measured using a linear fit to the calibration data. Calibration data for one B-dot probe and result of the fit are shown in figure 2.8. The calibration data was collected for frequencies ranging from 500 Hz to 30 kHz. We could also compute the NA of these probes from the knowledge of the geometry of the forms and the dimensions of the wire used to wind them. The advantage of having used a designed form is that the NA values

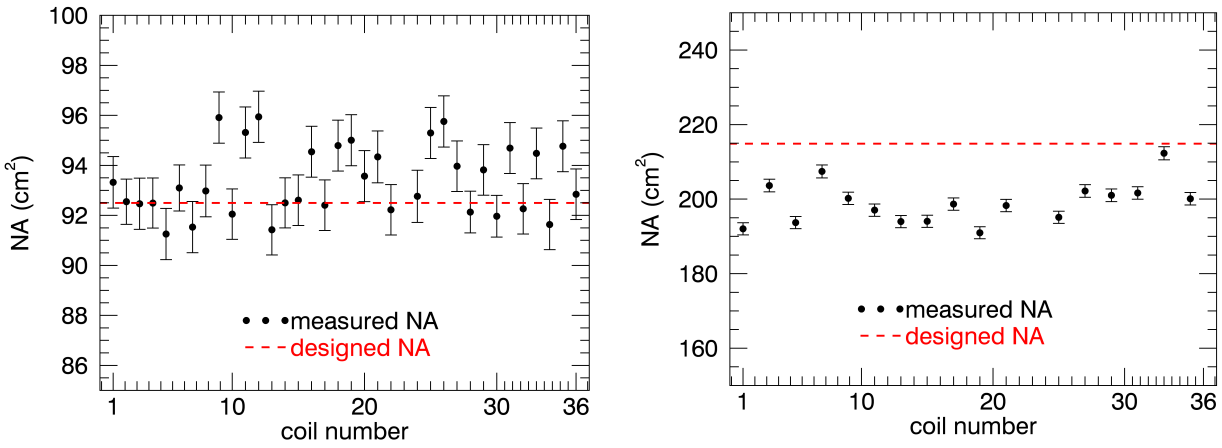

(a) $\dot{B}_\theta$-coils (b) $\dot{B}_\mathrm{r}$-coils

Figure 2.9: Comparison of effective response, NA, for all B-dot probes with their design value is shown. The dashed red line indicates the NA computed from the knowledge of number of turns and the area of these probes. (a) Calibrated effective response is shown for 36 probes, all of which are designed to measure poloidal field, B_θ, range from $NA = 91\,\mathrm{cm}^2$ to $NA = 96\,\mathrm{cm}^2$, close to their designed value of $NA = 92.5\,\mathrm{cm}^2$. The probes are numbered from 1 to 36 with every odd numbered probe also designed to measure radial field, B_r.(b) Calibrated effective response for 18 probes which are designed to measure radial field, B_r, is shown in the right figure. Their design value is $NA = 215\,\mathrm{cm}^2$ whereas the measured values are somewhat lower with a larger variation across the probes.

of these B-dot probes are comparable to each other and very close to their predicted values. This is evident from the comparison of NA for all the probes shown in figure 2.9. These new B-dot probes are more sensitive to the changing magnetic fields with an effective NA of about 92 cm^2 compared to roughly 50 cm^2 for the previously installed B-dot probes. For the B-dot probes that also measure the radial magnetic field B_r, the NA is about 215 cm^2. The response of the radial field coils is designed to be larger to compensate for smaller values of the B_r, typically by a factor of three, compared to values that of B_θ. The data from the these radial probes has not been used in the analysis presented in this dissertation. The deviation from the theoretical value for all the probes that measure $\dot{B}_\theta$ is in the range of 1.6-3.7%, while for the probes that measure $\dot{B}_\theta$, the deviation is in the range of 0.5-11.5%.

The B-dot probes were then assembled on a circular, nonmagnetic SS 316 frame 10.5″ in diameter. The circular frame can be broken into two halves so that it fits through the 16″ diameter tubes that makeup the side ports of CTH. The probes are attached to the

frame using L-shaped mounting brackets as shown in figure 2.10. As can be seen from the figure 2.10a, alternate B-dot probe measures both radial and poloidal field whereas the poloidal field is measured by all the probes. To protect the B-dot probes from coming into contact with the plasma, six stainless steel limiters 0.75″ wide are placed along the circular frame. The twisted leads of each B-dot probe are encased in a braid made out of PEEK, a thermoplastic material, that runs along the outer circumference of the circular frame. The PEEK is compatible with the base pressure of CTH which is of the order of $60 - 80$ nTorr.

Once the whole array was assembled on the bench, the position of each coil with respect to the frame was measured using a coordinate measuring machine (CMM). The B-dot probes were placed in such a fashion that the axis of each B-dot probe was tangent to the circumference of the frame so that once installed inside the vacuum vessel they would measure mostly the poloidal component of the magnetic field assuming the plasma is circular. In practice, CTH plasmas are neither centered horizontally within the vacuum vessel nor circular; however the coil array is centered horizontally and vertically inside the vacuum vessel. The array is then placed inside the vacuum vessel and the frame position is measured in place. Finally, the probes are covered with stainless steel stock about 0.003″ thick to shield out electrostatic noise.

The leads of each B-dot probe are connected to sub-D feed-throughs sourced from Accu-Glass products, Inc. On the outside of the vacuum vessel, these leads are connected to instrumentation amplifiers designed for low impedance loads such as the B-dot probes. Data acquisition for these B-dot probes is performed at the rate of 500 kS/s. The amplifier circuitry for these probes include, a two-pole Sallen-Key low-pass Butterworth filter, for low gain at signal frequencies greater than 250 kHz to prevent aliasing. The response of the amplifiers is designed to be flat up to 50 kHz. The measured circuitry frequency response is shown in figure 2.11. The gain of the circuit is approximately 7 and the 3 db frequency of the filter circuit is near 80 kHz. The rotating MHD activity analyzed with these B-dot probes

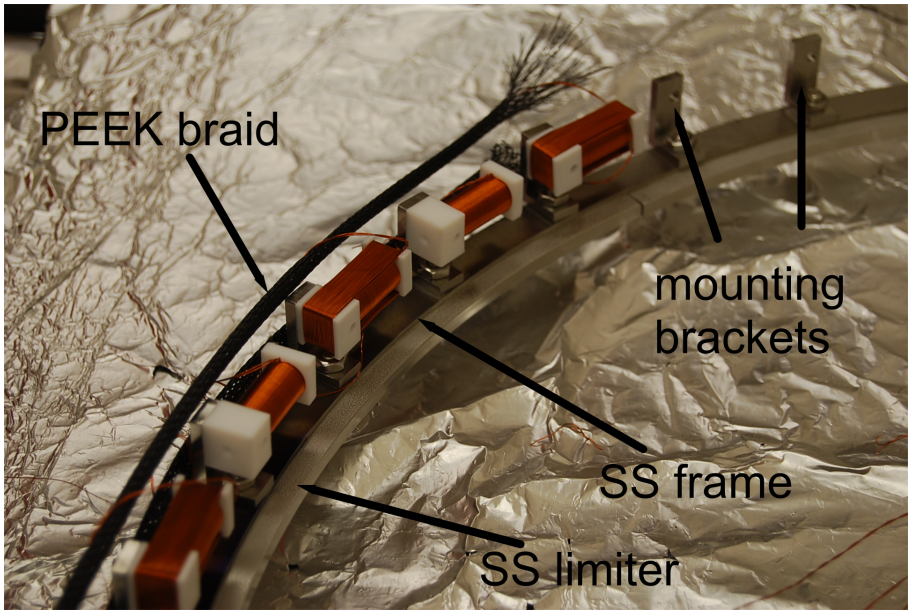

(a)

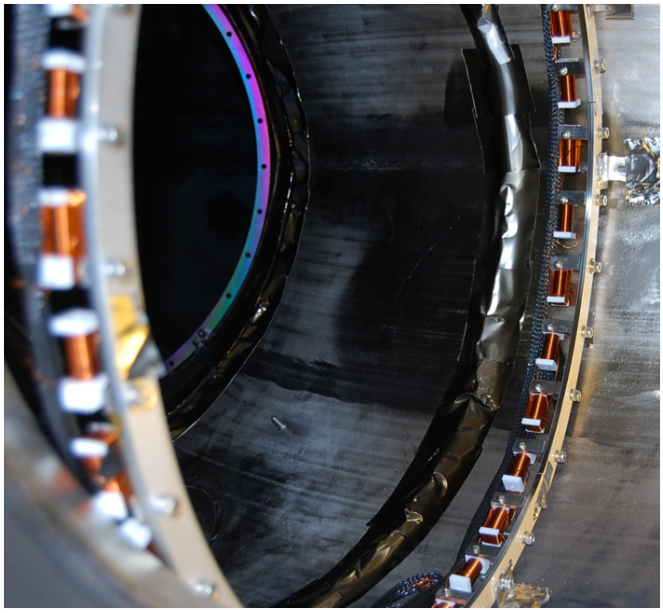

(b)

Figure 2.10: (a) Photo of the partially assembled poloidal array on the bench. B-dot probes are mounted onto a SS 316 frame $10^{1}/_{2}''$ in diameter with L-shaped brackets also made out of SS 316 material. SS limiter $^{3}/_{4}''$ thick, prevents plasma from coming into contact with the frame. B-dot probes designed to measure both poloidal and radial field, and those designed to measure only the poloidal field are alternately positioned. The leads of the each probe is protected by a PEEK braid that runs along the circumference of the whole assembly. (b) The completed assembly is mounted inside vacuum vessel in a plane nominally located at toroidal angle, $\Phi = 242°$.

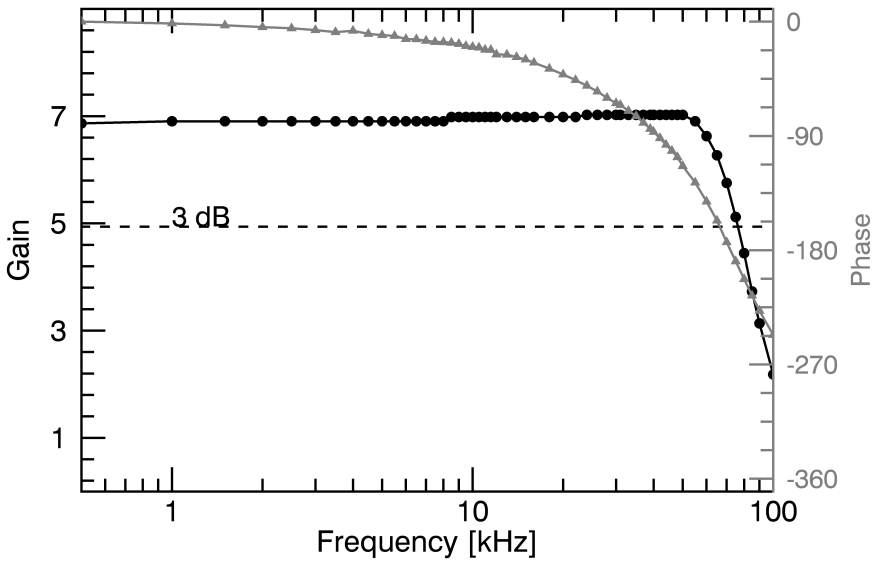

Figure 2.11: Frequency and phase response for the circuitry used in amplification of the B-dot probe signals is shown. A gain of seven is designed to be flat up to a frequency of 50 kHz with the 3 db frequency occurring at 80 kHz. The data from these B-dot probes is recorded at the rate of 500 kHz, thus the gain of these amplifiers is designed to drop to a small value at the Nyquist frequency of 250 kHz to prevent aliasing effects. In addition to the drop in gain, a phase shift is introduced by the filtering circuit of the amplifier, as a function of frequency. The frequency of the MHD modes observed in CTH is in the range $1 - 20$ kHz; thus in order to determine whether a correlation between multiple modes exists, the phase shift must be corrected.

is typically in the approximate range of $5 - 20$ kHz. The phase-shift introduced by the amplifiers must be numerically corrected at the time of data analysis.

2.4 Equilibrium Reconstruction of CTH Plasmas

Reconstructions of the CTH equilibria presented in this dissertation are performed using the V3FIT code[14], which presently uses the VMEC[15] as its equilibrium solver. VMEC solves for a three-dimensional MHD equilibrium assuming the existence of closed, nested flux surfaces and VMEC takes as inputs the vacuum magnetic fields, plasma current profile and pressure profile. The goal of the reconstruction process is to obtain the most probable plasma current and pressure profiles consistent with the measurements. The measurements can be from external magnetic diagnostics such as full and segmented Rogowski coils, saddle

coils, and internal diagnostics such as an interferometer, and SXR emission diagnostics. Information from external magnetic diagnostics are used in this dissertation to compute the equilibrium reconstructions.

The current and pressure profiles which represent the VMEC equilibrium are defined by a set of input parameters such as for example total enclosed toroidal flux, and the parameters that define current and pressure profiles. V3FIT optimizes the input parameters, by minimizing the mismatch between the measured signals and the corresponding modeled signals. For each measured signal, model signals are computed from the VMEC equilibrium obtained with external currents.

This optimization of the input parameters involves minimzing the mismatch, χ^2, defined by,

$$\chi^2(\mathbf{p}) \equiv \sum_i^N \frac{\left[S_i^O(\mathbf{d},\mathbf{p}) - S_i^M(\mathbf{p})\right]^2}{(\sigma_i)^2} \tag{2.6}$$

where N is the number of diagnostics used. The observed signal for the i^{th} diagnostic is given by S_i^{O} and the corresponding model-computed signal is given by S_i^{M}. The observed signals are dependent on the measured data, $\mathbf{d}$, and the optimized input parameters, $\mathbf{p}$. The modeled signal is only a function of the input parameters to be optimized. An uncertainty of the measurement is represented by σ_i, is the measured variance of signals.[16] For measurements within the uncertainty of the measurement the value of χ^2 is expected to be approximately equal to the number of diagnostics, N. Further details of equilibrium reconstruction on CTH can be found in the thesis by Stevenson[4] and a recent publication by Ma, et. al.[16]

The five-fold symmetry of the CTH magnetic configuration, and the effect of toroidal plasma current is demonstrated in the figure 2.12, which shows contour plots of the outermost flux surface of plasma with and without the ohmically driven current.[16] The left hand side of the contour figure is obtained by equilibrium reconstruction with no plasma current and the closed flux surfaces are shown at four different toroidal locations. The right side shows flux surfaces with a plasma current of $I_{\text{p}} = 53.6\,\text{kA}$. The poloidal cross-section becomes less elliptical with the addition of plasma current, but the $n = 5$ stellarator periodicity is

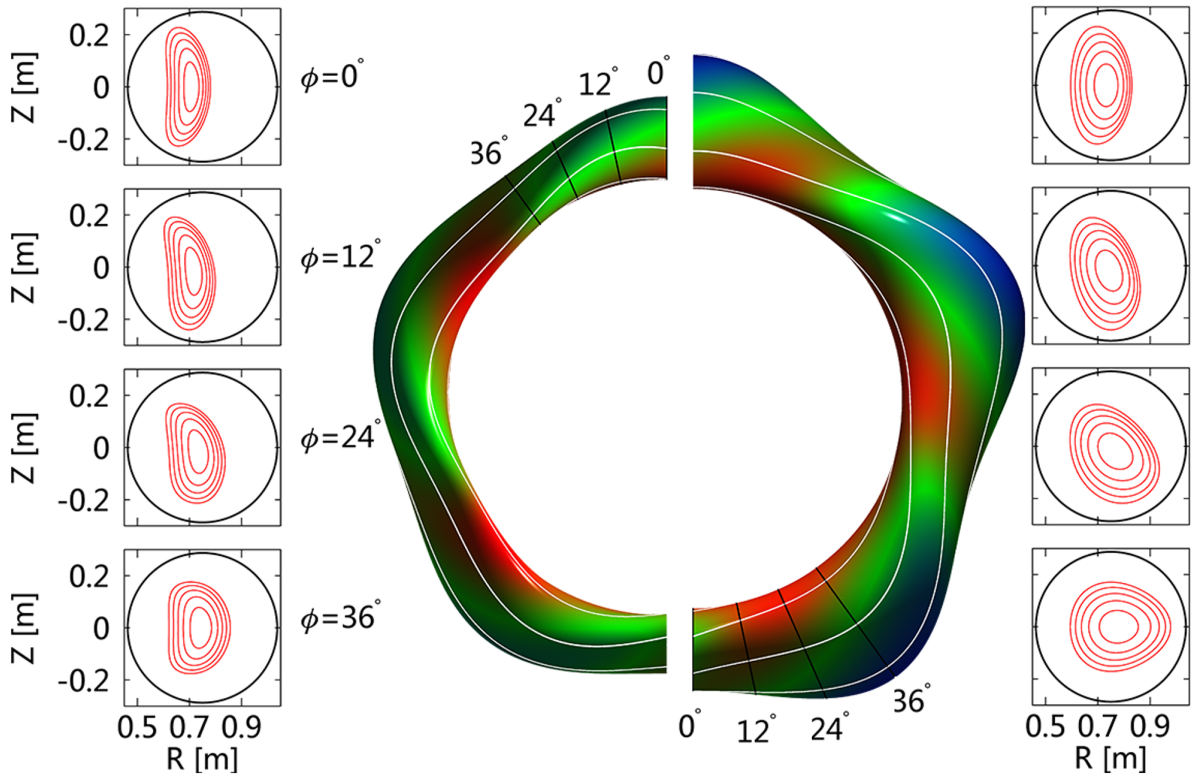

Figure 2.12: Poloidal cross-sections of flux surfaces and contour plots of the last closed flux surfaces of CTH with (left) and without (right) toroidal plasma current are shown. The colors represent the magnitude of the magnetic field, blue being low and red, high. The white lines represent the magnetic field lines which have larger twist when plasma current is driven on the stellarator equilibrium.

enhanced. The figure also shows that individual magnetic field lines in white, are twisted more with the addition of the poloidal field due to the toroidal plasma current, indicating that the rotational transform of the flux surface has increased.

References

[1] J. Freidberg. *Ideal MHD*. Cambridge University Press, 2014.

[2] J. Peterson, J. Hanson, G. Hartwell, and S. Knowlton. Vacuum magnetic field mapping experiments for validated determination of the helical field coil location in stellarators. *Physics of Plasmas*, 17(3), 2010.

[3] J. T. Peterson. *Vacuum Magnetic Flux Surface Measurements Made On the Compact Toroidal Hybrid*. PhD thesis, Auburn University, 2008.

[4] B. A. Stevenson. *3D Reconstruction of Plasma Equilibria using Magnetic Diagnostics on the Compact Toroidal Hybrid*. PhD thesis, Auburn University, 2011.

[5] W. D. D'haeseleer, W. N. G. Hitchon, J. D. Callen, and J. L. Shohet. *Flux Coordinates and Magnetic Field Structure: A guide to a Fundamental Tool of Plasma Theory*. Springer-Verlag, 1991.

[6] I. H. Hutchinson. *Principles of Plasma Diagnostics*. Cambridge University Press, 2002.

[7] Equipe TFR. Tokamak plasma diagnostics. *Nuclear Fusion*, 18(5):647, 1978.

[8] E. J. Strait. Magnetic diagnostic system of the DIII-D tokamak. *Review of Scientific Instruments*, 77(2), 2006.

[9] M. C. Miller, J. D. Hanson, G. J. Hartwell, S. F. Knowlton, D. A. Maurer, and B. A. Stevenson. Design and implementation of a multichannel millimeter wave interferometer for the compact toroidal hybrid experiment. *Review of Scientific Instruments*, 83(10), 2012.

[10] J. L. Herfindal, J. D. Dawson, D. A. Ennis, G. J. Hartwell, S. D. Loch, and D. A. Maurer. Design and initial operation of a two-color soft x-ray camera system on the compact toroidal hybrid experiment. *Review of Scientific Instruments*, 85(11), 2014.

[11] P. J. Traverso, D. A. Maurer, D. A. Ennis, G. J. Hartwell, M. M. Goforth, S. D. Loch, A. J. Pearce, and M. R. Cianciosa. Thomson scattering diagnostic system design for the compact toroidal hybrid experiment. *Review of Scientific Instruments*, 85(11), 2014.

[12] B. A. Stevenson, S. F. Knowlton, G. J. Hartwell, J. D. Hanson, and D. A. Maurer. Hall probe measurements of the poloidal magnetic field in Compact Toroidal Hybrid plasmas. *Review of Scientific Instruments*, 85(9), 2014.

[13] M. C. ArchMiller, M. R. Cianciosa, D. A. Ennis, J. D. Hanson, G. J. Hartwell, J. D. Hebert, J. L. Herfindal, S. F. Knowlton, X. Ma, D. A. Maurer, M. D. Pandya, and P. Traverso. Suppression of vertical instability in elongated current-carrying plasmas by applying stellarator rotational transform. *Physics of Plasmas*, 21(5), 2014.

[14] J D Hanson, S. P. Hirshman, S F Knowlton, L.L. Lao, E.A. Lazarus, and J. M. Shields. V3FIT: a code for three-dimensional equilibrium reconstruction. *Nuclear Fusion*, 49(7):075031, 2009.

[15] S. P. Hirshman and J. C. Whitson. Steepest descent moment method for three dimensional magnetohydrodynamic equilibria. *Physics of Fluids*, 26(12):3553–3568, 1983.

[16] X. Ma, D. A. Maurer, S. F. Knowlton, M. C. ArchMiller, M. R. Cianciosa, D. A. Ennis, J. D. Hanson, G. J. Hartwell, J. D. Hebert, J. L. Herfindal, M. D. Pandya, N. A. Roberds, and P. J. Traverso. Non-axisymmetric equilibrium reconstruction of a current-carrying stellarator using external magnetic and soft x-ray inversion radius measurements. *Physics of Plasmas*, 22(12), 2015.

Chapter 3

Magnetohydrodynamic activity in current-carrying CTH plasmas

3.1 Introduction

CTH plasmas with driven current harbor an interesting range of magnetohydrodynamic (MHD) modes.[1–4] In this chapter we shall identify several rotating MHD modes observed during CTH discharges. In cylindrical geometries an MHD mode can be identified by the Fourier harmonics of its poloidal and toroidal structure, m and n respectively.[5] The interpretation of the spatial structure of these modes is not as straightforward in toroidal plasmas, which in CTH is further complicated by the nonaxisymmetric or three dimensional nature of its equilibrium. The structure of the MHD modes and toroidal effects are discussed in detail in chapter 4. We shall refer to MHD modes by Fourier mode numbers (m/n) even though these modes may not be sinusoidal in nature.

The method to obtain fluctuations in the poloidal field, δB_θ, from the raw pickup coil signals is outlined in section 3.2. In the section 3.3 the biorthogonal decomposition technique is developed to interpret the structure of rotating MHD modes using the measurements from the poloidal and toroidal B-dot probe arrays inside CTH. Finally, in section 3.4, MHD modes observed during a typical current-carrying CTH discharge are identified.

3.2 Identification of MHD mode numbers in current-carrying CTH plasmas

CTH is equipped with poloidal and toroidal arrays of magnetic pick-up coils, or B-dot probes, to measure the fluctuations in the poloidal component of the magnetic field, δB_θ, as is described in Chapter 2. In the analysis presented in the rest of this thesis, we will use one poloidal array consisting of thirty-six B-dot probes, located at toroidal angle, $\phi = -117°$,

and one toroidal array of ten B-dot probes positioned at $\theta = +90°$, at the top of the vacuum vessel. Figure 3.1 shows the positions of the probes in these arrays. The angle $\theta = 0°$ at the outboard mid-plane, and the angle $\phi = 0°$ as indicated in the figure 3.1. These probes

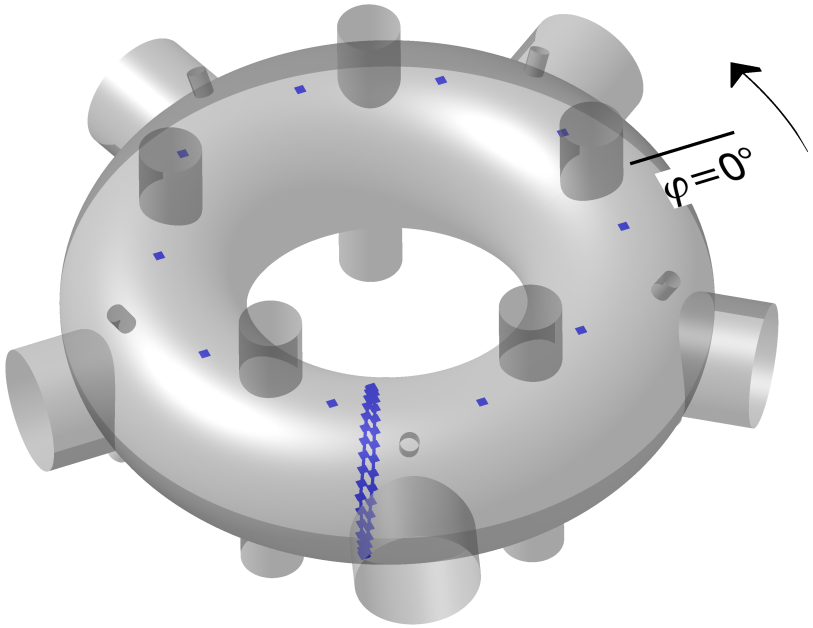

Figure 3.1: MHD activity observed in current-carrying CTH plasmas is measured with B-dot probes (shown in blue) belonging to a poloidal array with 36 probes placed every 10° and a toroidal array of 10 probes placed every 36°. Shown in gray is the CTH vacuum vessel with its vertical, horizontal and angled ports.

provide local measurements of the poloidal magnetic field from both equilibrium and MHD perturbations. A method to extract the poloidal field fluctuations from the raw pickup coil signals is outlined by the plots in figure 3.2. The measured raw signal, dB_θ/dt, for one of the probes is shown in the top panel, which after numerical integration gives the local poloidal field, $B_\theta(t) = \int \frac{dB_\theta}{dt} dt$, at the location of this probe, shown in the second panel. The fluctuations in the poloidal field, δB_θ, are obtained by subtracting a boxcar averaged signal from the total signal, $\delta B_\theta = B_\theta(t) - \langle B_\theta(t) \rangle$. The fluctuations for the window highlighted in figure 3.2, shown in the bottom panel, are coherent, with peak-to-peak amplitude of about 4 G. The spatial structure of these fluctuations can be deduced from measurements of δB_θ from the poloidal and toroidal arrays of the B-dot probes. Figure 3.3a shows the

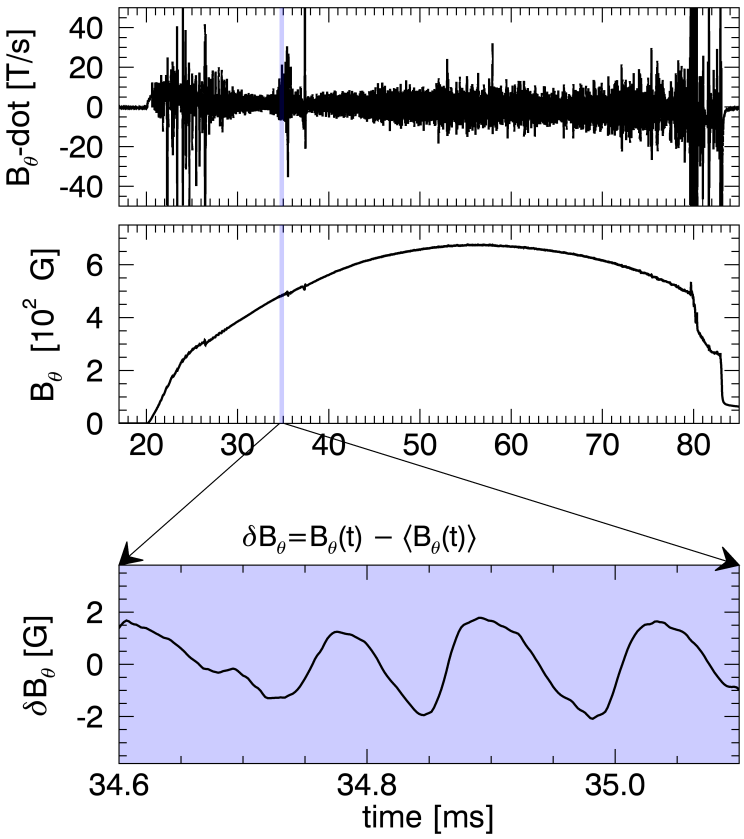

Figure 3.2: The raw signal, $\dot{B}_\theta$, measured by one of probes for shot 14021473 is shown the top panel. The middle panel shows the poloidal field, B_θ, obtained after numerical integration of the raw signal. Fluctuations in poloidal field, δB_θ, for the highlighted region are shown in the bottom panel.

δB_θ measurements for all the probes in the poloidal array. The plotted signals are offset by the poloidal angle at which they are located, with the probes at inboard midplane located at the top and bottom of the stack, at $\theta = \pm 180°$, and probe at the outboard midplane at the center, or $\theta = 0°$. The poloidal mode number of $m = 2$ can be deduced by counting the number of peaks in the signal going from bottom to top. A vertical dashed line is shown to help guide the eye. A contour plot of the intensity of the same signals is shown in figure 3.3b. At a fixed time there are two nodes, again giving an $m = 2$ mode. The toroidal mode number of $n = 1$ is deduced in a similar manner from the measurements made with the toroidal array of B-dot probes.

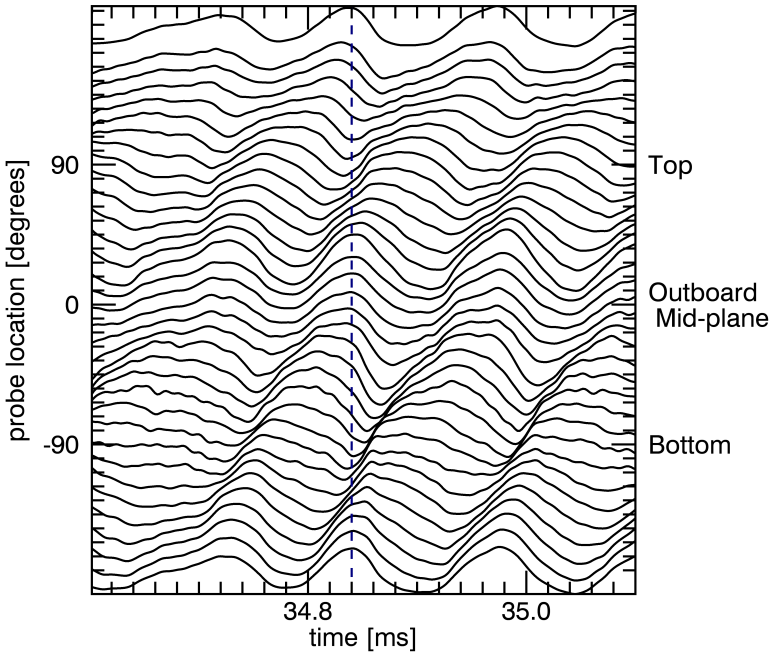

(a)

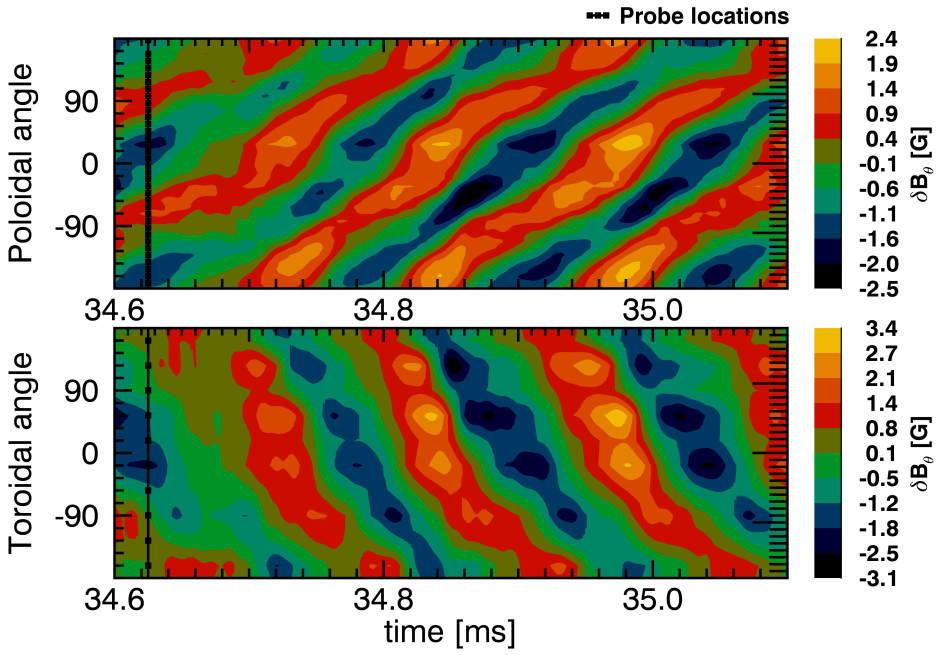

(b)

Figure 3.3: (a) Signals for the poloidal array of probes for shot 14021473 are shown offset by angular position of each probe with the probe located at the inboard midplane is shown at the bottom of the plot and outboard midlplane is the middle. The poloidal structure of MHD activity is determined to be $m = 2$ by counting the number of nodes at a fixed time indicated by a vertical dashed line. (b) The contour plots of these signals from polodial and toroidal array of B-dot probes show that the MHD activity corresponds to an $m = 2/n = 1$ mode. The black squares represent the location of the B-dot probes that measure the shown signals. The probes are placed every 10° in the poloidal array and every 36° in the toroidal array.

Such visual inspection of mode activity however, does not determine the actual MHD mode structure, which in circular, cylindrical plasmas is obtained by the Fourier analysis of fluctuations measured by spatially distributed arrays of B-dot probes. In non-circular, toroidal plasmas, the poloidal mode structure an MHD mode is no longer represented by a single Fourier harmonic of poloidal structure, m. A Fourier analysis of δB_θ performed for the poloidal array of B-dot probes is shown in figure 3.4. This indicates that along with an $m = 2$ mode, an $m = 1$, and other Fourier harmonics are associated with the MHD activity. A discussion of the fact that in toroidal plasmas multiple poloidal harmonics are associated

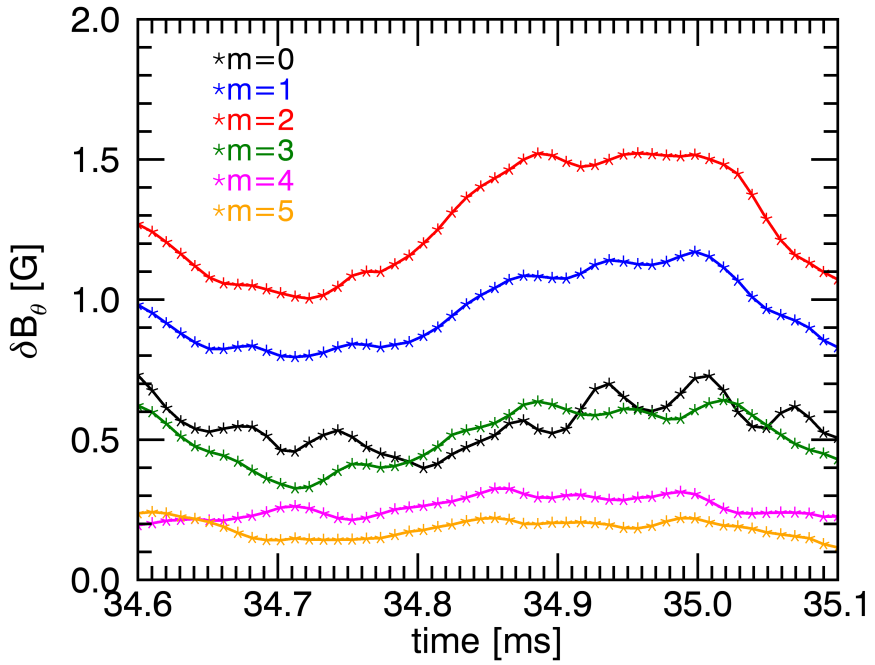

Figure 3.4: A Fourier analysis of fluctuations, δB_θ, measured by poloidal array of B-dot probes indicates presence of multiple Fourier harmonics.

with a single MHD mode is presented in greater detail in Chapter 4. However, at present we shall refer to MHD modes by the number of nodes deduced from visual inspection of the fluctuations, δB_θ, at a fixed time.

A visual inspection of the fluctuations fails if the observed magnetic activity is comprised of MHD modes having different poloidal, m, and toroidal, n, mode numbers. A more systematic method to determine the spatial and temporal structures uses a bi-orthogonal

decomposition technique (BD) which will be presented next, where BD will be applied to the $m = 2/n = 1$ mode we have shown earlier in this section.

3.3 Identification of dominant MHD modes using biorthogonal decomposition technique

The biorthogonal decomposition (BD) technique is used in plasma physics to investigate the spatial and temporal structure of magnetic perturbations.[6–11] BD is also known in the literature as singular value decomposition (SVD)[7,12]. BD decomposes a set of signals evolving in space and time into orthogonal spatial and temporal modes[13], with each spatio-temporal pair weighted by a singular value. This method has been demonstrated to be a robust tool to analyze fluctuations measured by multichannel diagnostics like poloidally and toroidally separated magnetic probes and multi-chord SXR cameras.[6–8,10,14] An important feature of this method is that it does not require any assumptions about the spatial structure of the MHD mode. If the signals are sinusoidal in both space and time then the result of BD and Fourier analysis will be identical. Some properties of the BD method are summarized as follows[6]:

1. Rotating modes in the data are represented by degenerate singular values, each with its own spatio-temporal structure;

2. Two or more spatial modes with different structures but rotating with same frequency are identified as single mode by BD with distorted spatial structure; however, the BD can't distinguish between different MHD modes of same frequency;

3. The singular values not related to a coherent spatial or temporal behavior are small in amplitude, and lie in the noise of the signal.

The BD breaks a rectangular, $m \times n$ matrix, A, into two rectangular matrices, U and V, and a diagonal, $n \times n$ matrix, Σ,

$$A = U\Sigma V^{\dagger}. \tag{3.1}$$

We shall apply this decomposition to determine the poloidal and toroidal mode structures embedded in the magnetic fluctuations measured by the arrays of B-dot probes shown in figure 3.1. The columns of the signal matrix contain time history of individual channels, while each row is the measured signal by all channels at one instance of time. Consider a signal matrix composed of n channels with m sample points in time, then U can be thought of as a set of n column vectors, u_i, each of length m, while $V^{\dagger}$ is a set of n row vectors, v_i, again of length m. This can be illustrated in the following way:

$$\underbrace{\begin{bmatrix} \uparrow & \uparrow & & \uparrow \\ s_1 & s_2 & \cdots & s_n \\ \downarrow & \downarrow & & \downarrow \end{bmatrix}}_{Signal\ Matrix} = \underbrace{\begin{bmatrix} \uparrow & \uparrow & & \uparrow \\ u_1 & u_2 & \cdots & u_n \\ \downarrow & \downarrow & & \downarrow \end{bmatrix}}_{Temporal\ Modes} \underbrace{\begin{bmatrix} \sigma_1 & & & \\ & \sigma_2 & & \\ & & \ddots & \\ & & & \sigma_n \end{bmatrix}}_{Singular\ Values/Weights} \underbrace{\begin{bmatrix} \leftarrow & v_1 & \rightarrow \\ \leftarrow & v_2 & \rightarrow \\ & \vdots & \\ \leftarrow & v_n & \rightarrow \end{bmatrix}}_{Spatial\ Modes} \tag{3.2}$$

The result of the decomposition is a set of temporal modes, u_i, arranged in columns, with corresponding singular values or weights, σ_i, and a corresponding set of spatial modes, v_i. The matrix Σ contains the singular values arranged in a descending order. The condition of bi-orthonormality implies that spatial modes are orthonormal, $u_i \cdot u_j = \delta_{i,j}$, and so are temporal modes, $v_i \cdot v_j = \delta_{i,j}$. BD generates the same number of biorthogonal modes as the number of diagnostic signals used, with the first mode being the most coherent mode in the measurement, and the last mode in most cases is uncorrelated background noise.

Next, we apply biorthogonal decomposition to the magnetic fluctuation data shown in the contour plots of figure 3.3b. The signal matrix is comprised of 35 channels belonging to the poloidal array that determine the poloidal structure and 10 channels of the toroidal array

that determine the toroidal structure of the poloidal magnetic field fluctuations, δB_θ. The resulting set of singular values are shown in figure 3.5 for a set of 45 modes, corresponding to the 45 diagnostics, ordered by their singular value or weight. As can be seen from the distribution of singular values in this example, the first two values are almost one order of magnitude larger than the rest. It will be shown later that these two modes combine to

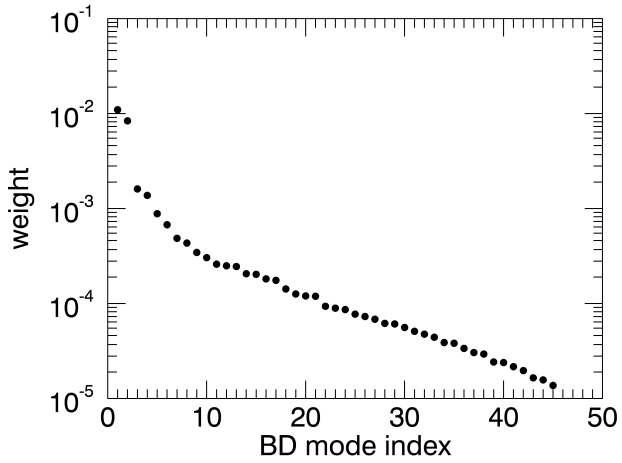

Figure 3.5: A set of 45 BD modes arranged in decreasing order are obtained when a set of spatio-tempral signals from as many diagnostics are used. The singular value distribution is dominated by a degenerate pair of BD modes. The singular value for the next pair of degenerate modes is an order lower in magnitude, while rest of the singular values appear to form a continuum.

form a quadrature pair of a rotating mode with poloidal mode number, $m = 2$ and toroidal mode number, $n = 1$. After this dominant mode, there are two more singular values close in amplitude, which later, will be shown to be another rotating mode, with mode number, $m/n = 4/2$. The rest of the singular values form a continuum and are close to the noise floor of the measurements. The weight distribution of these modes can be quantified by several parameters, one of them is the global signal energy which is the sum of squared weights, given by,[7]

$$E = \sum_{i=1}^{45} \sigma_i^2. \tag{3.3}$$

The relative amount of energy in each pair of spatio-temporal mode is useful for comparing different data sets and is given by,

$$p_i = \sigma_i^2 / E. \tag{3.4}$$

The value of relative energy is in the range, $0 \leq p_i \leq 1$ and the sum for all the spatio-temporal pair is one, $\sum_{i=1}^{45} p_i = 1$.

We mentioned earlier that the degenerate singular values obtained from biorthogonal decomposition can represent a traveling wave. This can be demonstrated with an example of a traveling wave which can be separated into spatial and temporal components using the trigonometric identity as given by,

$$cos(n\phi + \omega t) = \underbrace{cos(n\phi)}_{Spatial}\underbrace{cos(\omega t)}_{Temporal} - \underbrace{sin(n\phi)}_{Spatial}\underbrace{sin(\omega t)}_{Temporal}. \tag{3.5}$$

For the singular value distribution shown in figure 3.5 the first two modes have approximately degenerate singular values, $\sigma_1 = 0.011$ and $\sigma_2 = 0.0084$, together representing approximately 96% of the total signal energy. For a perfectly sinusoidal traveling wave in a cylinder these singular values would be equal. Whereas the next two modes, also with approximately degenerate singular values, $\sigma_3 = 0.0016$ and $\sigma_4 = 0.0013$, represent 3% of the total signal energy. The spatio-temporal modes corresponding to first four singular values are shown in figure 3.6. In figure 3.6a, a polar plot with radial excursion proportional to the strength of the fluctuations measured by each probe is used to demonstrate the structure of the mode. Each dot represents a probe in the poloidal array of probes and dashed circle represents zero perturbation. Since there are two lobes, this is referred to as an $m = 2$ mode. The black and orange colors represent the first and the second mode respectively, which are offset in phase and thus forming a quadrature pair as demonstrated earlier with the simple example of a traveling wave. For a perfectly sinusoidal traveling wave this phase difference would be 90°. That this is an $n = 1$ mode can be inferred from the structure of the fluctuations

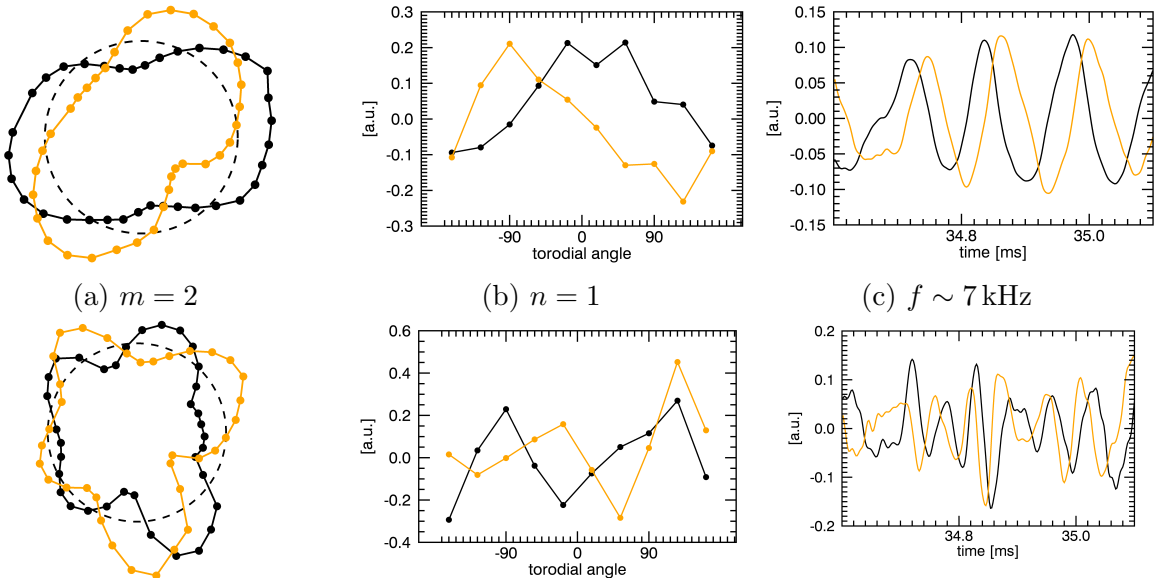

(a) $m = 2$ (b) $n = 1$ (c) $f \sim 7\,\mathrm{kHz}$

(d) $m = 4$ (e) $n = 2$ (f) $f \sim 14\,\mathrm{kHz}$

Figure 3.6: Corresponding to the first four BD modes, the spatial and temporal modes are shown. The spatial structure of the first two modes separated into poloidal and toroidal structure shown in (a) and (b), with dots representing a B-dot probe. The poloidal structure is represented by a polar plot where the radial excursion is proportional to size of the perturbation and dashed circle represents zero perturbation. An $m = 2/n = 1$ spatial structure is evident from these plots. The temporal structure for the first two modes is shown in (c). The spatial and temporal structure of both the modes is shifted in phase and forms a quadrature pair of rotating modes. Plots (d)-(f) show that the third and fourth BD modes also forms a quadrature pair, of a rotating $m = 4/n = 2$ mode.

measured by the toroidal array, shown in figure 3.6b. The temporal modes also consist of the quadrature pair, with a frequency of $f \sim 7\,\mathrm{kHz}$ as is shown in 3.6c. Thus we identify this to be an $m = 2/n = 1$ MHD mode. The poloidal and toroidal structure of the next two BD modes corresponds to 4/2 with mode rotation frequency of $f \sim 14\,\mathrm{kHz}$ as is shown in figures 3.6d to 3.6f. This 4/2 mode is a harmonic of the 2/1 mode that exists on the flux surface with edge safety factor, $q = 2$, which is consistent with observations made in other experiments.[8] Contour plots of the 2/1 and 4/2 modes are shown in figures 3.7a and 3.7b by recombining the spatio-temporal modes with appropriate singular values. Note that the modulations observed on the toroidal structure reflects the five-fold periodicity of the equilibrium field of the CTH stellarator.

In this section, we have presented an empirical method to identify multiple MHD modes coexisting in 3D (non-axisymmetric) plasmas. In applying this method to mode identification in CTH plasmas, we restrict our analysis to dominant modes with relatively large singular values because one of the drawbacks of the BD algorithm is its inability to assign confidence intervals to the components.[7]

3.4 Observation of MHD modes in typical current-carrying CTH plasmas

MHD modes are observed during the evolution of CTH discharges with inductively driven plasma current. A set of signals from a CTH discharge is shown in figure 3.8, with a discharge length of approximately 80 ms. A stellarator plasma is produced on the closed nested flux surfaces using electron cyclotron resonance heating at $t = 0$ ms. At $t = 20$ ms toroidal plasma current, I_{p} is inductively driven on this stellarator equilibrium shown in figure 3.8a. The plasma current reaches a peak value of $I_{\mathrm{p}} = 60$ kA before rolling over as the power supplied by the ohmic (OH) transformer coil (not shown) reaches the maximum. Eventually, at around $t = 78$ ms, a sudden collapse of plasma current known as a disruption is observed. A discussion of the disruption phenomenology is presented in section 5.2. Also shown is the loop voltage, V_{ℓ}, in figure 3.8b, induced on the surface of the plasma by the OH coil, and the plasma density, n_{e}, in figure 3.8c. As the plasma current increases, the edge safety factor, which is inversely proportional to the plasma current, $q(a) \propto I_{\mathrm{p}}^{-1}$, decreases, shown in figure 3.8d. Fluctuations in the poloidal field, δB_{θ}, shown in figure 3.8e, are observed when the value of the edge safety factor is close to rational values, that is, $q(a) = m/n$, where m and n are integers, describing the perturbation of the magnetic field on those surfaces. The poloidal and toroidal structure of these modes are analyzed using biorthogonal decomposition and the amplitude of the MHD modes, $\delta B_{m/n}$, are computed as shown in figure 3.8f. MHD modes with poloidal and toroidal mode numbers, $m/n = 4/1$, $3/1$ and $2/1$ are observed as the edge safety factor approaches values of $q(a) = 4$, 3 and 2 respectively. Such observations of modes with progressively decreasing m values are consistent with observations on tokamaks

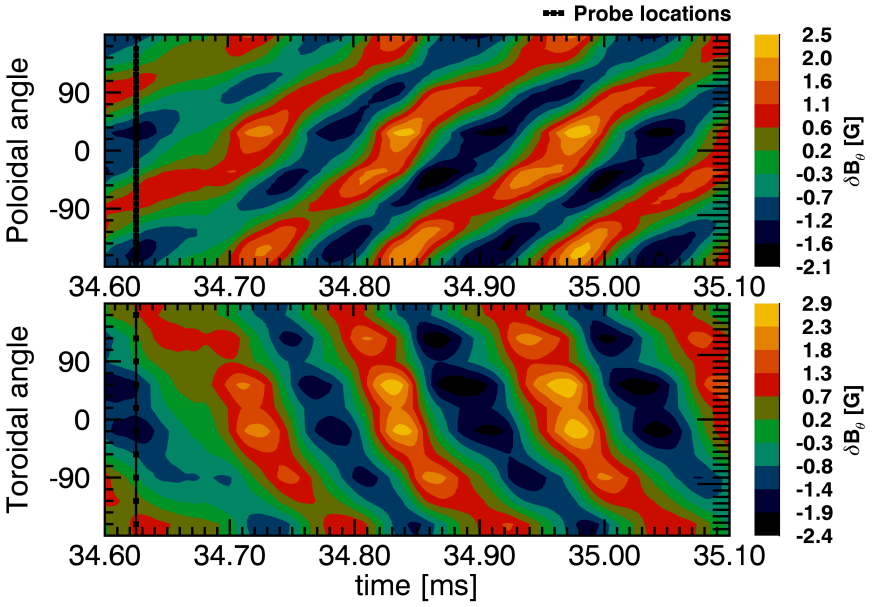

(a) $m = 2/n = 1$

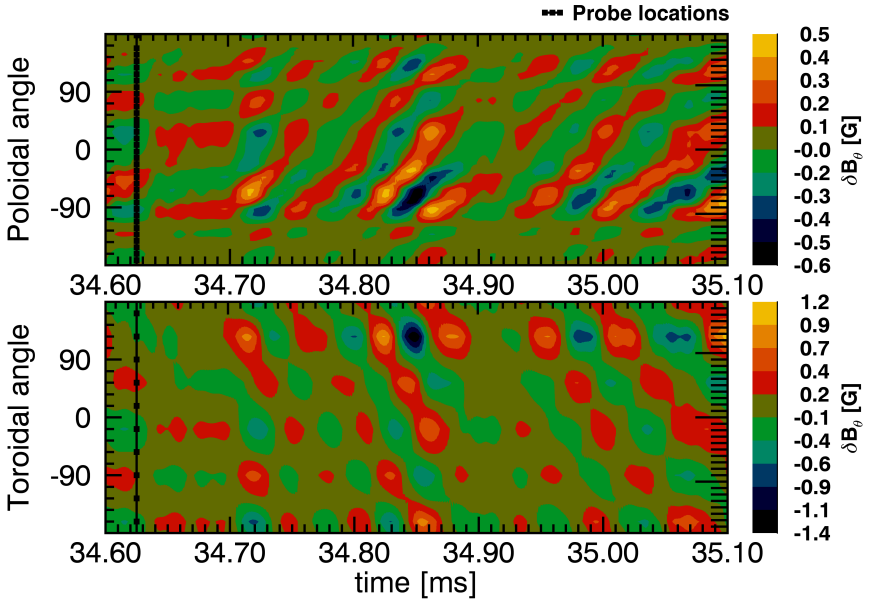

(b) $m = 4/n = 2$

Figure 3.7: The spatial and temporal modes corresponding to quadrature pairs of BD modes are multiplied and a signal in space-time coordinates is generated. Each mode is weighted by its singular value.(a) Contour plots obtained after combining the first two BD modes shows a rotating 2/1 mode (b) Third and fourth modes correspond to a rotating 4/2 mode.

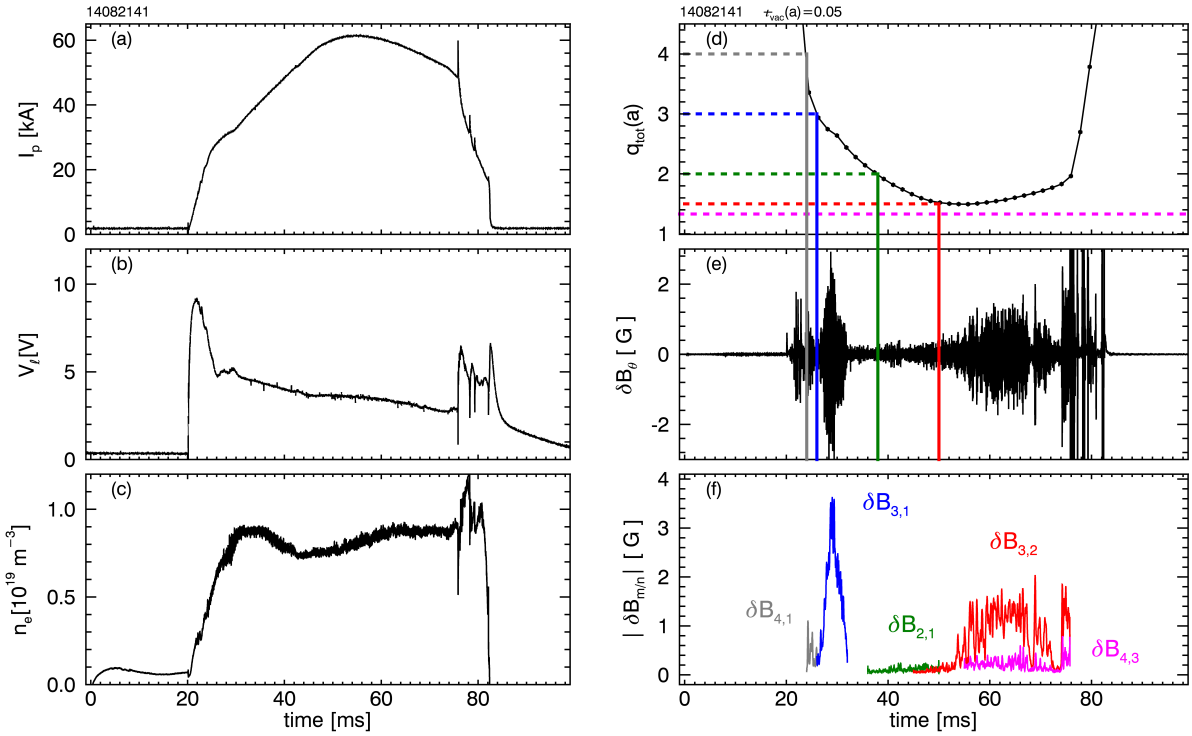

Figure 3.8: The time-evolution of various quantities for the CTH discharge 14082141 is shown. The panels (a)-(c) show the plasma current, loop voltage, and density respectively. The edge safety factor, computed using V3FIT equilibrium reconstruction is shown in panel (d). The total poloidal magnetic fluctuations, and the fluctuations corresponding to rational flux surfaces are shown in panels (e) and (f) respectively.

during current rise.[5,15,16] In the discharge shown in figure 3.8, as the plasma current reaches its peak value edge safety factor approaches a value of $q(a) = 1.5$ with an $m = 3/n = 2$ mode observed, shown in red in figure 3.8f. Even as the plasma current drops, the 3/2 mode amplitude remains large. This mode along with the 4/3 mode is typically observed before the disruption which is discussed in detail in chapter 5.

3.5 Summary

The structure of MHD modes is determined by Fourier analysis of magnetic perturbations in circular and cylindrical plasmas. The interpretation of the mode structure is complex because CTH plasmas are toroidal with stellarator non-axisymmetry. In this chapter we have

demonstrated the use of magnetic probes to determine the poloidal, m, and toroidal, n, structure of the perturbations in CTH plasmas. We employed a heuristic method, biorthogonal decomposition, to identify the dominant modes simply on the basis of the physical characteristics of their spatial structure. It will be shown in Chapter 4 that these modes indeed correspond to Fourier harmonics once we have taken into account the effects of toroidicity and stellarator non-axisymmetry.

References

[1] B. A. Stevenson. *3D Reconstruction of Plasma Equilibria using Magnetic Diagnostics on the Compact Toroidal Hybrid*. PhD thesis, Auburn University, 2011.

[2] J. D. Hanson, S. F. Knowlton, B. A. Stevenson, and G. J. Hartwell. Equilibrium and stability of current-carrying discharges in the non-axisymmetric cth experiment. *Contributions to Plasma Physics*, 50(8):724, 2010.

[3] M.G. Schlutt, C.C. Hegna, C.R. Sovinec, S.F. Knowlton, and J.D. Hebert. Numerical simulation of current evolution in the Compact Toroidal Hybrid. *Nuclear Fusion*, 52(10):103023, 2012.

[4] J. Hebert. *Simulations of the Compact Toroidal Hybrid Using the Finite Element Extended MHD Code NIMROD*. PhD thesis, Auburn University, 2015.

[5] I. H. Hutchinson. *Principles of Plasma Diagnostics*. Cambridge University Press, 2002.

[6] C. Nardone. Multichannel fluctuation data analysis by the singular value decomposition method. Application to MHD modes in JET. *Plasma Physics and Controlled Fusion*, 34(9):1447, 1992.

[7] T. Dudok de Wit, A.L. Pecquet, J.C. Vallet, and R. Lima. The biorthogonal decomposition as a tool for investigating fluctuations in plasmas. *Physics of Plasmas*, 1(10):3288–3300, 1994.

[8] J. S. Kim, D. H. Edgell, J. M. Greene, E. J. Strait, and M. S. Chance. MHD mode identification of tokamak plasmas from Mirnov signals. *Plasma Physics and Controlled Fusion*, 41(11):1399, 1999.

[9] D. Raju, R. Jha, P.K. Kaw, S. K. Mattoo, Y.C. Saxena, and ADITYA team. Mirnov coil data analysis for tokamak ADITYA. *Pramana - journal of physics*, 55(5):727–732, 2000.

[10] M. J. Hole and L. C. Appel. Fourier decomposition of magnetic perturbations in toroidal plasmas using singular value decomposition. *Plasma Physics and Controlled Fusion*, 49(12):1971, 2007.

[11] David A. Maurer, Daisuke Shiraki, Jeffrey P. Levesque, James Bialek, Sarah Angelini, Patrick Byrne, Bryan DeBono, Paul Hughes, Michael E. Mauel, Gerald A. Navratil, Qian Peng, Dov Rhodes, Nickolaus Rath, and Christopher Stoafer. High resolution detection and excitation of resonant magnetic perturbations in a wall-stabilized tokamak. *Physics of Plasmas*, 19(5), 2012.

[12] William H. Press, Saul A. Tukolsky, William T. Vetterling, and Brian P. Flannery. *Numerical Recipes in C: The Art of Scientific Computing*. Cambridge University Press, 2nd edition, 1992.

[13] Nadine Aubry, Fernando Carbone, Ricardo Lima, and Said Slimani. Wave propagation phenomena from a spatiotemporal viewpoint: Resonances and bifurcations. *Journal of Statistical Physics*, 76, 08 1994.

[14] T. Dudok de Wit. Enhancement of multichannel data in plasma physics by biorthogonal decomposition. *Plasma Physics and Controlled Fusion*, 37(2):117, 1995.

[15] R.S. Granetz, I.H. Hutchinson, and D.O. Overskei. Disruptive MHD activity during plasma current rise in Alcator A tokamak. *Nuclear Fusion*, 19(12):1587, 1979.

[16] John Wesson. *Tokamaks*. Oxford University Press, 4th edition, 2011.

Chapter 4

The structure of 3D magnetohydrodynamic modes in current-carrying CTH plasmas

4.1 Introduction

In the previous chapter we observed various MHD modes in a CTH discharge during the initial plasma current ramp phase, and as precursor to the disruption. The structure of observed MHD mode activity, without any prior information about the plasma equilibrium can be interpreted from the B-dot probe signals that measure the fluctuations in the poloidal magnetic field. The biorthogonal decomposition technique was employed to interpret the spatial and temporal structure of the MHD modes. The observed spatial structures correspond to helical perturbations on rational flux surfaces where the rotational transform is given by, $\iota = \frac{1}{q} = n/m$, where n and m are integers. For example, the fluctuations observed with helicity of $m = 3$, $n = 2$ mode are due to current perturbations on the rational surface $\iota = 2/3$, or $q = 3/2$, where m and n are the poloidal and toroidal mode numbers respectively. In this chapter we shall demonstrate that the fluctuations in the poloidal field, δB_θ, can be modeled as helical currents on these rational flux surfaces.

A literature survey of work done to understand the structure of MHD modes is presented in section 4.2. A recurring theme in the surveyed work suggests that most of the work is restricted to large aspect-ratio, $R_0/a >> 1$, circular, and low-β (β is the plasma pressure normalized to the magnetic field pressure) tokamak plasmas. In toroidal plasmas, a single Fourier harmonic in geometric coordinates does not adequately represent the poloidal structure of MHD modes. However, we will see that corrections to the path of the magnetic field line can be made so that Fourier analysis can still be employed. Interpretation of MHD activity in CTH is complicated by the fact that the equilibria are small aspect ratio, $R_0/a > 3.5$, and non-axisymmetric.

A model for the current distribution on rational surfaces is developed in section 4.3. The current distribution on a rational surface for an $m = 3$, $n = 2$ mode is obtained using measured fluctuations in the poloidal field, δB_θ, and the results are presented in section 4.4. Application of the current filament model to other MHD modes is presented in section 4.5.

4.2 Structure of MHD modes

MHD equilibrium implies a complete balance of forces at every point in space.[1] A static, isotropic plasma equilibrium is described by the force balance equation, Ampere's law and Gauss's law for magnetic field.

$$\begin{aligned} \mathbf{F} \equiv \mathbf{J} \times \mathbf{B} - \nabla p = 0, \\ \nabla \times \mathbf{B} = \mu_0 \mathbf{J}, \\ \nabla \cdot \mathbf{B} = 0 \end{aligned} \tag{4.1}$$

where, $\mathbf{J}$ is the current density, $\mathbf{B}$ is the equilibrium magnetic field, and p is the plasma pressure. The residual MHD force, $\mathbf{F}$, must vanish in equilibrium. Given an arbitrarily small perturbation to the equilibrium, it is deemed stable if the plasma/magnetic field system returns to its equilibrium state or oscillates about it. It is unstable if it tends to move away from the point of equilibrium. The MHD equilibrium is examined for stability[1–3] by introducing an arbitrarily small displacement, $\tilde{\xi}(\mathbf{r}, t)$, away from the equilibrium.

$$\tilde{\xi}(\mathbf{r}, t) = \xi(\mathbf{r}) e^{-i\omega t} \tag{4.2}$$

The structure of an MHD mode is embedded in $\xi(\mathbf{r})$. In a linear configuration like a cylindrical Z-pinch, a θ-pinch, or a screw-pinch, one can Fourier analyze the displacement with

respect to the ignorable coordinates, θ and z[3], and the displacement can be written as,

$$\xi(\mathbf{r}) = \xi_0(r) \exp\, i(m\theta + kz) \tag{4.3}$$

where m and k are poloidal and toroidal-like mode numbers, and (r, θ, z) are the cylindrical coordinates.

Analogous to the cylindrical case one can write the perturbation in toroidal geometry as,

$$\xi(\mathbf{r}) = \xi_0(r) \exp\, i(m\theta + n\phi) \tag{4.4}$$

where m and n are poloidal and toroidal mode numbers, and θ and ϕ are the corresponding geometric angles. However, these are not eigenfunctions of the perturbation in a toroidal plasma because, m is no longer a good quantum number since the equilibrium poloidal and toroidal fields, B_θ and B_ϕ, vary on an equilibrium flux surface.[4,5] In a screw pinch with circular cross-section, the poloidal and toroidal fields are constant on a flux surface and so the pitch of the magnetic field line is also constant on a flux surface. Therefore, the MHD modes which are identified in cylindrical harmonics due to the property that pitch of the magnetic field line is constant on a flux surface, cannot be described by a single Fourier harmonic in toroidal equilibria. Another way to say this is that the equilibrium depends on θ so it is no longer an ignorable coordinate. One way to deal with this problem is to "map a general equilibrium to a screw pinch like geometry such that the pitch angle is constant again".[5] This leads to a 'corrected' poloidal angle, θ^*, referred to as straight field line angle.

Considering large aspect-ratio, $R_0/r >> 1$, and a circular cross-section toroidal geometry, a correction was first derived by Merezhkin[4],

$$\theta^* = \theta - \lambda \sin\theta \tag{4.5}$$

where the parameter λ is a function of equilibrium quantities,

$$\lambda = \left(\beta_p + \frac{\ell_i}{2} + 1\right)\epsilon. \tag{4.6}$$

Here, β_p is the poloidal beta , which is the plasma pressure normalized to the magnetic pressure due to the poloidal magnetic field, ℓ_i is the internal inductance which has dependence on the distribution of current in the plasma, and $\epsilon = r/R_0$ is the inverse aspect ratio. For low aspect ratio, non-circular plasmas, higher order harmonics, $\sin 2\theta$ and $\sin 3\theta$, can be present in a θ^* correction, on account of elongation and triangularity.[5] This so-called Merezhkin correction has to be considered when the poloidal structure of MHD modes is analyzed using the magnetic pick-up coils in toroidal geometry.

The Merezhkin correction was successfully applied to determine poloidal mode numbers in the ASDEX tokamak.[6] The phase of measured fluctuations was assumed to have a fixed functional form, $\phi_i = m(\theta_i - \lambda \sin\theta_i) + \delta$, where the subscript, i, labels the B-dot probes that measure fluctuations in poloidal field. The probes were placed at a fixed toroidal angle around the inner circumference of the machine. Minimization with respect to measured data gave an optimal set of λ, phase, δ, and the poloidal mode number, m. A similar, comprehensive analysis to determine MHD modes in the plasma startup of the TFTR tokamak was demonstrated to work well.[7]

In low-β configurations, the MHD instabilities are driven by currents parallel to the equilibrium magnetic field lines.[3,8] MHD fluctuations measured by the B_θ-dot probes correspond to perturbations in the parallel current at rational surfaces. An analytical framework was first developed by Fussmann, et al.,[9] where the magnetic field of a helical surface current was determined for a large aspect ratio, circular cross section tokamak. It was shown that the poloidal mode number, m, was coupled to sidebands with mode numbers, $m \pm 1$. This is referred to as torodial mode coupling as it couples different poloidal modes corresponding to same toroidal mode number, n. The analysis by Kikuchi[10] takes into account the

Merezhkin correction and computes the poloidal flux due to the perturbed current on the rational surface. The current distribution is assumed to is given by,

$$\tilde{J_\phi}^* = J_{mn}\cos(m\theta^* + n\phi + \phi_0) \tag{4.7}$$

where $\tilde{J_\phi}^*$ is the perturbed toroidal current density, ϕ is the toroidal angle and ϕ_0 is the phase delay. J_{mn} is the amplitude of the perturbed currents on the m/n singular surface. The superscript, '*', indicates that straight field line angle, θ^*, is used instead of geometric angle θ.

Toroidal effects are dominant in low aspect ratio devices making the determination of the poloidal mode number more difficult. Helical surface currents have been employed in forward simulations of measured poloidal field fluctuations from toroidally coupled modes.[11] Poloidal mode numbers have been determined in non-circular plasma by least squares fit with observed MHD mode activity.[12] Helical filamentary currents were modeled as being along the magnetic field lines of the equilibrium of the MAST tokamak,[13] a spherical tokamak with low aspect ratio. The equilibrium in this case was axisymmetric and was reconstructed using EFIT[14]. The current distribution on the rational surface was obtained from a least squares fit to measured B-dot probe signals. By obtaining a fit at multiple instances in time, poloidal rotation and the growth amplitude of the mode were determined for a single tearing mode.

CTH is a low-aspect ratio tokamak-torsatron hybrid with five-fold stellarator symmetry as demonstrated in Chapter 2. Basic analysis of the observed MHD mode structures was presented in Chapter 3. Determination of poloidal mode number is complicated not just by enhanced toroidal effects due to its low aspect ratio, but also its inherent non-axisymmetry. However, reconstructions of CTH plasmas done using the V3FIT code[15] can be used to locate rational surfaces in the equilibrium. With this knowledge we can obtain the path of magnetic field lines in terms of straight field line angle. As we mentioned earlier, transformation to the straight field line angle incorporates the change in poloidal angle as a function of the

equilibrium parameters. This is akin to applying the analytic Merezhkin correction, but in a numerical sense. In straight field line coordinate system, the poloidal mode number corresponding to a single rational surface is represented by one Fourier harmonic. Obtaining a best fit with the measured B-dot probe signals allows us to associate observed MHD activity to a particular rational surface. The analysis presented in this chapter is limited to the consideration of equilibrium perturbations on one rational surface.

4.3 Development of the current filament model

The goal of the current filament model is to obtain a current distribution on a rational surface, that results in fluctuations, δB_θ, consistent with measurement. We use a χ^2 minimization technique[16] to minimize the discrepancy between the model and the measured signals within the uncertainty of the measurements, where χ^2 is defined as

$$\chi^2 = \sum_{i=1}^{N_D} \left[\frac{S_i^M - S_i^O}{\sigma_i} \right]^2 . \tag{4.8}$$

Here the measured signal is given by S_i^O, model signal is given by S_i^M, N_D is the number of diagnostics, and σ_i is the uncertainty in the measurement of δB_θ. The modeled signal for the i^{th} diagnostic coil is given by,

$$S_i^M = \sum_{j=1}^{N_f} M_{ij} I_j, \tag{4.9}$$

where N_f is the number of filamentary coils on a rational flux surface, M_{ij} is the mutual inductance between the i^{th} diagnostic coil and j^{th} filamentary coil, and I_j is the modeled current in the j^{th} filamentary coil. The current carried by each filament is modeled by

$$I_j = I_0 \sin(m\theta_j^* + \delta), \tag{4.10}$$

where m is the poloidal mode number of the MHD mode that we are to model; θ_j^* is a descriptor or label for the j^{th} filament chosen to be the poloidal position of the filament where it is initialized on the flux surface. I_0 and δ are variable parameters that are independent of position, not tied to a specific filament. The χ^2 optimization process involves varying these parameters until the mismatch between S_i^M and S_i^O is minimized. The number of filamentary coils is chosen to be much greater than the number of fit parameters. In our simulations, we shall arbitrarily pick the number of filaments, $N_f = 36$, equally spaced on a flux surface, whereas the number of fit parameters are just two, I_0 and δ. All the analysis and computation is done with the Interactive Data Language (IDL) software. χ^2 minimization is done using a publicly available code, MPFIT[17], an IDL nonlinear least squares fitting routine.

4.3.1 Choosing the equilibrium to model

MHD modes with multiple helicities are observed in a typical CTH discharge including, but not limited to, $m/n = 4/1,\ 3/1,\ 2/1$ and $3/2$. It is essential that the MHD mode we model have a strong signature on the B-dot probes because the model seeks to obtain a current distribution on the rational surface such that the magnitude and phase of δB_θ is consistent with the measured signal. Strong $4/1$ and $3/1$ kink modes are observed during the initial plasma current ramp phase when the corresponding rational surfaces are close to, or outside, the last closed flux surface of the plasma. In high current CTH plasmas where low-$q(a)$ disruptions are typically observed, a dominant $3/2$ tearing mode is present prior to the disruption and depending on the characteristics of a discharge, can be long-lived thus making it an ideal candidate to model.

Shown in the figure 4.1 from top to bottom are temporal evolutions of the plasma current I_p, edge safety factor q(a), $\dot{B}_\theta$ signal (from one probe) and the line averaged density n_e, for CTH discharge 14021473. As the plasma current increases the rotational transform at the edge, ι(a) $= 1/q(a)$, increases, with strong fluctuations observed on the B_θ probe throughout

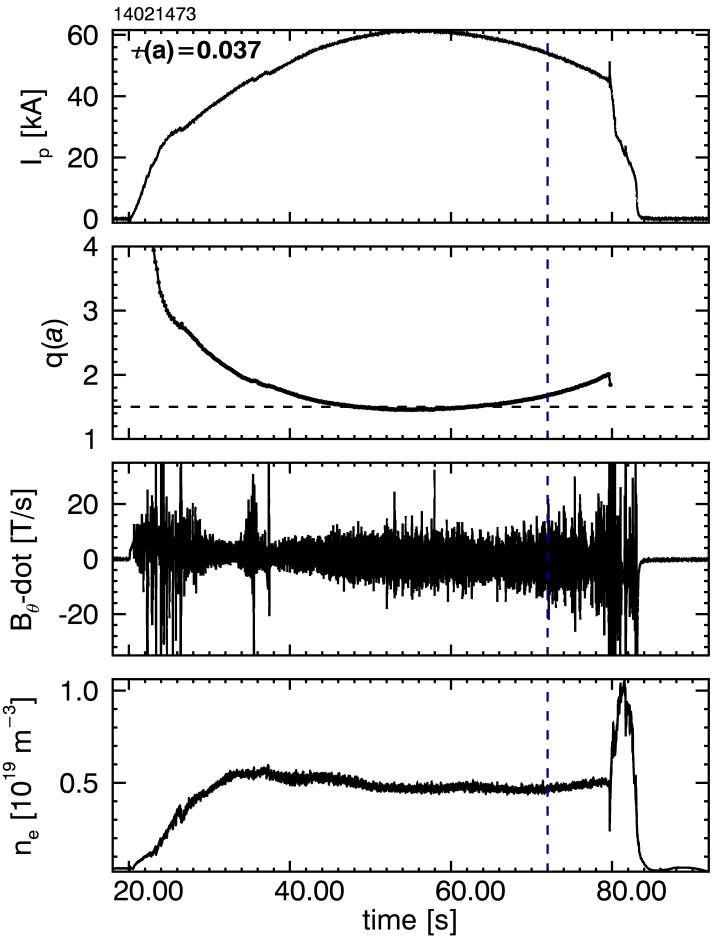

Figure 4.1: Plots from the CTH discharge 14021473 having $\iota_{\rm vac}(a) = 0.037$, with strong MHD activity is used to build a current filament model. The panels from top to bottom are the plasma current, $I_{\rm p}$; the edge safety factor $q(a)$; B-dot probe signal, $\dot{B}_\theta$; and the line-averaged density $n_{\rm e}$. The dashed horizontal line indicates a $q(a)$ of 1.5. The vertical line indicates the time when $q(a) > 3/2$, meaning the $\iota = 2/3$ surface is inside the LCFS and the observed MHD activity corresponds to a coherent $m = 3/n = 2$ MHD mode.

the discharge. The line averaged density, $n_{\rm e}$, is roughly flat during the discharge, until the disruption at $t = 79\,$ms. The vertical line shown at $t = 71.8\,$ms is when $q(a) > 3/2$, meaning the $\iota = 2/3$ surface is inside the last closed flux surface (LCFS). The observed MHD activity is due to $m = 3/n = 2$ mode, as will be shown later.

It is important that we choose a reconstruction of the shot when $\iota(a) \sim 2/3$ because our knowledge of rotational transform comes from equilibrium reconstructed using only external magnetic diagnostics. Such reconstructions are capable of providing accurate rotational

transform profiles near the edge of the plasma but they do not, in general, inform the profile shape deeper in to the plasma core.[18]

Figure 4.2 shows the rotational transform profile for the equilibrium at $t = 71.8\,\text{ms}$. The x-axis is the normalized toroidal flux represented by variable, s, in VMEC coordinates; $s = 0$ at the magnetic axis and $s = 1$ at the LCFS. The rotational transform $\iota(\text{s})$ is obtained for the discrete radial locations indicated in the plot. The $\iota(a) \sim 2/3 = 0.66\dot{6}$ surface, shown by the dashed line, is close to the edge of the plasma where the reconstructed equilibrium rotational transform profile is most trusted. The uncertainty in reconstructed rotational transform values is of the size of thickness of the line in figure 4.2.

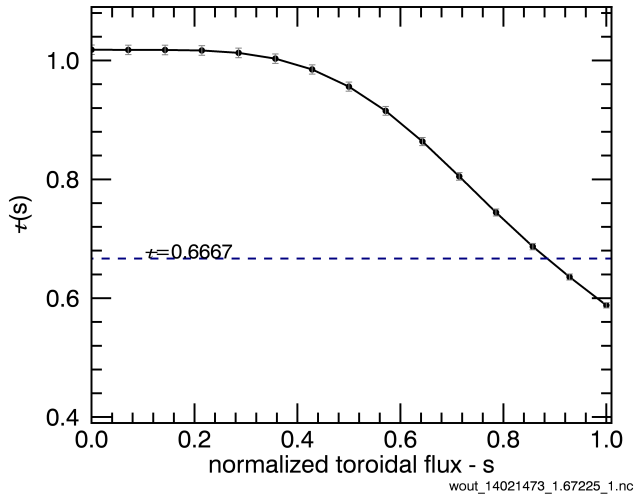

Figure 4.2: A graph showing the rotational transform profile, $\iota(\text{s})$, for an equilibrium with $\iota = 2/3$ close to the LCFS as indicated by the dashed horizontal line. The x-axis is the normalized toroidal flux which essentially describes radial distance from magnetic axis at $s = 0$ to $s = 1$ at the LCFS.

The total fluctuations in the poloidal field, δB_θ, measured by the poloidal and toroidal arrays of B-dot coils are shown in figure 4.3a. It is clear from the poloidal and toroidal structure that there is an $m = 3/n = 2$ mode present in the plasma. Flucutations corresponding to the 3/2 mode ($\delta B_{3,2}$) can be isolated from the total fuctuations using the biorthogonal decomposition method as was shown in chapter 3; these are depicted in figure 4.3b. A quick

look at the magnitude of MHD activity in both cases reinforces that the dominant MHD activity is associated with the 3/2 mode. We shall continue to use biorthogonal decomposition to isolate dominant mode activity for the analysis presented in this chapter.

4.3.2 Representation of magnetic field lines in VMEC

The paths of the magnetic field lines are obtained from the equilibrium computed by the **V**ariational **M**oments **E**quilibrium **C**ode (VMEC). VMEC is an ideal MHD equilibrium solver that uses a variational formulation of the MHD equilibria to seek an equilibrium that represents the minimum energy state[19]. It uses a steepest-descent procedure[16] to solve nonlinear moment equations that arise in the MHD equilibrium problem. The plasma energy given by W is minimized over a toroidal domain Ω_p,

$$W = \int_{\Omega_p} \left(\frac{B^2}{2\mu_0} + p \right) dV. \tag{4.11}$$

VMEC assumes the existence of 3-D nested flux surfaces and requires as input the magnetic fields from external magnet coils, a pressure profile, and a current profile. A static, isotropic plasma equilibrium is described by the ideal MHD equations shown in equation 4.1. The pressure, p, is a flux surface function. The nested toroidal flux surface geometry is expressed in flux coordinates, (s, u, v). The radial coordinate, s represents the fractional toroidal flux enclosed within a radial distance from magnetic axis, and is given by

$$s = \frac{\Phi}{\Phi_{LCFS}}, \tag{4.12}$$

where Φ is the enclosed toroidal flux within the flux surface labeled s, and Φ_{LCFS} is the enclosed toroidal flux within the LCFS. This gives $s = 0$ at the magnetic axis and $s = 1$ at the LCFS. The coordinate v is the geometrical toroidal angle, whereas u is a poloidal-like

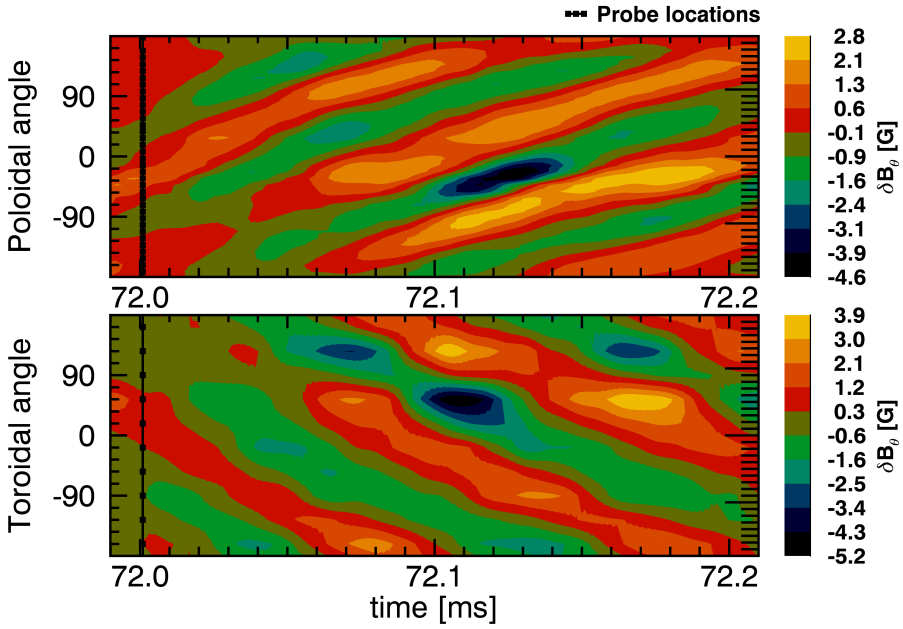

(a)

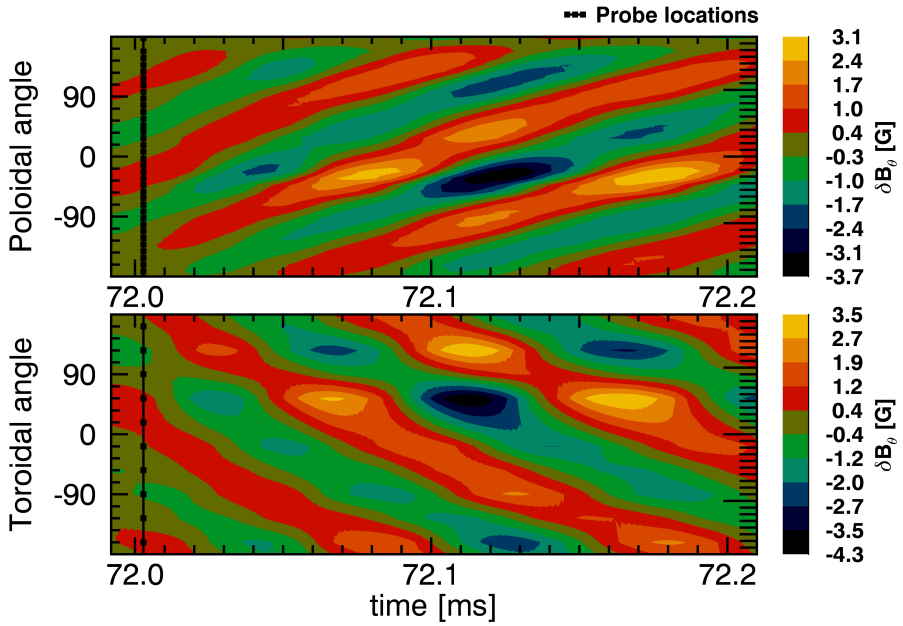

(b)

Figure 4.3: Contour plots show fluctuations in the poloidal magnetic field. (a) Figure shows total fluctuations, δB_θ, as measured by the poloidal and toroidal arrays of B-dot probes. (b) Flutuations corresponding to the $m = 3/n = 2$ mode, $\delta B_{3,2}$ obtained using biorthogonal decompsition dominate the total fluctuations in the poloidal field.

angle. VMEC uses an inverse coordinate representation of the cylindrical coordinates,

$$\begin{aligned} R &= R(s,u,v), \\ Z &= Z(s,u,v), \\ \phi &= v. \end{aligned} \tag{4.13}$$

The cylindrical coordinates (R, Z) are represented by Fourier sums given by equation 4.14. A function, $\lambda\,(s,u,v)$, also represented by a Fourier sum is introduced to make the magnetic field lines straight.

$$\begin{aligned} R &= \sum R_{mn}(s)\cos(mu-nv) \\ Z &= \sum Z_{mn}(s)\sin(mu-nv) \\ \lambda &= \sum \lambda_{mn}(s)\sin(mu-nv) \end{aligned} \tag{4.14}$$

This λ parameter will be used later in our work to determine starting locations for the current-carrying filaments on a rational flux surface. The conditions, $\mathbf{B}\cdot\nabla p = 0$ and $\nabla\cdot\mathbf{B} = 0$ can be satisfied by writing $\mathbf{B}$ in contravariant form,

$$\mathbf{B} = \nabla v \times \nabla\Psi + \nabla\Phi \times \nabla u^*, \tag{4.15}$$

where $2\pi\Psi(s)$ and $2\pi\Phi(s)$ are the poloidal and toroidal magnetic fluxes within the flux surface labeled s, and u^* is the poloidal-like angle that makes the magnetic field lines straight given by

$$u^* = u + \lambda(s,u,v) \tag{4.16}$$

In equation 4.16, λ is the same periodic stream function given by equation 4.14. Note that λ averages to zero over a magnetic surface. The local rotational transform, ι, is a flux surface

function in the (s, u^*, v) coordinate system, and is given by,

$$\iota(s) = \frac{\mathbf{B} \cdot \nabla u^*}{\mathbf{B} \cdot \nabla v} \tag{4.17}$$

Thus far we have introduced the coordinate system used in VMEC and details relevant to our application. A full description of VMEC can be found in the original paper by Hirshman and Whitson.[19] Mathematical details and development of a flux coordinate system is given in chapter 4 of the book by D'haeseleer et al.[20]

4.3.3 Current filaments on a rational surface

The current filaments in our model are placed on a rational surface along the equilibrium magnetic field lines. From our knowledge of a given equilibrium we can follow field lines on the surface of interest. We shall continue with the example equilibrium having the vacuum rotational transform profile given in figure 4.2. The flux surface of interest has $\iota = 2/3$. This surface lies between the two grid points of the reconstructed equilibrium as is evident from the reconstruction result. Interpolation between the grid points gives us the location of the flux surface as is shown in figure 4.4a with the dashed magenta line. VMEC output gives the Fourier amplitudes $R_{mn}(s)$, and $Z_{mn}(s)$ in equations 4.14. Thus interpolation from figure 4.2 gives a value of s that corresponds to the $\iota = 2/3$ surface which can be used to get the Fourier coefficients. The location of the flux surface is then simply computed from equation 4.14.

The path of a single magnetic field line on the flux surface labeled s is specified by its poloidal-like angle, u, and toroidal angle, v, in our flux coordinate system. This magnetic field follows a straight line path in (u^*, v) coordinates, where u^* is the straight field line angle. The rotational transform, $\iota(s)$, in this straight field line coordinate system is the slope of the magnetic field line, simply given by[20],

$$\iota(s) = \frac{du^*}{dv}. \tag{4.18}$$

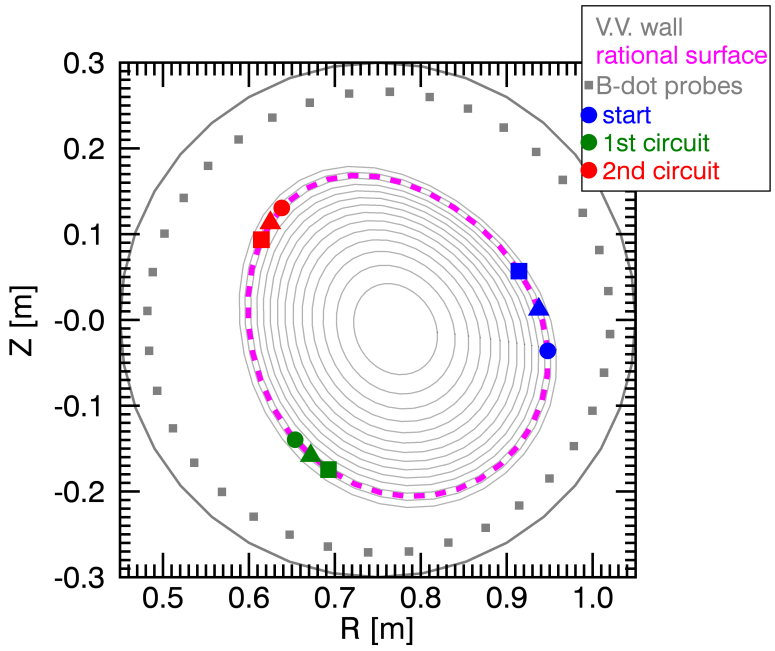

(a)

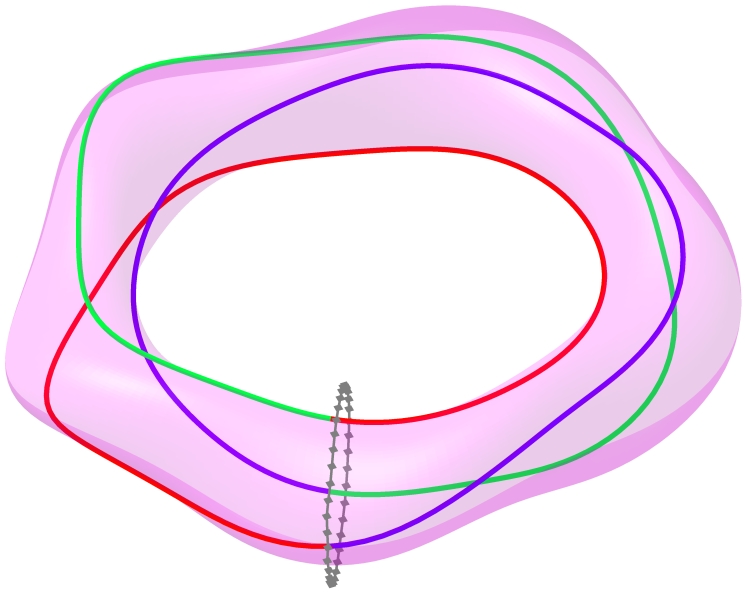

(b)

Figure 4.4: The path of a magnetic field line on the rational surface is shown. (a) Flux surfaces are shown at the toroidal angle where a poloidal array of B-dot probes is located. Shown with solid gray lines are the flux surfaces obtained from equilibrium reconstruction. The dashed magenta line indicates the rational surface with $\iota = 2/3$ whose position is obtained by interpolation. Positions of three magnetic field lines, distinguished with different shapes, are initialized at the outboard midplane (blue). Each field line comes back to its starting position after three toroidal and two poloidal circuits. (b) The path of a single magnetic field line is shown on the $\iota = 2/3$ surface. The field line is initialized near outboard mid-plane at the toroidal location of B-dot probes (shown in gray). The field line is colored blue for the first circuit and green and red for the second and third circuits respectively.

In our example we initialize a magnetic field line on the outboard side of the rational surface at the nominal toroidal location of one of the poloidal arrays of B-dot probes, $\phi = -117°$. As the field line advances toroidally, the poloidal location is determined through equation 4.18. Because the poloidal mode number is three and toroidal mode number is two, after 3 toroidal transits the magnetic field line completes two poloidal transits and returns to the point of initialization. This is shown in figure 4.4b, where each toroidal circuit is indicated by a different color.

Now that we can trace the path of a single magnetic field line on a flux surface, recall that the end goal is to obtain a current distribution on the rational surface given by equation 4.10. We shall now describe the procedure to trace multiple field lines on the same rational surface, with starting locations of the magnetic field lines obtained by integrating 4.19,

$$u^* = \iota(s) \cdot v + u_0^*, \tag{4.19}$$

where u_0^* is the initial condition. Transformation of these straight field line coordinates to flux coordinates, and subsequently to the cylindrical coordinates, (R, Z), gives the path of the filamentary circuit which will used in further modeling work. This is achieved by determining the initial condition in the flux coordinates, u_0, corresponding to that in the straight field like coordinates, u_0^*, as given by equation 4.16. This is shown in figure 4.5 for three different values of toroidal angle coordinate, v, while the radial coordinate, s, specifies the radial location of the $\iota = 2/3$ flux surface. Notice that the values of u and u^* go from 0 radians to 4π radians corresponding to the two poloidal circuits made by the field line on the flux surface. For a given u_0^* we use a root-finding procedure to determine u.

Figures 4.6a and 4.6b show plots of the magnetic field lines in flux coordinates (or VMEC coordinates) and straight field line coordinates respectively. They are initialized at the location of the poloidal array of B-dot probes, $\phi = -117°$, to be equally spaced in flux coordinates and they follow a straight line path with slope being the inverse of the rotation

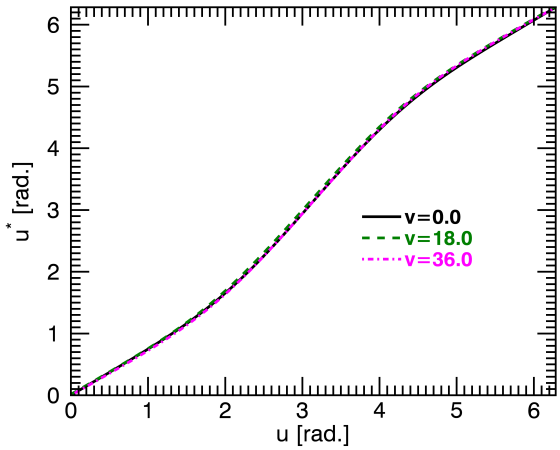

Figure 4.5: The functional dependence of the straight field line coordinate, $u^*(s,u,v)$, on the flux coordinate, u, is shown for three different values of toroidal angle, v, and radial coordinate, s, corresponding to the position of the rational surfaces, $\iota(s) = 2/3$. A root finding procedure is used to transform from the straight field line coordinates to the flux coordinates. Note that all the magnetic field lines are initialized at the location of the poloidal array of B-dot probes, $\phi = -117°$, as seen from the negative intercept on Y-axis.

number of the field line or $1/\iota(s) = 3/2$ for this rational surface. Note that $u = 0$ on the outboard mid-plane and $u = \pi$ on the inboard mid-plane. Each field line makes three toroidal circuits as it goes around twice poloidally. On the other hand, in the VMEC coordinates, they do not follow a straight line path. There are 36 magnetic field lines initialized in this example. The field lines get closer as they move inboard and farther apart on the outboard. This is reflected in the figure 4.4a where the field lines are closer on the inboard than the outboard side of the plasma.

4.3.4 Calculation of the mutual inductances between current filaments and the B-dot probes

Now that we have in place the filamentary circuits on the rational surface, we shall determine the poloidal field that would be generated by a finite current in each of these circuits, at the location of the B-dot probes installed in CTH. This is done by computing the mutual inductance, M_{ij}, between the jth current filament and the ith B-dot probe, which will allow us to compute the model signal for the ith B-dot probe, S_i^M(see equation 4.9).

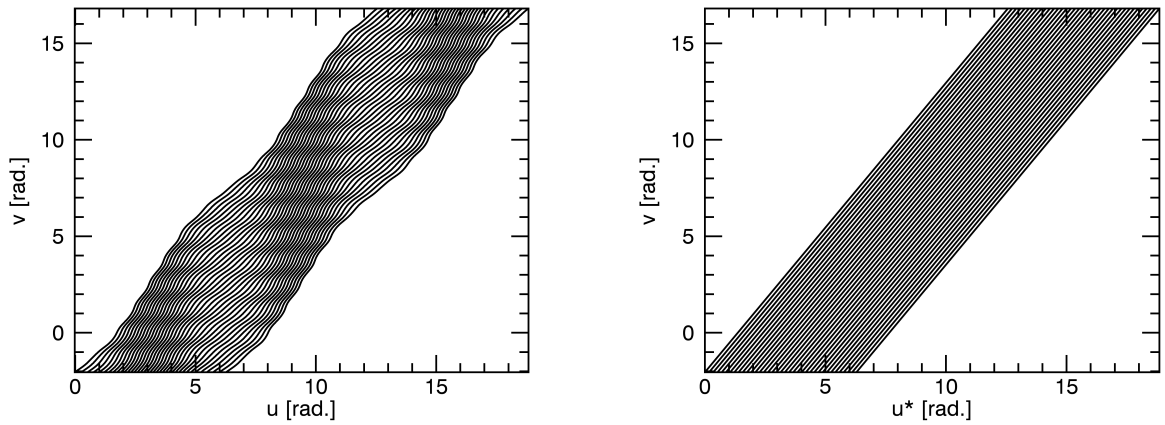

(a) (b)

Figure 4.6: Current filaments are initialized on a rational flux surface, s, with $\iota = 2/3$, equally spaced in flux coordinates. (a) Current filaments in VMEC coordinates (u, v) are plotted for the rational flux surface. Each filament makes 3 toroidal circuits as it goes around twice poloidally. The field lines are closer on the inboard mid-plane, $u = \pi$, and farther on the outboard mid-plane, $u = 0$. (b) The field lines follow a straight line path in flux coordinates and are chosen to be equally spaced. Their slope is the $1/\iota(s) = 3/2$ for the chosen rational surface.

The mutual inductances are computed using the V3RFUN code[21], which is a part of V3FIT suite of equilibrium reconstruction codes. Details of V3RFUN relevant to the equilibrium reconstruction process can be found in the thesis by Stevenson[22], and in the paper by Hirshman, et al[21]. It takes as input, the geometrical descriptions of the external field coils and diagnostic coils, and generates an output with coil and plasma response functions. The V3RFUN output is then used by the V3FIT code. The field coils in V3FUN parlance are the ones that produce the external magnetic fields. The field coils can be any of the numerous types of magnet coils on CTH including helical field coils, toroidal field coils, etc. Eddy currents in structures like vacuum vessel or coil frame can also be modeled as discrete field coils. The second class of coils are the diagnostic coils that carry currents induced by time-varying magnetic fields. Diagnostic coils could be magnetic probes, Rogowski coils, flux loops and saddle coils.

The V3RFUN code is used to compute the diagnostic response functions and store them in separate files making up a database, which can be employed later to compute plasma response for any given equilibria. In our present analysis we are interested in the coil response function computed by V3RFUN given by equation 4.20.

The V3FUN code computes two kinds of response functions, coil response functions, and plasma response functions. The coil response functions are defined by

$$S_i = \sum_j R_{ij} I_j, \tag{4.20}$$

where S_i is the signal in the ith diagnostic coil, R_{ij} is the response of the ith diagnostic coil to the jth field coil, and I_j is the current in the jth field coil. The response function is just a mutual inductance coefficient between the diagnostic coil and the field coil. The units of a coil response function depends on the kind of diagnostic coil. Diagnostic coils measure the total flux, in the units of Weber, or can make point measurements, with units of Tesla. The plasma response function is defined by

$$S_i = \int_{V_\mathrm{p}} \mathbf{J}_\mathrm{p}(\mathbf{r}') \cdot \mathbf{R_i}(\mathbf{r}') \mathbf{dr}' \tag{4.21}$$

where S_i is the signal in the ith diagnostic coil, $\mathbf{J}_\mathrm{p}(\mathbf{r}')$ is the current density in the plasma, $\mathbf{R_i}(\mathbf{r}')$ is the plasma response function for ith diagnostic coil and V_p is the volume of the plasma.

We model the current distribution on the rational surface with 36 filamentary coils. Figure 4.7 shows four current filaments on $\iota = 2/3$ surface, each of them making a complete electrical circuit by returning to their point of origin. Also shown is the poloidal array of B-dot probes for which we are to compute the mutual inductances with each of the filamentary coils. The Details of input files used to execute of V3RFUN code is given in appendix C.

Contour plots of the computed mutual inductances between the B-dot probes and the current filaments, M_{ij} (in equation 4.9), are shown in figure 4.8. Figure 4.8a shows the

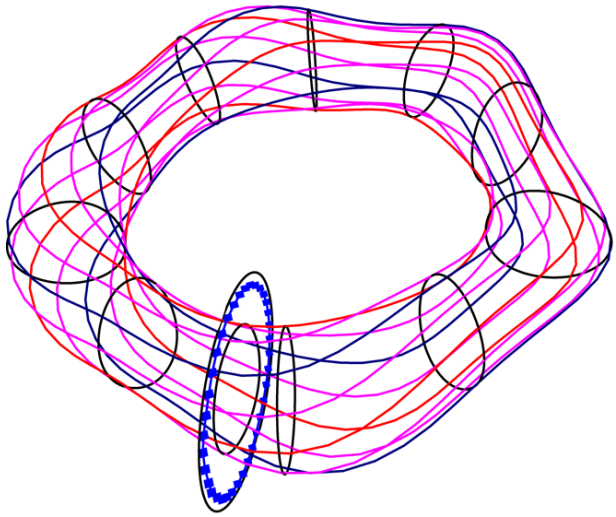

Figure 4.7: The mutual inductance is computed between the shown current filaments on the rational surface and the poloidal array of B-dot probes. Only four of the 36 current filaments for which the mutual inductances are computed are shown here. Each of the filamentary coils is initialized on the $\iota = 2/3$ surface at the toroidal location of the B-dot probes. The path of each filamentary coil completes an electrical circuit, i.e. they begin and end at the same point in space. Also shown is the rational surface on which these current filaments lie, at the location of the B-dot probes, and then every half-period and full-period locations of CTH stellarator symmetry.

mutual inductances for the probes in the poloidal array of B-dot probes and 4.8b shows mutual inductances for the toroidal array. The white dots along the abscissa show locations where the current filaments are initialized in geometric coordinates and the white squares along the ordinate show the poloidal angle for the B-dot probes in the array. Note that the geometrical poloidal angle is defined as 0° on the outboard side and 180° on the inboard side of the vacuum vessel mid-plane. The contours represent the mutual inductances between the B-dot probes and the filaments in the units of Tesla/Ampere. Note that the current filaments are not equally spaced in the geometric coordinates, however they are spaced uniformly in the straight field line coordinates as described previously.

The fact that filaments are on the rational surface having poloidal mode number, $m = 3$, is reflected in the periodicity of the mutual inductances. For a particular B-dot probe in the poloidal array, say the one located on outboard mid-plane (0°), the mutual inductance is maximum at three locations and minimum at three, implying an $m = 3$ poloidal structure.

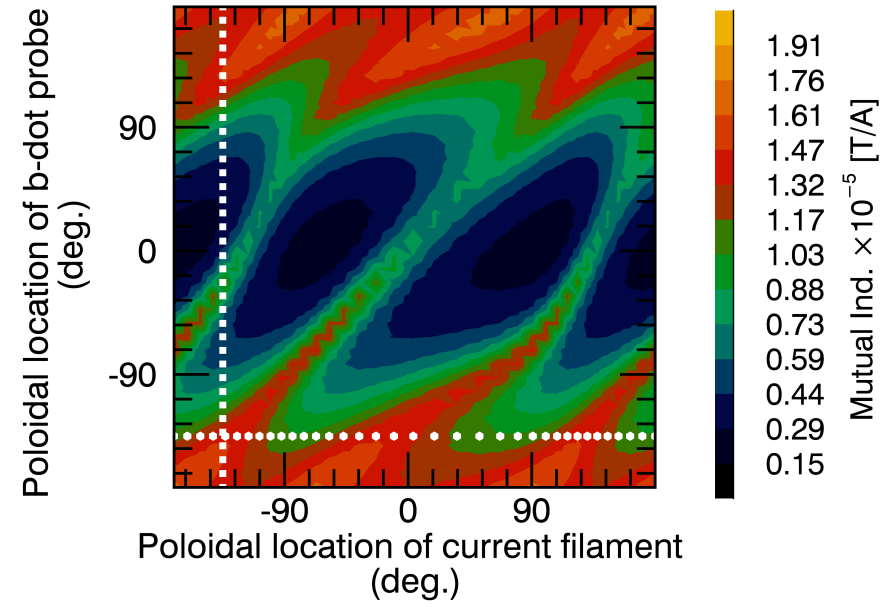

(a)

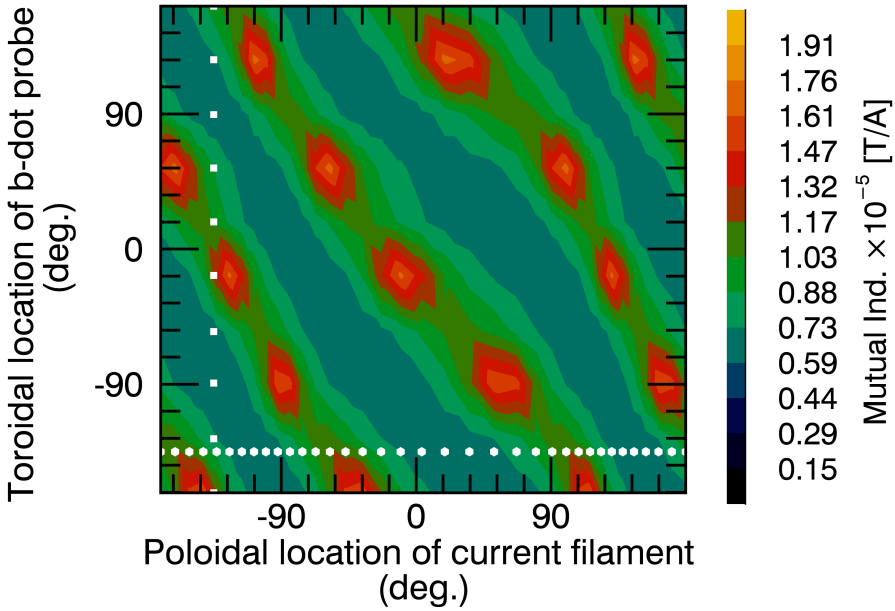

(b)

Figure 4.8: The computed mutual inductances between the current filaments located on a $q = 3/2$ rational surface and the B-dot probes of (a) the poloidal array, (b) the toroidal array. Along the x-axis are the poloidal locations where the current filaments are initialized (white circles) and along the y-axis are the (a) poloidal, and (b) toroidal angles of the B-dot probes in their respective arrays (white squares). The poloidal angle is 0° on the outboard and 180° on the inboard side.

Also, it follows from geometry that the closer the current filaments and the B-dot probes are to one another, the larger is their mutual inductance. For example the filament located on outboard mid-plane has the largest mutual inductance with the B-dot probe located near outboard mid-plane. However, it can also be seen that the mutual inductance is large for all the B-dot probes located approximately thirty degrees on either side of the inboard mid-plane. This is testament to the fact that the magnetic field lines, and hence the current filaments, spend more time on the inboard side of the vacuum vessel as they make toroidal transits.

The mutual inductances for the toroidal array shown in figure 4.8b are also reflective of the helicity of the surface on which they are located. Considering a particular current filament, the mutual inductance has two peaks in the toroidal direction. Whereas, for a particular probe the mutual inductance has three peaks and troughs. The locations at which hot spots are observed in the mutual inductance, the magnetic field line is closest to the B-dot probe, that is close to the top of the machine. This happens at five different toroidal locations, demonstrating five-fold periodicity of CTH equilibrium.

4.4 Determination of the current distribution on a rational surface

Now that all the necessary ingredients of the recipe to obtain a current distribution on rational surface have been obtained, $I(\theta^*)$, modeled by equation 4.10, a χ^2 minimization is done to determine model signals, S_i^M, that best match the observed signal, S_i^O. The current distribution is determined using measurements from one poloidal array and one toroidal array of B-dot probes. Although, χ^2 is the quantity that is minimized to obtain the fit, the results will be compared in terms of a reduced χ^2_R, defined as,

$$\chi^2_R = \frac{\chi^2}{d} \tag{4.22}$$
$$d = N_D - N_F$$

where d is the number of degrees of freedom, and is the difference between the number of diagnostics, N_D and the number of fit parameters, N_F. For our case there are 36 poloidal probes and 10 toroidal probes, so $N_D = 46$. We are fitting I_0 and δ so $N_F = 2$, thus $d = 44$ for this system.

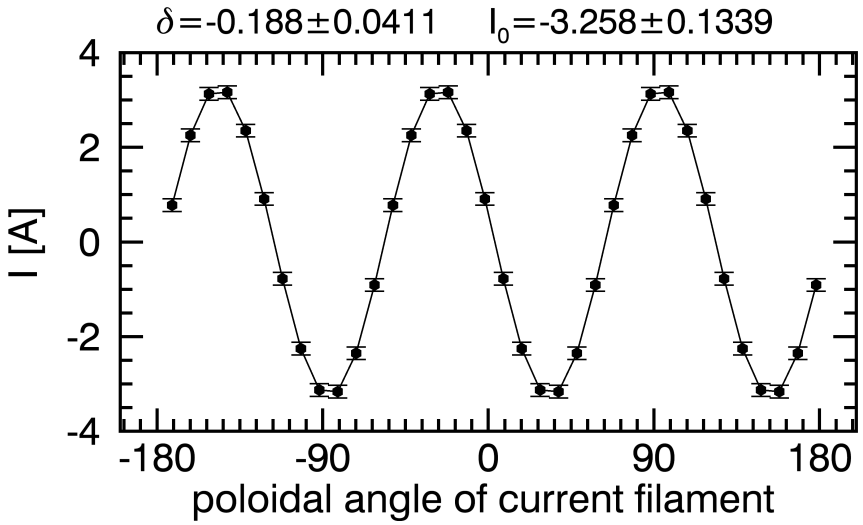

Figure 4.9: The current distribution on the $\iota(s) = 2/3$ surface obtained after χ^2 minimization of discrepancy between the measured and computed fluctuations, δB_θ. The determined parameters of the fit are δ (radians), and I_0 (Amps). respectively.

For the MHD mode of interest here, the current distribution that results in the minimum χ^2 is shown in figure 4.9. The parameters of the current distribution that are varied in the fitting process are the phase, $\delta = 10.7 \pm 0.26$ degrees, and the magnitude of the current $I_0 = 3.25 \pm 0.133$ Amps. The dashed blue line in figure 4.10 is the experimentally measured signal at $t = 71.8$ ms, which is at the center of the time window in the data shown in figure 4.3b. The model signal, which is determined at the location of the B-dot probes, is shown with solid black line. The χ^2_R of the fit is about 1.8. For a fit that is within the standard deviation of the measurement, σ_i, the χ^2_R would be 1. The error bars on the measurement in figure 4.10 indicate an estimated σ_i. The error in the model signal, S_i^M, is much smaller than the error in measurement. The uncertainty in the computed parameters of the current distribution, δ and I_0, are obtained by propagation of measurement uncertainty σ_i.

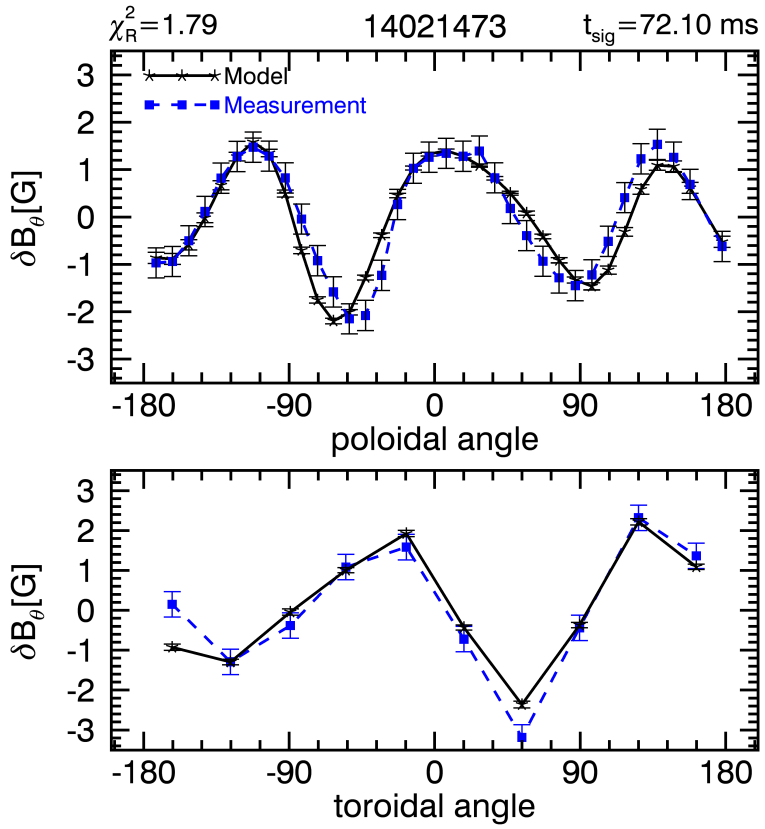

Figure 4.10: Comparison of model and the measured signals for poloidal($m = 3$) and toroidal mode structure($n = 2$). The model signals are indicated by solid black lines and the measurement by dashed blue lines. The symbols represent the poloidal/toroidal location of the B-dot probes. Error bars on respective trend lines indicate uncertainty in the measurement and the model.

It is a challenge to make an appropriate choice of σ_i because here it does not reflect the uncertainty of our measurement of δB_θ. That is, it does not represent the absolute uncertainty of the measured voltage across the leads of B-dot probes. Instead, we have chosen the uncertainty to be about 10% of the largest measurement of δB_θ amongst all the measurements. This means σ_i is chosen to be same for all the probes. This value is much smaller than the standard deviation of the signal over $2-3$ cycles. The $m = 3/n = 2$ mode shown in this example rotates in the laboratory frame with a frequency of $f \sim 12\,\text{kHz}$. Such a choice of σ_i is found to be a reliable indicator of the goodness of fit. Hence χ^2_R will be used to make a comparison of fits across shots with varying MHD mode amplitudes.

We have thus developed a method to obtain the distribution of current on a rational surface that generates a poloidal magnetic field consistent with the measurement.

4.5 MHD modes observed in the plasma current rise

MHD modes with decreasing q are observed during the plasma current rise phase in CTH. Figure 4.11 shows a discharge where the edge safety factor decreases from $q(a) = 50$ when $I_\mathrm{p} = 0$ to $q(\mathrm{a}) \sim 1.7$ at peak plasma current. Shown in figure 4.11 from top to bottom are the plasma current, the edge safety factor obtained from equilibrium reconstruction, and δB_θ as measured by one of the B-dot probes. As the plasma current increases, the edge safety factor assumes different rational values as highlighted by the horizontal dashed lines. Note that the ohmic part of the discharge begins at $t \sim 20\,\mathrm{ms}$.

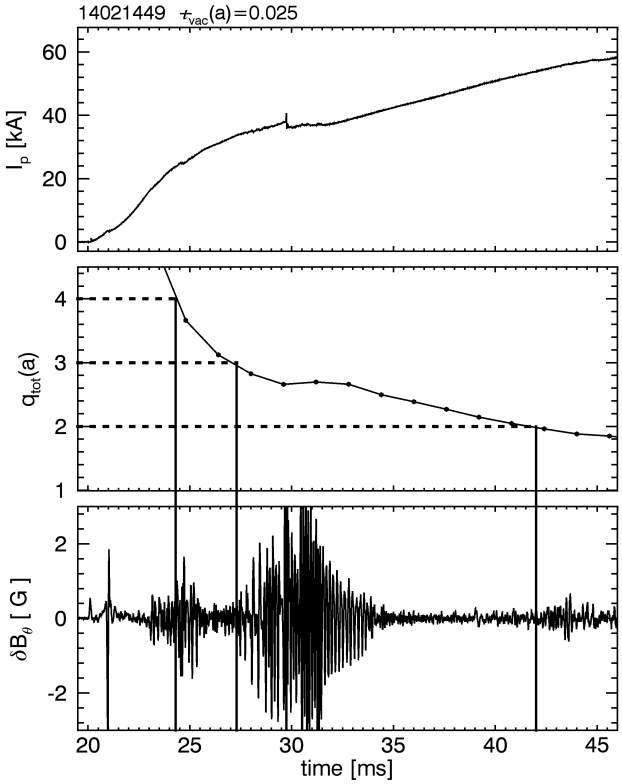

Figure 4.11: Multiple MHD modes are observed during the current rise phase of a CTH discharge. As the plasma current increases (top panel) the edge safety factor assumes rational values, $q(a) = 4, 3, 2$, indicated by dashed horizontal lines in the middle panel of the figure. In the lower panel, poloidal magnetic field fluctuations, δB_θ corresponding to each MHD mode is indicated by vertical bars.

In this section, current filament models for the $m/n = 4/1$, $3/1$ and $2/1$ modes are obtained using the method outlined in sections 4.3 and 4.4. The sinusoidal current distribution on the rational surface is given by $I = I_0 \sin(m\theta^* + \delta)$ and the fit parameters of the χ^2 minimization are I_0 and δ.

4.5.1 The 3/1 mode

The value of edge safety factor is greater than 3 at $t = 27\,\text{ms}$, as indicated by the horizontal line in figure 4.11. As the plasma current is increases, the edge safety factor evolves to a value $q(a) < 3$, thus pushing the $q = 3$ rational surface out of the plasma. The equilibrium $q-$profile at the time when the surface is internal to the LCFS is shown in figure 4.12a. An equilibrium reconstruction is performed with a fixed current profile and using only the external magnetic diagnostics. The x-axis of figure 4.12a is the square root of s, where s is the normalized toroidal flux. The square root of s can be thought of as minor radius of the flux surface normalized to average minor radius of the plasma. The contour plots of δB_θ measured by the poloidal and toroidal arrays of B-dot probes are shown in figure 4.12b.

The mutual inductances computed from the equilibrium are given in figure 4.13. Again, the $m = 3/n = 1$ mode structure is embedded in the mutual inductances. The current distribution on the rational surface is given by the model, $I_j = I_0 \sin(3\theta_j^* + \delta)$, where the values of $I_0 = 0.66\,\text{Amps}$ and $\delta \sim 12.8^\circ$ are obtained from the χ^2 minimization. The resulting χ^2_R is 7.63. A comparison between the modeled signals and the measurement is shown in figure 4.14. The model signals and measurement are a good match for the toroidal mode structure. However, poloidal mode fit is poor, as indicated by a large overall χ^2_R.

A quick look at the total fluctuations in figure 4.11 indicates that the amplitude of MHD activity increases at about $t = 27\,\text{ms}$ as the 3/1 surface exits the plasma. At this time the edge safety factor is decreasing and the minor radius of the 3/1 surface is increasing as it is moving closer to the B-dot probes. Biorthogonal decomposition of the measurements confirm a 3/1 structure to these perturbations. Fourier mode amplitudes of the dominant

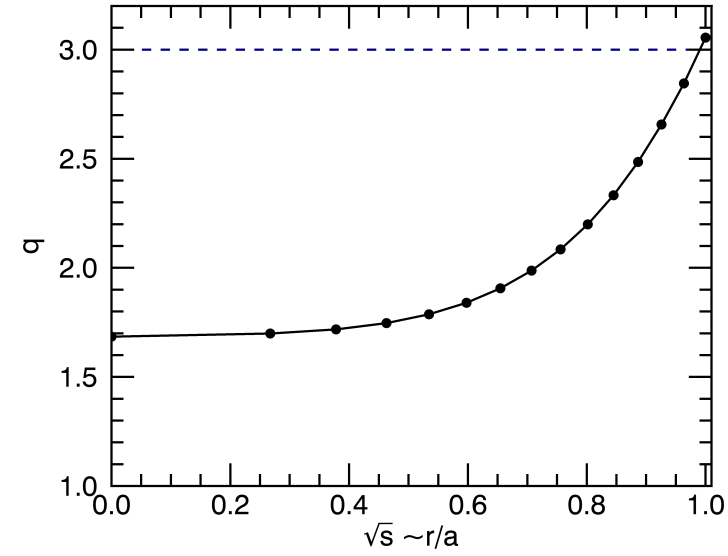

(a)

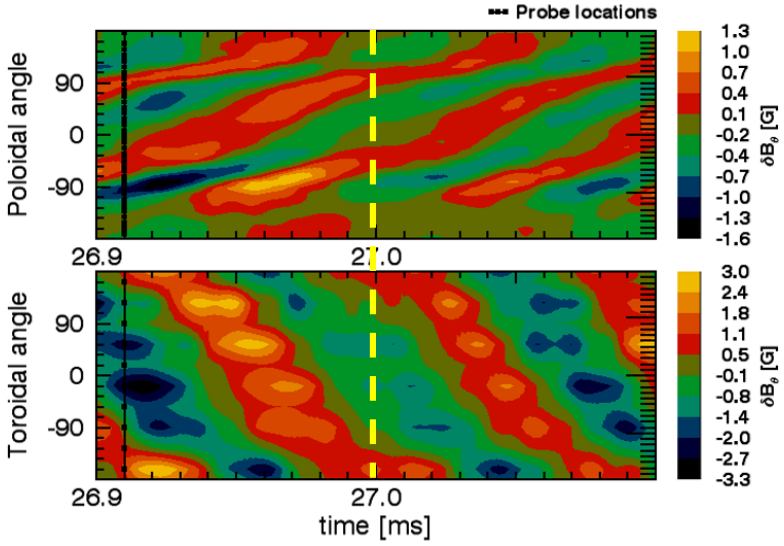

(b)

Figure 4.12: (a) The $q-$profile obtained from equilibrium reconstruction shows that the 3/1 surface is just inside the plasma. The x-axis is a radial-like variable, indicative of radius of the flux surface normalized to average minor radius of the plasma. Each point in the plot indicates a flux surface location where the reconstruction was computed for 15 magnetic flux surfaces within the plasma. The horizontal line indicates that the $q = 3$ surface lies just inside the LCFS (b) The total fluctuations, δB_θ, measured by the poloidal and toroidal arrays of B-dot probes indicate that a rotating $m = 3/n = 1$ mode is present. The time of equilibrium reconstruction is indicated by a dashed yellow line at the center of the window.

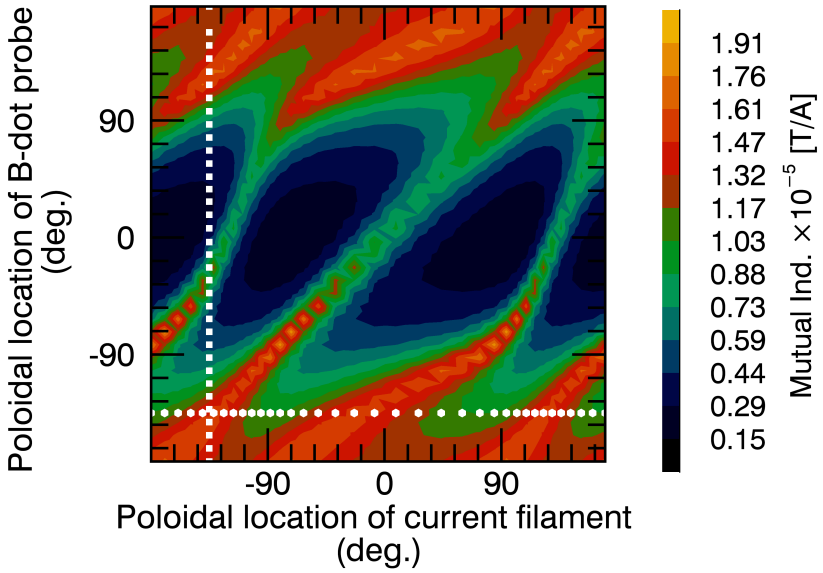

(a)

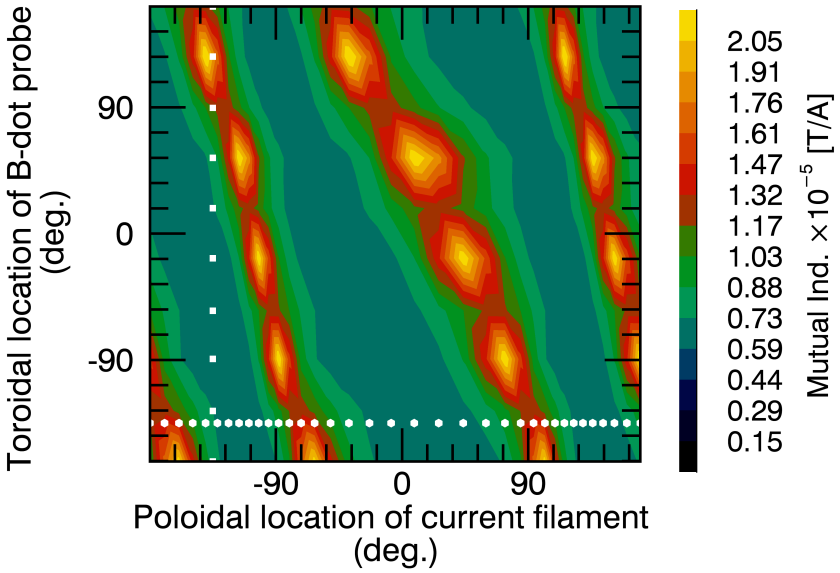

(b)

Figure 4.13: Mutual inductances between the current filaments on $q = 3$ surface and the B-dot probes in (a) the poloidal array (b) the toroidal array. The poloidal ($m = 3$) and toroidal structure ($n = 1$) is embedded in the mutual inductances.

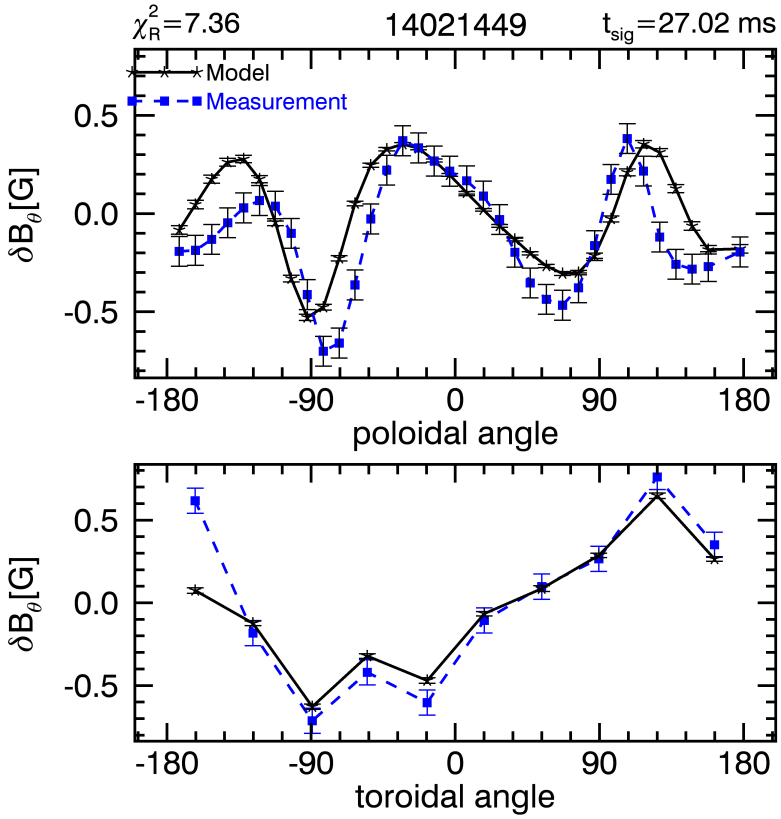

Figure 4.14: The model signals and measurement are a close match in terms of the toroidal structure (bottom panel). The poloidal fit is poor thus giving a large χ^2_R for the overall fit(top panel).

MHD modes are shown in figure 4.15 and are also indicative of this. The shaded region in the plots show the time when the equilibrium reconstruction is done with the 3/1 surface close to the LCFS. The mode amplitude is less than 0.5 G when the 3/1 surface is internal to the LCFS and increases to about 10 G before decaying. The dominant Fourier harmonics corresponding to what would be an $m = 3$ in a cylinder, are represented by $m = 3$ and $m = 2$. The dominant toroidal mode number is $n = 1$.

We shall construct a current filament model for the 3/1 mode when it is external to the LCFS, using equilibrium information obtained when the mode is internal. Equilibrium reconstruction gives the correct location of the rational surface only when it is internal to the LCFS. In our case, when the surface is external to the plasma, strong fluctuations are

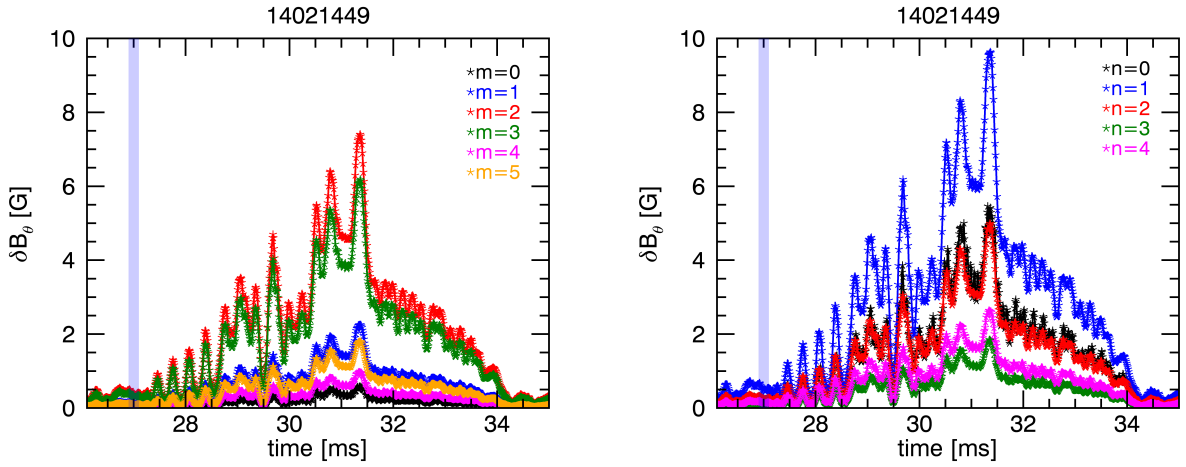

(a) (b)

Figure 4.15: Fourier mode amplitudes of poloidal (a) and toroidal (b) mode structures is shown for the dominant MHD modes obtained from biorthogonal decomposition. The $m = 3$ and $m = 2$ modes are the dominant poloidal harmonics whereas the $n = 1$ toroidal harmonic is dominant. The shaded area at $t = 27\,\text{ms}$ indicates the time when the mode is inside the LCFS. It exits the plasma later in time when the MHD mode amplitude gets large in amplitude.

measured by the B-dot probes. We shall assume that the shape of the rational flux surface does not change much and hence we assume that the mutual inductances are unchanged. So the larger mode amplitude will simply result in a larger current, I_0, on the rational surface. The resulting $\chi^2_R(t)$ plotted in figure 4.16a shows that a better fit is obtained when the mode is external to the plasma. The large spike in χ^2_R after $t \sim 29.5\,\text{ms}$ corresponds to a sudden change in MHD activity also evident in the Fourier harmonics in figure 4.15. The χ^2_R is less than 2 after $t = 30\,\text{ms}$ and the $q(a) \sim 3.2$ (see fig. 4.11). An example of such a fit is shown in figure 4.16b, where the model and measurement are both within the variance of measured signals σ_i resulting in $\chi^2_R < 1$. The amplitude of the current in this case $I_0 = 4.7\,\text{A}$ and phase $\delta = 43°$.

4.5.2 The 4/1 mode

Next, we shall obtain a perturbed current on the $q = 4$ surface that results in measured fluctuations in the poloidal field. This mode is short-lived compared to 3/1 mode

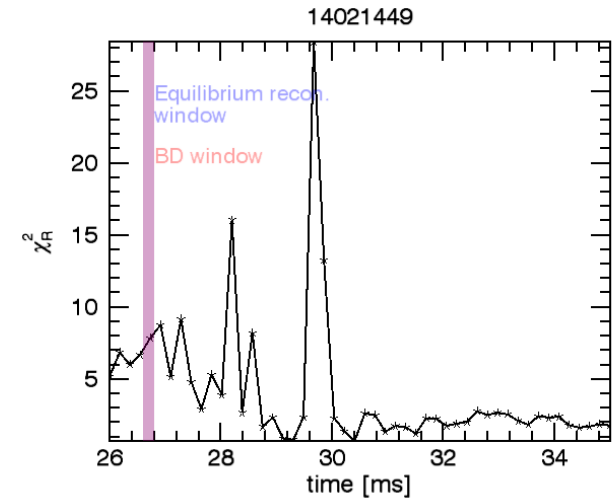

(a)

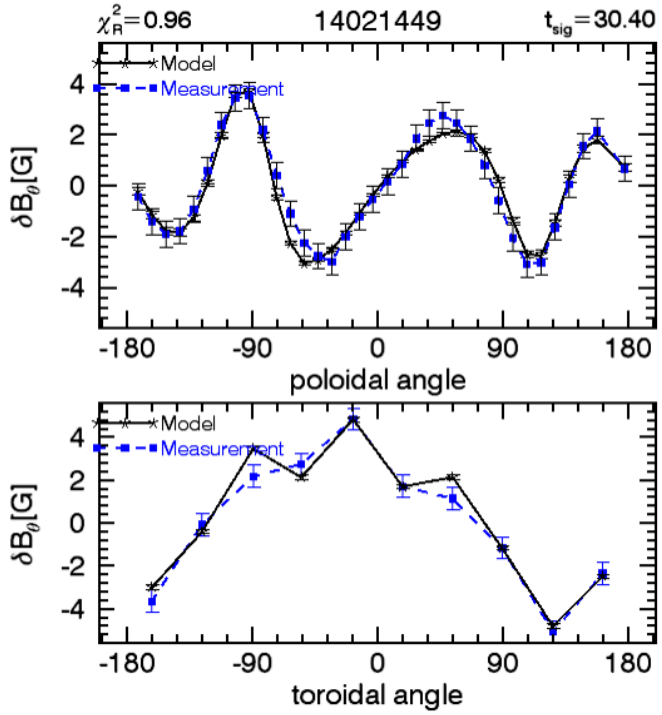

(b)

Figure 4.16: The current filament model obtained for the 3/1 mode when it is external to the plasma. (a) The $\chi^2_R(t)$ is small when the $q = 3$ surface is external to the plasma and the MHD amplitude is large. The shaded region indicates the time when the equilibrium reconstruction is done and the surface is inside the plasma, shown in figure 4.12. The fit at $t = 30.4$ ms has a lower value of χ^2_R as shown in the next plot. (b) Model signals are a good match to the measured signals resulting in a $\chi^2_R < 1$.

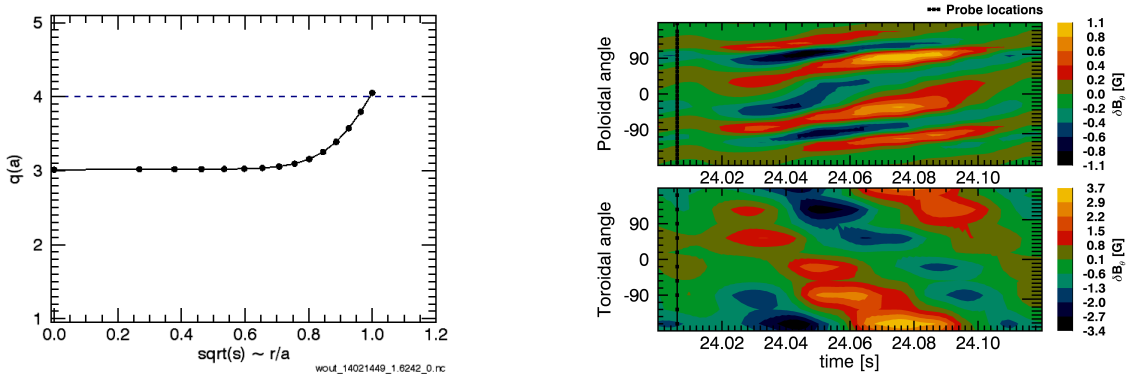

(a) (b)

Figure 4.17: (a) The $q-$profile obtained from equilibrium reconstruction shows that the $q = 4$ surface is just inside the plasma. The x-axis is radial position of flux surface normalized to average minor radius of the plasma. Each point in the plot indicates a flux surface location and the reconstruction is done with 15 surfaces in the plasma. (b) Total fluctuations δB_θ measured by the poloidal and toroidal arrays of B-dot probes indicate that a rotating $m = 4/n = 1$ mode is present. The equilibrium reconstruction is done at $t = 24.06$ ms, in the middle of the shown data window.

because the high initial plasma current ramp quickly moves the rational surface out of the plasma. However, it follows the general behavior of 3/1 mode in that the mode amplitude is larger when it is external to the LCFS. For this mode, it will be demonstrated that the sinusoidal current distribution given by equation 4.10, with $m = 4$, satisfactorily reproduces the observed fluctuations in the poloidal field.

The $q-$profile when the surface is internal to the plasma is shown in figure 4.17a. Again, the equilibrium reconstruction is performed assuming a fixed current profile and using only the external magnetic diagnostics. The $m = 4/n = 1$ mode is observed by the B-dot probes at the reconstruction time and is shown in figure 4.17b.

The mutual inductances between the filaments and the poloidal and toroidal arrays of B-dot probes are shown in figure 4.18. Model signals are obtained following the procedure outlined earlier in 4.3. A comparison between the model signals and measurements when the 4/1 surface is inside the LCFS is shown in figure 4.19a. The fit is quite acceptable with $\chi^2_R \sim 2$. When the surface is external to plasma, the mode amplitude is larger and the computed model signals are shown in 4.19b. The model signals are a better match to

measurement when the mode amplitude is large even though the surface is external, as was observed for the 3/1 mode.

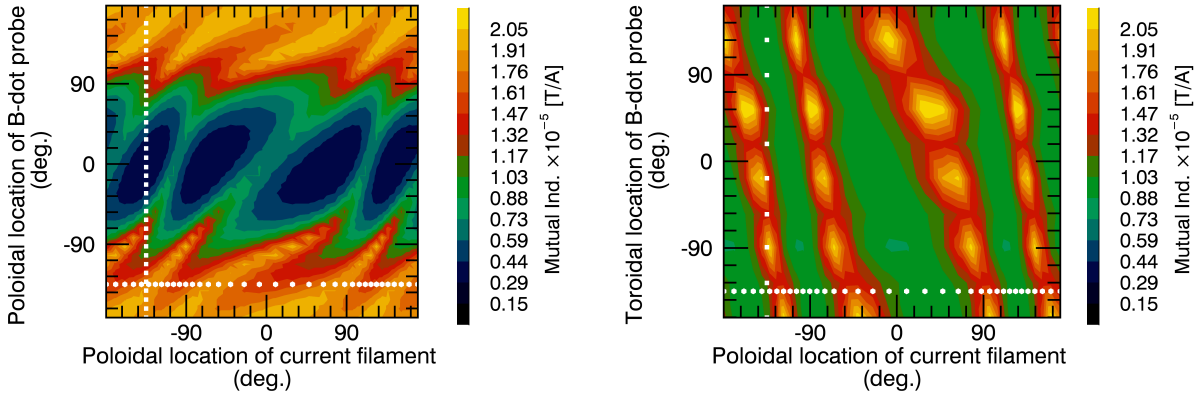

(a) (b)

Figure 4.18: Mutual inductances between the current filaments on the $q = 4$ surface and the B-dot probes in (a) the poloidal array, (b) toroidal array. The poloidal ($m = 4$) and toroidal structure ($n = 1$) is embedded in the mutual inductances.

4.5.3 The 2/1 mode

Analysis of the 2/1 mode is done along the lines of previous examples. We shall obtain the current filament model for the 2/1 mode for the discharge shown in figure 4.11 and for another case where the 2/1 mode amplitude is considerably larger.

Like the 4/1 and 3/1 modes the amplitude of the 2/1 mode is larger when the rational surface, $q = 2$ surface, is external to the plasma. The Fourier analysis of the poloidal mode structure is shown in figure 4.20a, where the spectrum is dominated by $m = 2$ and $m = 1$ modes. The dashed vertical line indicates the time at which the $q = 2$ surface goes external to the LCFS. The current filament model when the 2/1 mode is internal to plasma results in poor fits. We shall look at the fits when the mode is external, shown with highlighted region in the figure. The equilibrium reconstruction is performed when the surface is inside the LCFS.

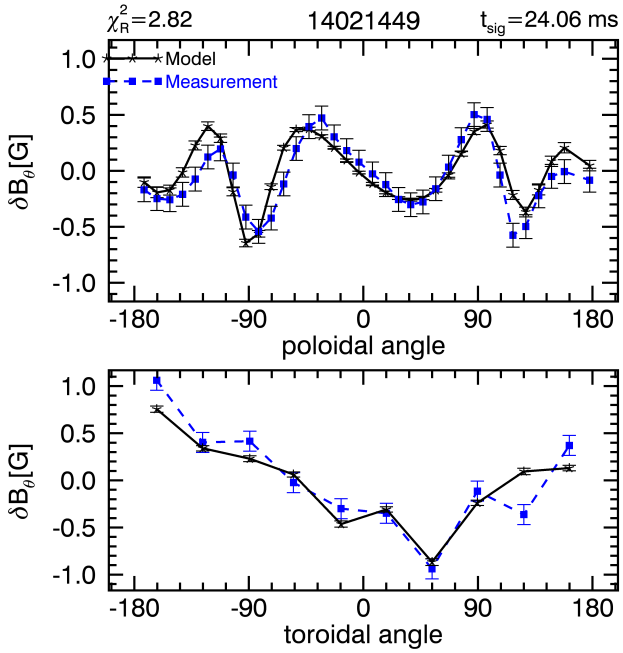

(a)

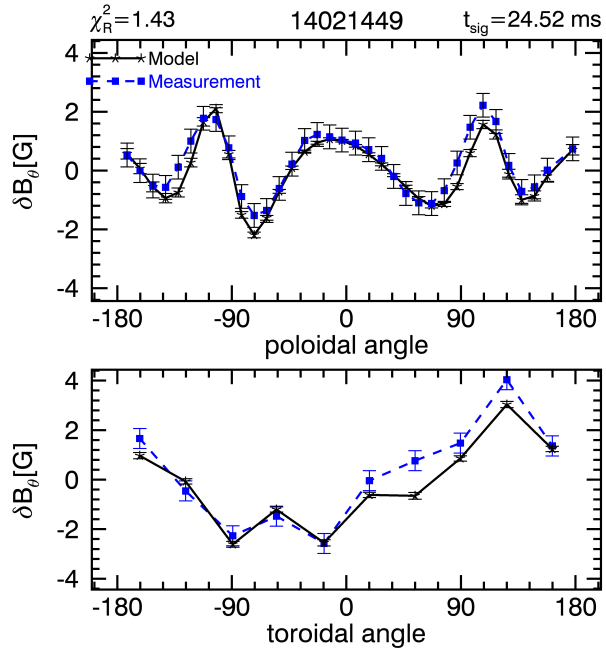

(b)

Figure 4.19: A comparison between the model signals and the measurements is shown when the $q = 4$ surface is (a) internal to the LCFS, and (b) external to the LCFS. Note the magnitude of the mode is about four times larger when it is external. In both cases the fits are acceptable but better when the mode is external and the signals are larger in amplitude. Note that y-axis is different in (a) and (b) due to differences in mode amplitude.

The model signals and the measurements are compared in figure 4.20b. The fits are poor in this case. In general the toroidal structure is well matched except for one measurement at the toroidal angle of $\phi = -18°$. The poloidal structure matches well on the bottom inboard side of the plasma but does not match otherwise. Numerous examples of the 2/1 mode in the current rise have been analyzed and large discrepancies between the model and the measurement exist for them all.

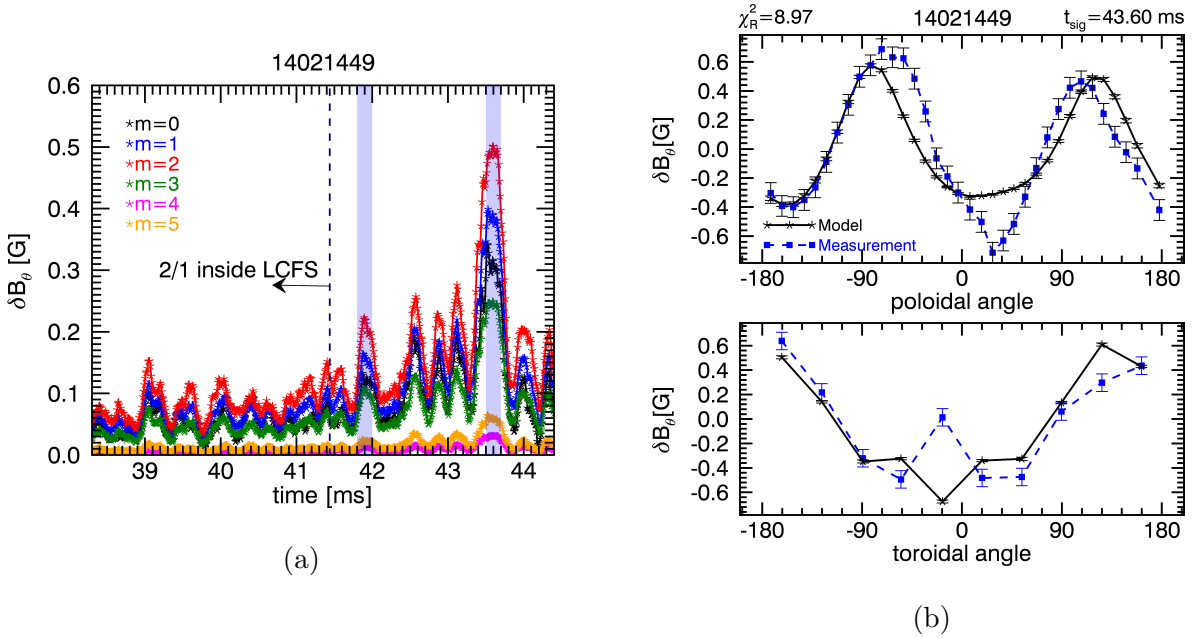

(a) (b)

Figure 4.20: (a) Fourier analysis of the dominant MHD modes show that the $m = 2$ and $m = 1$ harmonics correspond to the 2/1 mode. The $q = 2$ surface exits the plasma at the time indicated by dashed line. The mode amplitude is larger when rational surface it is external to LCFS. The current filament model is obtained at $t = 43.6$ ms indicated with blue shaded region.(b) The current filament model is obtained when mode is external to the plasma shows a poor fit between the model and the measured signals.

Next, we look at another example of the 2/1 mode with significantly larger amplitude. Contour plots of the dominant MHD activity is shown in figure 4.21a. The model signals obtained using the current filament model are shown in figure 4.21b. Even though a very clear 2/1 mode dominates the MHD activity, the observed fits are poor. The χ^2_R is unacceptable in this case as well.

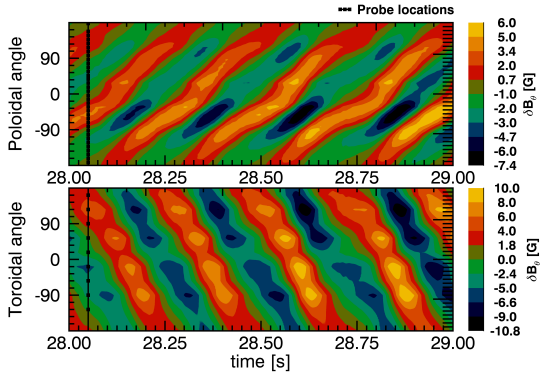

(a)

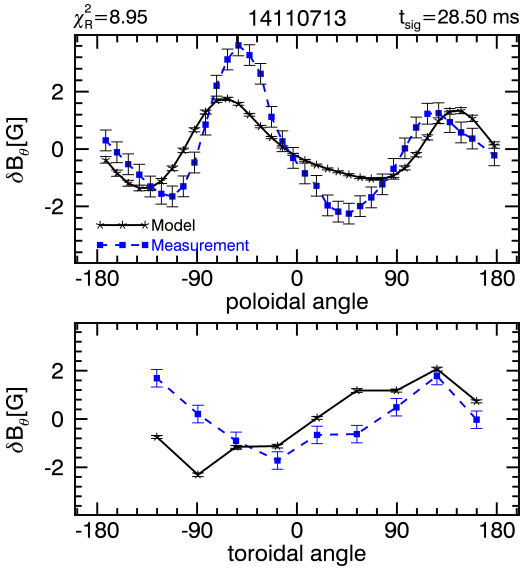

(b)

Figure 4.21: (a) Contour plots showing a large $m/n = 2/1$ mode in the plasma current rise. (b) Current filament model when the 2/1 surface is internal shows poor fit even when a larger mode amplitude is observed.

Analysis of the 2/1 mode has been done for times during the plasma current ramp down phase of CTH discharges. Here also it is found that the model is inconsistent with the measurement giving large χ^2_R.

References

[1] G. Bateman. *MHD Instabilities*. The MIT Press, 1978.

[2] M. D. Kruskal and C. R. Oberman. On the stability of plasma in static equilibrium. *Physics of Fluids*, 1(4):275–280, 1958.

[3] J. Freidberg. *Ideal MHD*. Cambridge University Press, 2014.

[4] V.G. Merezhkin. Structure of the magnetic-field perturbations in the disruptive instability in the T -6 tokamak. *Soviet Journal of Plasma Physics*, 4:152, 1978.

[5] H. Zohm. *Magnetohydrodynamic Stability of Tokamaks*. Wiley, 2015.

[6] O. Klüber, H. Zohm, H. Bruhns, J. Gernhardt, A. Kallenbach, and H.P. Zehrfeld. MHD mode structure and propagation in the ASDEX tokamak. *Nuclear Fusion*, 31(5):907, 1991.

[7] T.R. Harley, D.A. Buchenauer, J.W. Coonrod, and K.M. McGuire. TFTR Mirnov coil analysis with toroidal effects at plasma startup. *Nuclear Fusion*, 29(5):771, 1989.

[8] Allen H. Boozer. Physics of magnetically confined plasmas. *Rev. Mod. Phys.*, 76:1071–1141, Jan 2005.

[9] G. Fussmann, B. J. Green, and H. P. Zehrfeld. The magnetic field of toroidal helical surface currents and its effect on island formation and ergodization in tokamaks. In *Plasma Physics and Controlled Nuclear Fusion Research, (Proc. 8th Int. Conf. Brussels, 1980)*, volume 1, page 353, Vienna, 1981. IAEA.

[10] M. Kikuchi. A note on the mirnov signal analysis in tokamaks. *Nuclear Fusion*, 26(1):101, 1986.

[11] M. Schittenhelm and H. Zohm. Analysis of coupled MHD modes with Mirnov probes in ASDEX Upgrade. *Nuclear Fusion*, 37(9):1255, 1997.

[12] S. Tsuji and H. Toyama. Digital data-acquisition system and mode analysis of magnetohydrodynamic instabilities in a noncircular tokamak. *Review of Scientific Instruments*, 53(12):1882–1887, 1982.

[13] H. Tojo, A. Ejiri, M. P. Gryaznevich, Y. Takase, and Y. Adachi. Poloidal mode analysis of magnetic probe data in a spherical tokamak configuration. *Review of Scientific Instruments*, 79(10), 2008.

[14] L.L. Lao, J.R. Ferron, R.J. Groebner, W. Howl, H. St. John, E.J. Strait, and T.S. Taylor. Equilibrium analysis of current profiles in tokamaks. *Nuclear Fusion*, 30(6):1035, 1990.

[15] J D Hanson, S. P. Hirshman, S F Knowlton, L.L. Lao, E.A. Lazarus, and J. M. Shields. V3FIT: a code for three-dimensional equilibrium reconstruction. *Nuclear Fusion*, 49(7):075031, 2009.

[16] William H. Press, Saul A. Tukolsky, William T. Vetterling, and Brian P. Flannery. *Numerical Recipes in C: The Art of Scientific Computing*. Cambridge University Press, 2nd edition, 1992.

[17] C. B. Markwardt. Non-linear least-squares fitting in IDL with MPFIT. In *Astronomical Data Analysis Software and Systems XVIII ASP Conference Series*, volume 411, pages 251–254, 9 2009.

[18] X. Ma, D. A. Maurer, S. F. Knowlton, M. C. ArchMiller, M. R. Cianciosa, D. A. Ennis, J. D. Hanson, G. J. Hartwell, J. D. Hebert, J. L. Herfindal, M. D. Pandya, N. A. Roberds, and P. J. Traverso. Non-axisymmetric equilibrium reconstruction of a current-carrying stellarator using external magnetic and soft x-ray inversion radius measurements. *Physics of Plasmas*, 22(12), 2015.

[19] S. P. Hirshman and J. C. Whitson. Steepest descent moment method for three dimensional magnetohydrodynamic equilibria. *Physics of Fluids*, 26(12):3553–3568, 1983.

[20] W. D. D'haeseleer, W. N. G. Hitchon, J. D. Callen, and J. L. Shohet. *Flux Coordinates and Magnetic Field Structure: A guide to a Fundamental Tool of Plasma Theory*. Springer-Verlag, 1991.

[21] Steven P. Hirshman, Edward A. Lazarus, James D. Hanson, Stephen F. Knowlton, and Lang L. Lao. Magnetic diagnostic responses for compact stellarators. *Physics of Plasmas*, 11(2):595–603, 2004.

[22] B. A. Stevenson. *3D Reconstruction of Plasma Equilibria using Magnetic Diagnostics on the Compact Toroidal Hybrid*. PhD thesis, Auburn University, 2011.

Chapter 5

Suppression of low edge safety factor disruptions in current-carrying CTH plasmas

5.1 Introduction

A high temperature plasma must be confined long enough for a self-sustaining burn of the fusion fuel,[1] thus a stable magnetohydrodynamic (MHD) equilibrium with high temperature and pressure is important. In tokamaks, ideal MHD instabilities often lead to the catastrophic loss of confined plasma, but may be avoided by limiting the amount of pressure and toroidal current. Though, large toroidal current is desirable to increase energy confinement times[2], the operation of tokamaks with high toroidal current is limited by edge safety factor values greater than 2, $q(a) \propto I_p^{-1} > 2$. Lower values of $q(a)$ often lead to uncontrolled loss of equilibrium.[3] The focus of this chapter is the passive avoidance of such instabilities with the application of external rotational transform in the current-carrying CTH device.

An introduction to the disruptive instability, a survey of observations of low-q disruptions in tokamaks along with efforts to mitigate them, and the role of non-axisymmetric configurations like CTH in the mitigation of these instabilities is presented in section 5.2. Observations of low-q disruptions in CTH and their precursors are presented in sections 5.3 and 5.4 respectively. The observation of suppression of low edge safety factor disruptions with increasing vacuum rotational transforms is presented in section 5.5.[4]

5.2 Background

A disruption is a sudden loss of confined plasma which can lead to large heat, particle and mechanical loads on the confining vessel. Disruptions in tokamaks have long been studied and are known to impose limits on the plasma pressure, density and current.[3,5–9] Such

catastrophic loss of confinement introduces roadblocks in the design and operation of large reactor scale devices like ITER.[10] A disruption leads to a sudden loss of plasma, during the current ramp, flat-top and current fall.[5] The various stages of disruption occuring progressively with time are pre-precursor phase, precursor phase, thermal quench, and current quench. They are outlined as below:

- In the pre-precursor phase some operational limit such as a density limit may be attained, in which case a density increase leads to the onset of an $m = 2$ mode that increases to a large magnitude in the precursor phase.[5]

- Once the MHD instability grows to a critical point a thermal quench is observed, collapsing the central temperature on a very short timescale. A rapid flattening of the current profile is also observed, the evidence of which is a short positive spike in plasma current accompanied by a negative loop voltage spike. Loop voltage is a measure of the change in total flux given by, $V_\ell = -d\Phi/dt$. A negative spike in loop voltage implies an increase in total flux in the space between the poloidal flux loop that measures the loop voltage and the ohmic coil. This increase in the magnetic field implies an increase in the total plasma current because $\oint B \cdot d\mathbf{l} = \mu_0 I$. The magnetic energy associated with the plasma current is given by $W = \frac{1}{2}LI^2$, where L is the total inductance associated with the plasma current. The total magnetic energy, which is the sum of the energy stored in the plasma and the energy due to the inductance between the plasma and the the external ohmic coil, is conserved on the short timescale of the negative loop voltage spike. Since the inductance between the plasma current and the ohmic coil is geometric in nature it does not change and so the inductance of the plasma current, ℓ_i must decrease. The internal inductance, ℓ_i is a measure of the current profile, a small value implying a broad current profile whereas a larger value means that the current profile is more peaked.[5]

- Finally, a rapid temperature decrease increases the plasma resistivity, and unless the external power supplies respond to adjust the loop voltage on a short time scale, the plasma current eventually decays to zero in most cases. This is known as the current quench.[5,9] In a major disruption, the plasma current decays rapidly to zero, while in a minor disruption the plasma may heat up again before eventual collapse later in the discharge.[9]

In tokamaks a disruption may occur due to either a violation of an operational limit or due to technical failures in systems associated with machine or plasma control. Operational limits include the β-limit, where β is plasma pressure normalized to magnetic field pressure, the low-$q(a)$ limit, and the density limit.[9] Here $q(a)$ is the magnetohyrdodynamic (MHD) edge safety factor, which for large aspect ratio approximation, $R >> a$, is given by

$$q(a) = \frac{2\pi a^2 B_\phi}{\mu_0 I R}, \tag{5.1}$$

where R is the major radius, a is the plasma minor radius, I is the total toroidal plasma current, B_ϕ is the toroidal magnetic field, and μ_0 is the magnetic permeability in vacuum. The low-q limit on tokamak operation restricts the amount of plasma current achievable with a given toroidal magnetic field.

Low-$q(a)$ disruptions are caused by tearing/kink instabilities which grow to catastrophic levels. As $q(a)$ value reaches $q(a) = 2$, the $m = 2/n = 1$ MHD mode grows to a large amplitude and locks, i.e. stops rotating in the laboratory frame, resulting in a disruption.[3] These high current disruptions are driven by steep gradients in the current density profile near the edge of the plasma.[5] Thus, in high current tokamak discharges, disruption free operation is limited to edge safety factor values approximately greater than or equal to two, $q(a) \gtrsim 2$.[3] In many cases the disruptions are observed even before the edge safety factor value reaches $q(a) = 2$.[11–13]

Historically, various methods have been applied to stabilize MHD modes to achieve $q(a) < 2$, including the use of a close-fitting shell around the plasma,[14] and lowering of the toroidal magnetic field as the plasma current increases.[15] In tokamaks, the application of external fields bearing the same helicity as that of the instability has been found to influence the MHD mode amplitudes.[16,17] Operation with $q(a) < 2$ has been achieved by using feedback techniques in recent experiments on circular cross-section[18] and shaped tokamaks.[19,20] These feedback-assisted techniques employ small amounts of non-axisymmetric fields (3D) on top of the largely axisymmetric fields, B_0, of tokamak plasmas. A relatively small amount of 3D field, $B_{3D}/B_0 \sim 10^{-3}$, is employed to suppress unstable mode activity as the $q(a) = 2$ operational boundary is approached.

In general, stellarators are immune to the disruptive effects of current-driven instabilities due to the absence of externally driven plasma current.[21] However, in stellarators where plasma current is driven, disruptions are possible, and experiments have shown evidence of disruption avoidance and suppression with increasing levels of transform provided by external magnet coils.[22–24] Indeed, previous experiments on CTH have shown suppression with increasing the amount of 3D fields.[25] CTH plasmas are very non-axisymmetric as the deviation of the equilibrium field from the average axisymmetric equilibrium field is appreciable, $B_{3D}/B_0 \sim 0.1$. In current-carrying CTH plasmas, we shall study the effect of these 3D fields on discharges with the edge safety factor less than two, $q(a) \leq 2$.

The amount of 3D shaping of plasmas in the CTH device is adjusted by varying the vacuum rotational transform provided by the external magnet coils. When current is driven in an already established stellarator equilibrium, the total rotational transform is given by $\iota_{\rm tot} = \iota_{\rm vac} + \iota_{\rm p} = 1/q$, with contribution from both the external coils, $\iota_{\rm vac}$, and the plasma curent, $\iota_{\rm p}$. The amount of 3D shaping in these plasmas can also quantified by the fractional transform,

$$f = \frac{\iota_{\rm vac}(a)}{\iota_{\rm tot}(a)}, \tag{5.2}$$

the ratio of vacuum transform at the edge of the plasma to the total transform at the edge.

5.3 A typical low-q disruption in CTH

The evolution of a typical CTH discharge terminating in a low edge safety factor, $q(a) \leq 2$, disruption is shown in the plots of figure 5.1. The vacuum transform for this discharge is $\iota_{\text{vac}} = 0.024$ with a fractional transform at peak current of $f = 0.04$. The evolution of the plasma current and loop voltage are shown in the first two panels. The evolution of the edge safety factor, $q(a)$, is shown in the third panel. Also shown in the figure is output from one of the B-dot probes, and the plasma density which is maintained fairly constant over the quiescent portion of the discharge. The equilibrium is reconstructed using the V3FIT code.[26]

The ohmic phase of the CTH discharge is initiated at about $t = 20\,\text{ms}$ with a strong current ramp, $dI_{\text{p}}/dt \approx 3\,\text{MA/s}$, that gives rise to a broad current profile and a steep edge gradient. Bursts of magnetic activity with $m/n = 4/1$ and $3/1$ are detected as the $q = 4$ and $q = 3$ rational surfaces exit the plasma. This correlation between the observed mode activity and the edge safety factor value is a common occurrence in tokamaks.[3,27,28] These instabilities observed during the current rise phase are believed to be driven by a steep current gradient.[5]

After the initial current rise, a current ramp of $dI_{\text{p}}/dt \approx 1\,\text{MA/s}$ is maintained from $t = 35\,\text{ms}$ to $t = 50\,\text{ms}$, again resulting in an edge current gradient, as the $q = 2$ surface moves into the vacuum region. Note that in tokamak experiments, large current gradients are observed to cause disruptions in the current rise when $q(a) \sim 2$.[3,18] Like this example, similar current ramp rates are maintained for all the discharges presented later in this chapter.

Magnetic fluctuations corresponding to the $2/1$ and $3/2$ modes are observed during the periods indicated by arrows in the figure. Note that the value of edge safety factor at peak plasma current is $q(a) \sim 1.8$, and since the $q-$profile of these current driven tokamak-like plasmas is monotonically increasing, the $q = 3/2$ surface is close to, but always internal to the last closed flux surface. The current reaches a peak value at about $t = 50\,\text{ms}$ and then decreases prior to the sudden loss of confinement at $t = 70\,\text{ms}$. This disruption event is

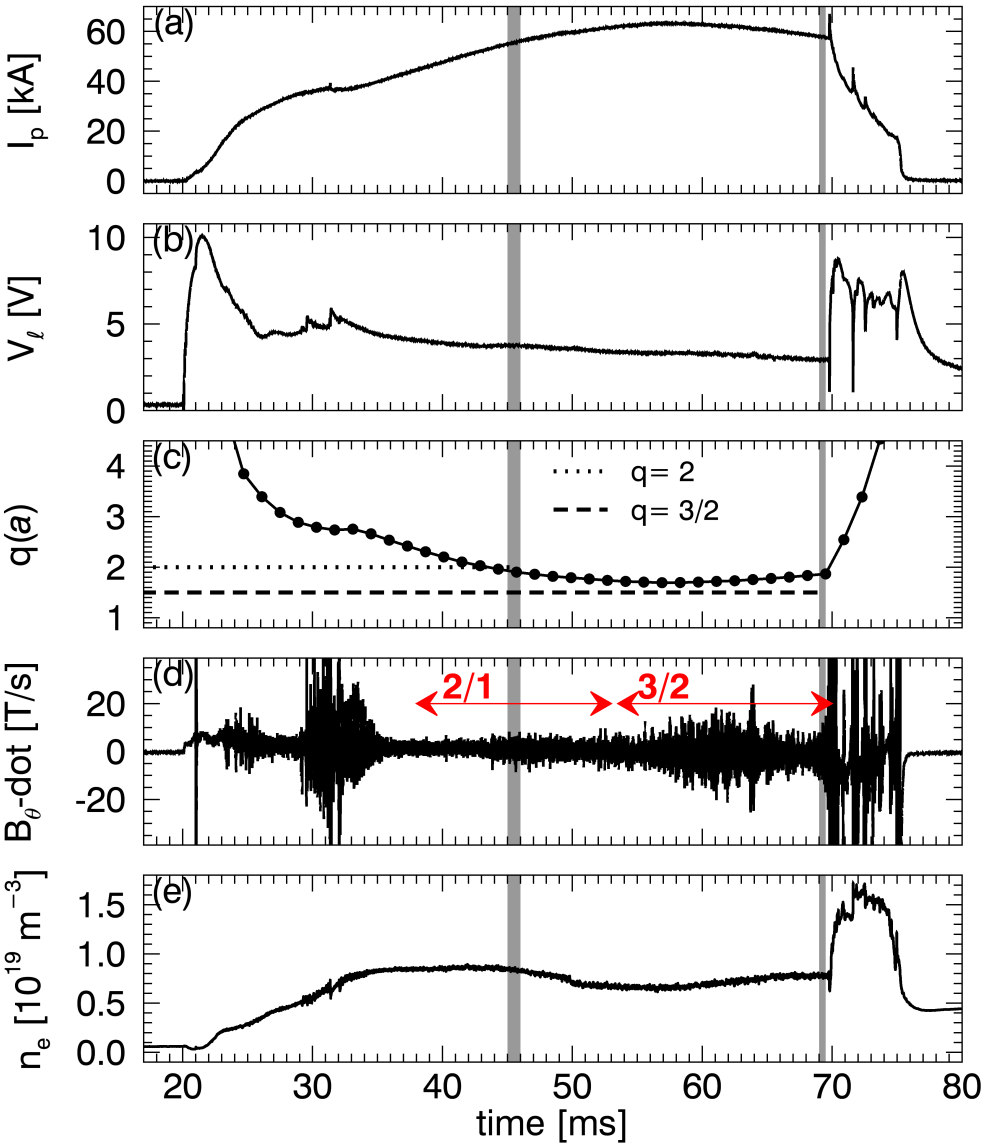

Figure 5.1: Typical evolution of a low-$q(a)$ disruption in CTH indicated by a positive spike in plasma current, negative loop voltage spike, and rapid quench of the plasma current just prior to $t = 70\,\mathrm{ms}$: (a) the plasma current, I_p, (b) loop voltage (c) edge safety factor, $q(a)$, (d) measured magnetic fluctuation level, dB_θ/dt, (e) and the plasma density, n_e.

accompanied by the usual tokamak disruption signatures, a positive spike in plasma current and a negative loop voltage spike.

The vertical position of the plasma in this discharge was centered at the mid-plane by applying a radial magnetic field using the radial field coils (RFC). The rapid decay of plasma current is accompanied by a loss of the vertical positional control, which on the timescale of the disruption, cannot be compensated with the RFC. The sudden increase of the plasma density just after the disruption is thought to be due to plasma contacting the limiters, liberating neutral hydrogen which is then briefly ionized as the plasma current quenches.

5.4 Low-$q(a)$ disruption precursors

The amplitudes of poloidal field fluctuations, $\delta B_\theta(t)$, corresponding to $m/n = 2/1$ and $3/2$ modes determined from biorthogonal decomposition[29], are shown in figure 5.2. The time windows for these signals are centered at $t = 45.5\,\text{ms}$ and $t = 69.25\,\text{ms}$, as indicated by vertical gray bars in figure 5.1. Note that in figure 5.2 there is a difference in scale and that the amplitude of the $2/1$ mode is smaller than that of the $3/2$ mode observed later in the discharge. In general the $2/1$ mode can be bursty, although for this discharge it is fairly coherent. The amplitude of the $2/1$ mode does not get large enough to disrupt the plasma when the $q = 2$ surface moves into the vacuum region. With increasing plasma current, the edge safety factor approaches the value $q(a) = 1.5$ and a large amplitude $m = 3/n = 2$ mode is observed, along with an $m = 4/n = 3$ mode. Both of these modes are implicated by the external magnetic diagnostics as being primary causes of these low-$q(a)$ disruptions. Soft x-ray emission measurements indicate that a non-sawtoothing, periodic $m/n = 1/1$ mode is also present in the core of the plasma.

The secondary $4/3$ mode is inferred from biorthogonal decomposition and its amplitude is shown in figure 5.3. Note that in this figure the time axis spans $0.2\,\text{ms}$ from $t = 69.3\,\text{ms}$ to $t = 69.5\,\text{ms}$ as opposed to $0.5\,\text{ms}$ for the $3/2$ mode shown in figure 5.2. Figures 5.2 and 5.3 show simultaneous observation of $3/2$ and the $4/3$ modes in the plasma prior to the

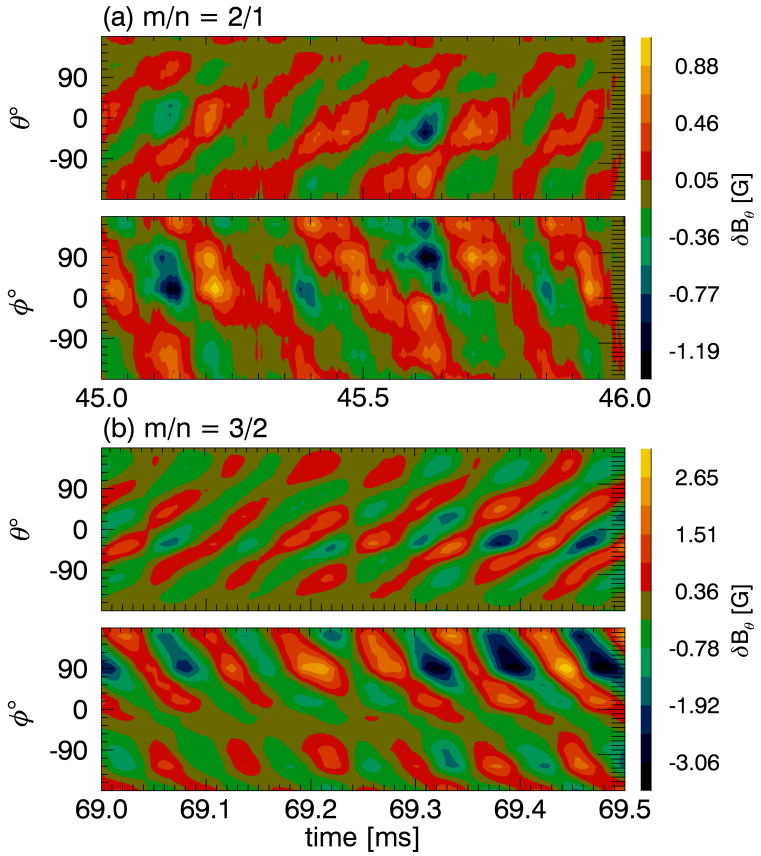

Figure 5.2: Poloidal magnetic field fluctuation amplitudes, $\delta B_\theta(t)$, as measured by a poloidal and toroidal array of pick-up coils, showing (a) the evolution of the $m/n = 2/1$ component of the field, and at a later time, (b) the evolution of the $m/n = 3/2$ mode amplitude. The time windows shown for the $m/n = 2/1$ and $m/n = 3/2$ activity are indicated by the gray highlights in Fig. 5.1.

disruption, with amplitudes of 3 G and about 1 G, respectively. One thing to keep in mind when comparing these amplitudes is the relative location of these surfaces inside the plasma. Since $q(a) \sim 1.8$ at the time of disruption, the $q = 4/3$ surface is necessarily farther inside the plasma, with a smaller minor radius than the 3/2 surface. This means 4/3 surface is farther away from the B-dot probes so its actual amplitude maybe significantly larger. The rotation frequencies for the 3/2 and the 4/3 modes are determined using a fast Fourier transform (FFT) to be $f_{3/2} \sim 12\,\text{kHz}$ and $f_{4/3} \sim 18\,\text{kHz}$ respectively.

Next, evidence of a periodic $m = 1$ mode coexisting in the plasma with the 3/2 and 4/3 modes will be presented. The 1/1 mode, which is expected to be at a smaller minor

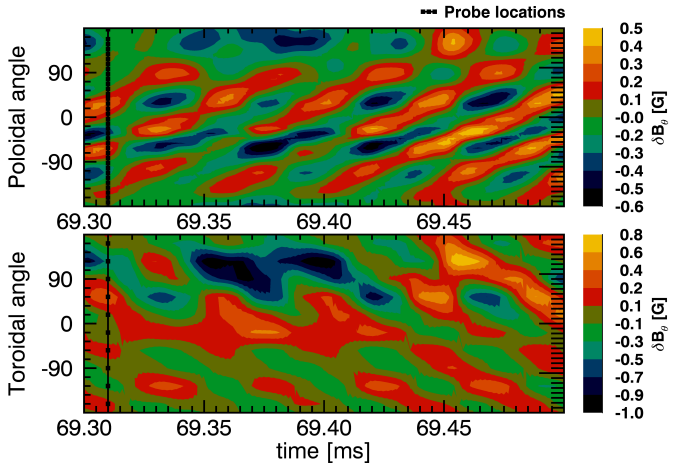

Figure 5.3: Contour plots show the $m = 4/n = 3$ that is observed prior to the low-$q(a)$ disruptions. The 4/3 mode is observed concurrently with 3/2 mode during this time window and is of comparatively smaller amplitude.

radius near the core of the plasma, is too far away from the magnetic diagnostics to be detected. However, CTH is equipped with multiple arrays of detectors that measure chord integrated soft X-ray (SXR) emission.[30] All the SXR cameras are located at one toroidal angle, $\phi = 252°$, therefore only the poloidal mode number can be detected with it. The toroidal mode number is assumed to be $n = 1$, with the presumption that the central edge safety factor is close to one.

The figure 5.4a shows the lines of sights for one of the three, 20-channel SXR cameras, with channel 1 viewing the inboard side of the plasma, and channel 20 viewing the outboard part of the plasma column. The chords are shown overlaid on flux surfaces from an equilibrium reconstructed at about $t = 69\,\text{ms}$. Measured SXR signals from $t = 68.5\,\text{ms}$ to $t = 69.5\,\text{ms}$ are shown in figure 5.4b. The top panel shows the raw measured signals in arbitrary units, indicating a fluctuating emission from the center of the plasma, around channel 11. The amplitude of the SXR signal is small outside of channels 5 on the inboard side, and 17 on the outboard side indicating a strong emission from the core as compared to the edge. The second panel below this is the box-car average of the total raw signal (top panel), and the difference between the two highlights the fluctuations in the SXR emission

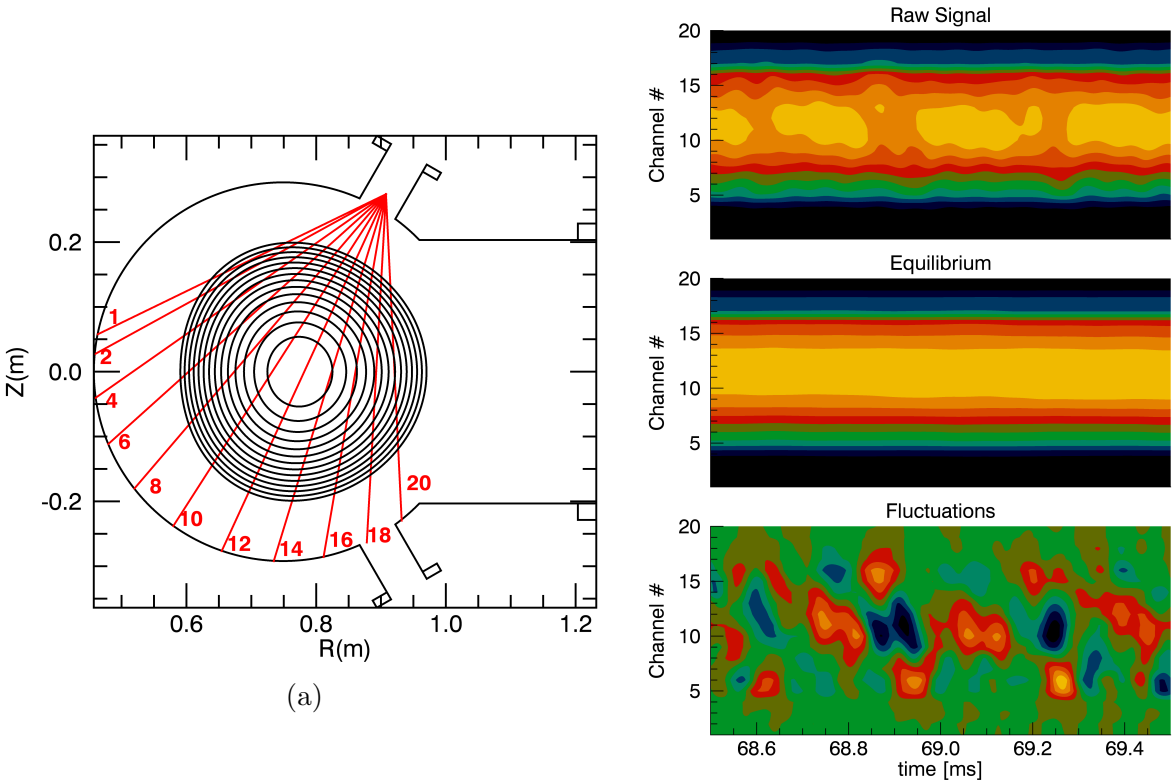

(a)

(b)

Figure 5.4: CTH is equipped with cameras to measure soft X-ray emission. Lines of sights for one of the cameras and the measured signals are shown in this figure. (a) The lines of sights for the different channels of the SXR camera are overlaid on the reconstructed equilibrium. The core of the plasma is viewed by the chords 10 to 14. (b) The top panel shows the raw signals with large emission from the core of the plasma. The box-car averaging of raw signals shown in the second panel indicates a peaked profile from chords 10 to 14 which is consistent with reconstructed location of the core from the figure on the left. The difference between the total raw signals and the box-car averaged signals shows an $m = 1$ like fluctuation near the center of the plasma.

as is shown in the bottom panel. These fluctuations show an $m = 1$ like poloidal structure rotating in the core at a frequency of about $f = 3 - 4\,\mathrm{kHz}$.

The SXR cameras measure bremsstrahlung emission whose amplitude is proportional to square of the plasma density.[31] The density in these low-$q(a)$ discharges was maintained relatively low and constant throughout discharge to stay away from the high density disruption regime observed on CTH. Thus the measured signals are generally small with a small signal to noise ratio. Even so, the observation of an $m = 1$ mode in the center of the plasma is indicative of the presence of a $q = 1$ surface in the plasma core.

Strong current perturbations on the $q = 1$, $4/3$ and $3/2$ surfaces may be implicated in the disruption process, as multiple rational surfaces are known play a role in inducing stochasticity within a plasma, eventually precipitating a disruption.[5]

5.5 The suppression of low-$q(a)$ disruptions with increasing vacuum rotational transform

Next we look at the effect that the amount of vacuum transform has on the characteristics of the low-$q(a)$ disruptions. This is achieved on CTH by varying the ratio of currents in the helical field coil (HF) and the toroidal field coil (TF). The evolution of plasma current and the edge safety factor for discharges with vacuum rotational transform values of $\iota_{\mathrm{vac}}(a) = 0.02$, 0.03 and 0.05 are shown in figure 5.5 from top to bottom respectively. The plasma current evolution was chosen to be nearly identical. The small variation in the edge safety factor is attributed primarily to the differences in their vacuum transforms. The plasma density of these discharges have similar values. The amount of vacuum transform can be thought of as the amount of passive 3D shaping in the equilibrium.

For the discharge with the lowest edge vacuum transform, a fast current quench is observed. A partial or complete collapse is observed when the vacuum transform is increased further to 0.03 whereas no disruption occurs when $\iota_{\mathrm{vac}}(a)$ is raised to 0.05. The magnetic fluctuations also exhibit variability for these discharges; examples for the $\iota_{\mathrm{vac}}(a) = 0.05$, and

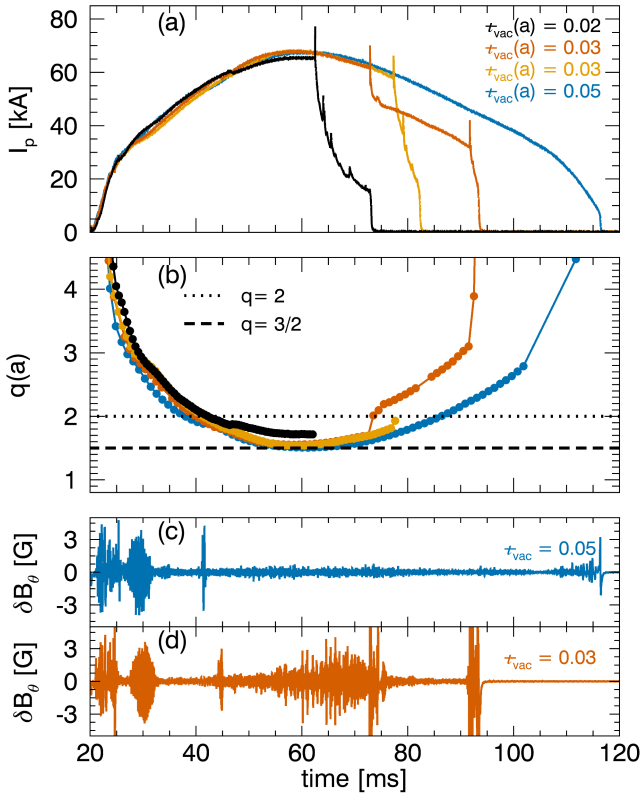

Figure 5.5: A series of discharges with similar plasma current time histories and differing vacuum transform values illustrating the changing character of the observed disruptivity. (a) The evolution of the total plasma current, and (b) the edge safety factor for these discharges. The measured total magnetic fluctuation amplitude for the $\iota_{\rm vac}(a) = 0.05$ case is shown in (c) and for the $\iota_{\rm vac}(a) = 0.03$ in (d).

$\iota_{\rm vac}(a) = 0.03$ cases are shown in figures 5.5c and 5.5d. The amplitude of MHD activity is smaller for the discharge with vacuum transform $\iota_{\rm vac}(a) = 0.05$ from $t = 60\,$ms onwards, unlike for the discharge with $\iota_{\rm vac}(a) = 0.03$ where strong MHD activity eventually disrupts the plasma.

All disruptions suffer from loss of vertical positional control during the current quench and terminate in what is referred to as vertical displacement event (VDE).[5] The vertical position is deduced from measurements of the poloidal field due to the toroidal plasma current, made by coils symmetrically located at the top and bottom of the vacuum vessel.[25] Figure 5.6 shows the vertical position of plasma for the discharges shown in figure 5.5. The plasmas are vertically centered until right before the current quench begins. The plasmas move

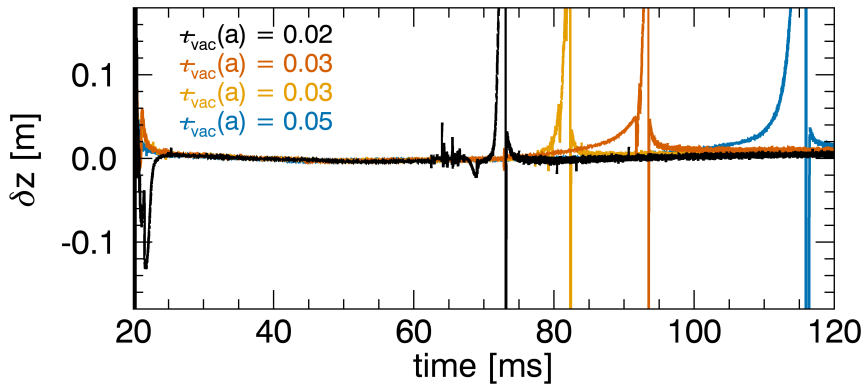

Figure 5.6: Vertical position of the plasma for the set of discharges with different vacuum transforms shown in figure 5.5. The plasmas are vertically centered until right before the current quench begins. For the non-disrupting case, position control is eventually lost because the current in RFC is unable to hold the plasma at low plasma currents.

rapidly up at about $t = 70\,\mathrm{ms}$, and $t = 80\,\mathrm{ms}$, for the fast current quench cases. For the partial current quench, the plasma moves up slowly after the initial current quench begins at about $t = 85\,\mathrm{ms}$, but then moves up at a faster rate at $t = 90\,\mathrm{ms}$ when the current quench is fast. For the non-disrupting case, vertical position control is eventually lost at low plasma current value as the plasma becomes vertically unstable.

The effect of external transform on low-$q(a)$ disruptions in CTH has been studied for an ensemble of 526 discharges. The vacuum transform at the edge, $\iota_{\mathrm{vac}}(a)$, is varied in the range 0.02-0.1 while keeping the evolution of the plasma current, density, and the average equilibrium magnetic field comparable across the discharges in the dataset. The density is held between $n_e = 4 \times 10^{18}\,\mathrm{m}^{-3}$ and $n_e = 8 \times 10^{18}\,\mathrm{m}^{-3}$, whereas the average magnetic field magnitude is between $\mid B \mid = 0.45\,\mathrm{T}$ and $\mid B \mid = 0.55\,\mathrm{T}$. A plot of $q(a)$ versus the edge vacuum rotational transform $\iota_{\mathrm{vac}}(a)$ is shown in figure 5.7. The value of the edge safety factor is taken at peak plasma current. The disruptivity of these low-$q(a)$ plasmas is observed to have three regimes, depending upon the value of the vacuum transform.

Plasmas in the regime $\iota_{\mathrm{vac}}(a) \lesssim 0.03$ terminate with a fast current quench. The second regime, $0.03 \lesssim \iota_{\mathrm{vac}}(a) \lesssim 0.07$, consists of discharges terminating in fast and partial current quenches, as well as the discharges for which disruption has been suppressed. In the third

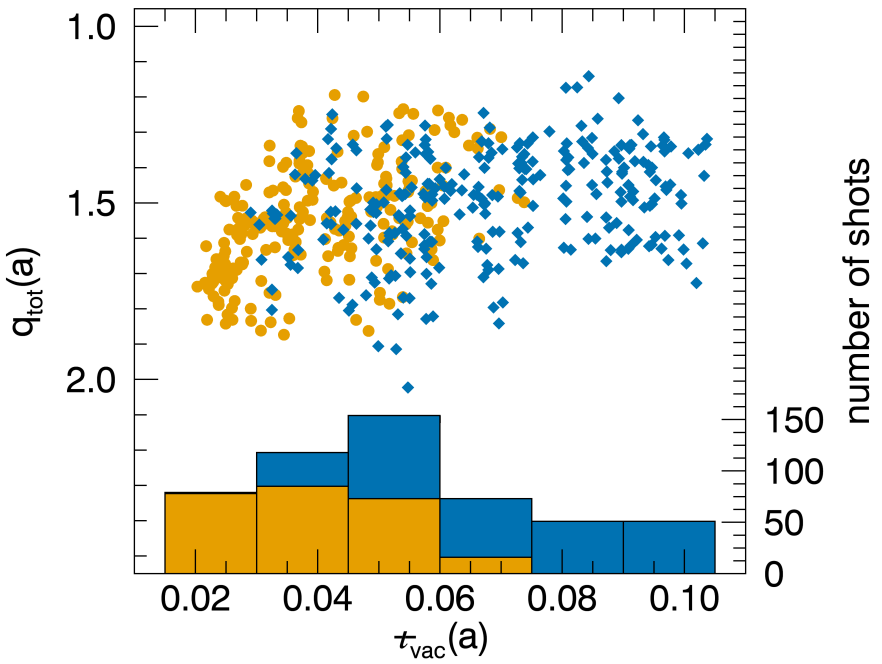

Figure 5.7: An ensemble of low-$q(a)$ discharges showing the value of $q(a)$ at peak plasma current as a function of the applied vacuum transform. Disrupting shots are represented by gold circles and non-disrupting shots are indicated by blue diamonds. Also shown is a histogram of the data using a vacuum transform bin-size of 0.01. The corresponding y-axis on the right represents the number of shots within a bin. Only disruptions are observed to occur at the lowest values of edge vacuum transform $\iota_{\rm vac}(a) \sim 0.02$ to 0.03. The observed disruptivity is seen to reduce with increased edge vacuum transform in the range of $0.03 \lesssim \iota_{\rm vac}(a) \lesssim 0.07$. Disruptions are completely suppressed when $\iota_{\rm vac}(a) \gtrsim 0.07$.

regime, where the external helical transform is increased to $\iota_{\rm vac}(a) \gtrsim 0.07$, disruption free operation is achieved with $q(a) < 2$. This data set can also be viewed in terms of the fractional transform, f, defined in equation 5.2. The plot of $q(a)$ versus f shown in figure 5.8 indicates that for complete disruption suppression a fractional transform of $f \approx 0.1$, or about 10% of the total transform at the edge of plasma is sufficient.

As mentioned earlier, in tokamaks disruptive behavior is observed during the current rise if the ramp rate is sufficiently large, and the onset of low-q disruptions can be delayed by tailoring the plasma current ramp rate.[3,18] However, they still do occur when the edge safety factor is greater than 2. The current ramp rate in this data set when $q(a) \sim 2$ is maintained at roughly 1.5 MA/s. The fluctuating component of the poloidal field, δB_θ, can

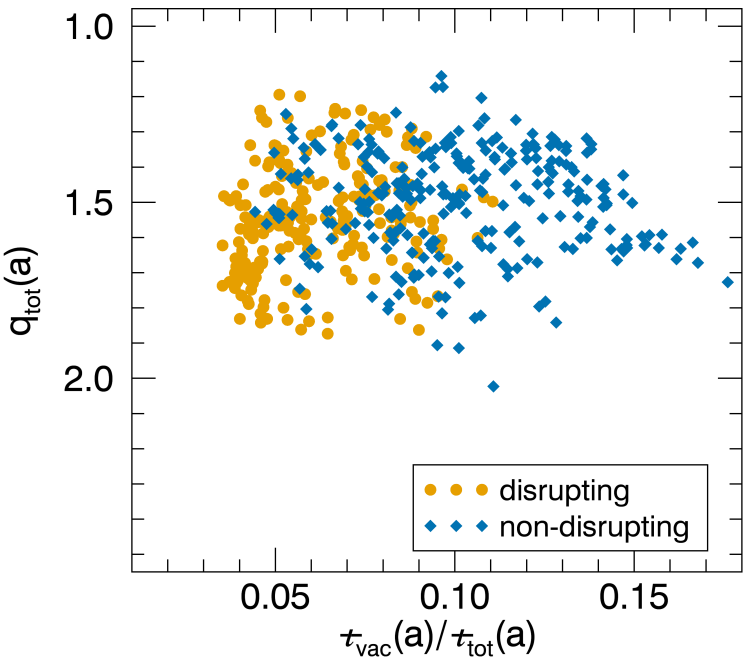

Figure 5.8: The same data set shown in figure 5.7 plotted in terms of the fractional transform, showing disruption suppression for $f > 0.1$.

be bursty for some shots when $q(a) \sim 2$; however, the amplitude is not large enough to disrupt the plasmas. The 3/1 mode which is also observed during the current rise, has comparatively larger amplitude and occurs much earlier in the plasma current evolution but does not appear to have an effect on the magnitude of the 2/1 mode. A survey of the total fluctuation amplitude, δB_θ, when $q(a) \sim 2$ and $q(a) \sim 3$, is shown in figure 5.9a for a subset of the discharges in the data set over the complete range of vacuum transform in the dataset. It shows that when $q(a) \sim 3$, the amplitude of fluctuations is in the range, $\delta B_\theta = 0.5\,\mathrm{G}$ to $\delta B_\theta = 1.0\,\mathrm{G}$, whereas the fluctuation amplitude has a larger scatter when $q(a) \sim 2$, but for the majority of the shots its value is smaller, $\delta B_\theta < 0.5\,\mathrm{G}$. The values larger than 1.0 G usually correspond to large amplitude transient bursts. Figure 5.9b shows that the magnitude of δB_θ is proportional to the plasma current ramp rate when $q(a) \sim 3$, whereas in the majority of discharges when $q(a) = 2$, the ramp rates are consistently about $1.5\,\mathrm{MA/s}$.

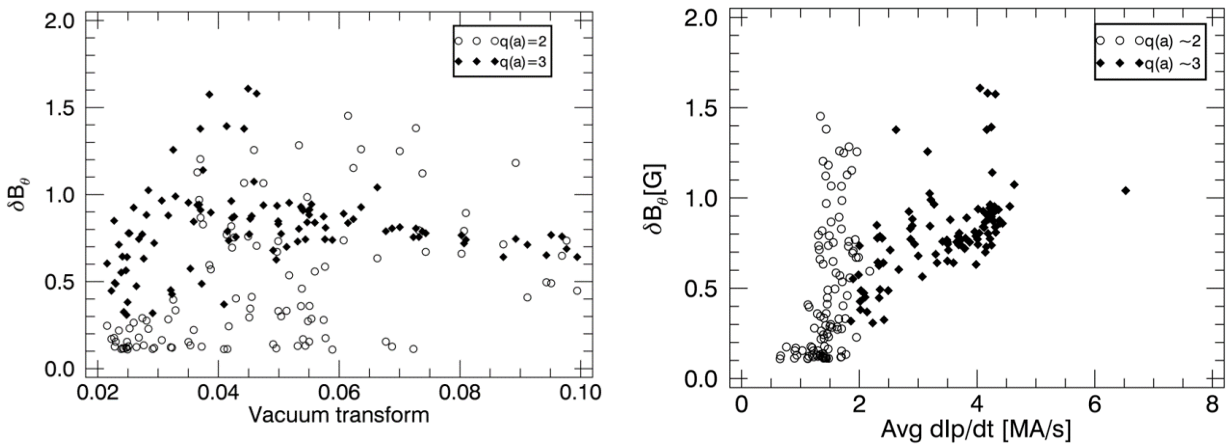

(a) (b)

Figure 5.9: Magnitude of fluctuations in poloidal field when $q(a) \sim 2$ and $q(a) \sim 3$ is compared for dependence on (a) vacuum transform (b) plasma current ramp rates.

To access different values of the edge safety factor, which is inversely proportional to the plasma current, the plasma current was varied by applying different amounts of ohmic input power. Figure 5.10 shows that the peak plasma current, $I_{\rm p}$, varies from 40 kA to 80 kA. The disrupting discharges are marked by solid circles whereas the open circles indicate non-disrupting discharges. This shows that for a fixed vacuum transform, say $\iota_{\rm vac}(a) = 0.05$, disruptions are observed for multiple values of I_p and by extension, for a range of $q(a)$ values.

A survey of $q(a)$ just prior to disruption is plotted in figure 5.11. This shows that the edge safety factor values fall within a narrow range of, $1.6 \lesssim q(a) \lesssim 1.9$, indicating that the $q = 1.5$ surface is internal to the plasma and the $q = 2$ surface is outside, though close to the plasma edge. The magnetic activity prior to the disruptions does not indicate the presence of a 2/1 mode and so it is not implicated in the disruption.

From the scatter plot shown in figure 5.7 it is observed that for discharges with vacuum transforms in the range, $0.04 \lesssim \iota_{\rm vac}(a) \lesssim 0.06$, about half of the discharges terminate in a disruption. These discharges may terminate either with a fast or a partial current quench. Three of these discharges with vacuum transform of $\iota_{\rm vac}(a) = 0.05$ are shown in the figure 5.12. One ends with a fast current quench, second with a partial current quench, while the

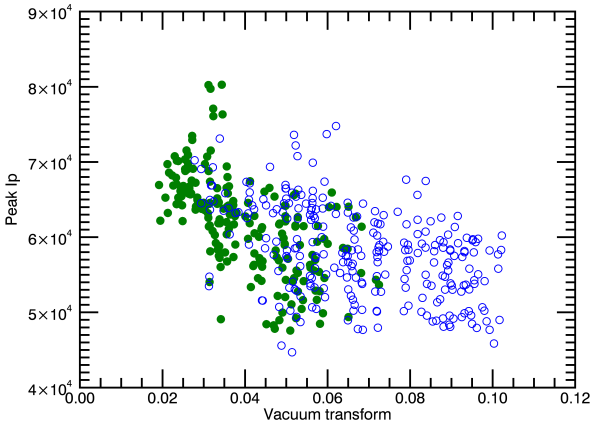

Figure 5.10: The dataset consists of discharges with varying amounts of driven plasma current, between 40 kA and 80 kA. The disruptions are indicated by solid circles whereas open circles indicate non-disrupting discharges.

third does not disrupt. The plasma current and the edge safety factor evolutions shown in the top two panels are identical up to the time of disruption, and the MHD fluctuations are of comparable amplitude. For all three discharges, MHD activity corresponding to the $m = 3/n = 2$ and $4/3$ modes are measured with B-dot probes; corresponding mode amplitudes for the time period indicated by the shaded region are shown in figure 5.13. Biorthogonal decomposition is applied to the total fluctuations and the dominant modes, $3/2$ and $4/3$, are isolated from the total fluctuations. The amplitudes of these modes are comparable for the three shots from $t = 62$ ms to $t \approx 68$ ms. The average $3/2$ mode amplitude during this time is about $1 - 1.2$ G while the average amplitude of the $4/3$ mode is about $0.2 - 0.3$ G. The mode amplitudes from $t = 70$ ms to about $t = 74$ ms decrease for all shots. The difference in mode activity between the three shots is seen from about $t = 74$ ms. For the discharge with a fast current quench, both $3/2$ and $4/3$ mode amplitudes rapidly increase to about 1.5 G and 0.5 G respectively. For the partial current quench, the $3/2$ mode growth is not as rapid but does have a similar amplitude, whereas the $4/3$ mode grows to only about 0.2 G. For the non-disrupting case, the $3/2$ mode amplitude is comparable though somewhat smaller, and the $4/3$ mode is distinctly small, being barely above the noise floor of the detectors.

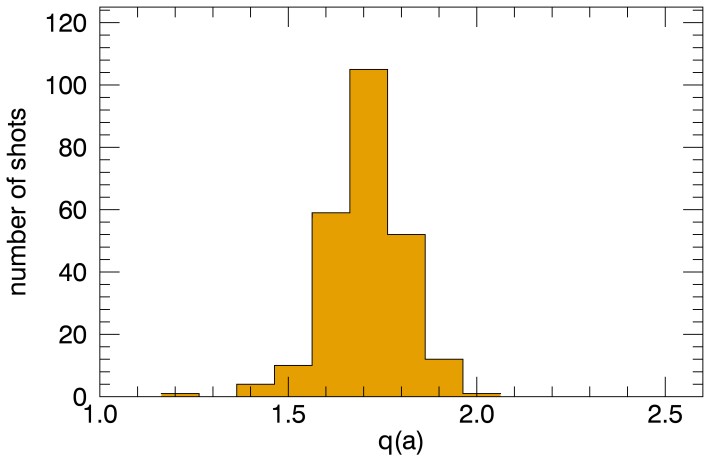

Figure 5.11: A survey of $q(a)$ just prior to disruption shows that discharges disrupt with edge safety factor values within a narrow range of, $1.6 \lesssim q(a) \lesssim 1.9$

Thus, it is concluded that both 3/2 and 4/3 modes are implicated in low edge safety factor disruptions.

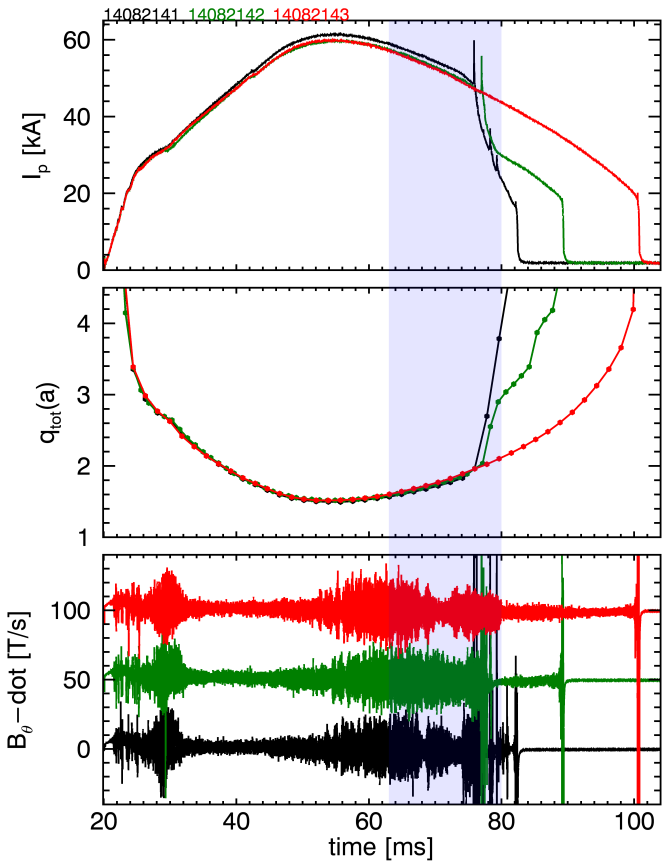

Figure 5.12: The disruptivity of three discharges with identical values of edge rotational transform, $\iota_{\rm vac}(a) = 0.05$, are compared. Shown from top to bottom are the measured plasma current,$I_{\rm p}$; the edge safety factor obtained from equilibrium reconstruction, $q(a)$, and the signals measured by the B-dot probes, dB_θ/dt. Note that B-dot signals are offset by $50\,{\rm T/s}$ for ease of presentation. The evolution of plasma current and the edge safety factor are identical. Two of these discharges disrupt at a different rate of current quench while one does not.

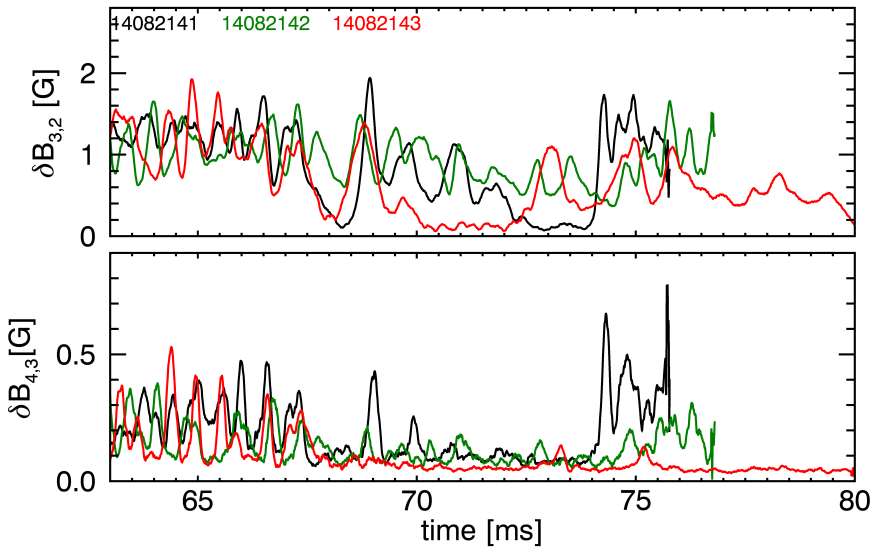

Figure 5.13: The growth of MHD modes with helicities $m/n = 3/2$ and $4/3$ are compared for discharges with identical vacuum transform but different disruption outcomes.

References

[1] J D Lawson. Some criteria for a power producing thermonuclear reactor. *Proceedings of the Physical Society. Section B*, 70(1):6, 1957.

[2] J. Freidberg. *Plasma Physics and Fusion Energy.* Cambridge University Press, 1st edition, 2007.

[3] J.A. Wesson, R.D. Gill, M. Hugon, F.C. Schuller, J.A. Snipes, D.J. Ward, D.V. Bartlett, D.J. Campbell, P.A. Duperrex, A.W. Edwards, R.S. Granetz, N.A.O. Gottardi, T.C. Hender, E. Lazzaro, P.J. Lomas, N. Lopes Cardozo, K.F. Mast, M.F.F. Nave, N.A. Salmon, P. Smeulders, P.R. Thomas, B.J.D. Tubbing, M.F. Turner, and A. Weller. Disruptions in JET. *Nuclear Fusion*, 29(4):641, 1989.

[4] M. D. Pandya, M. C. ArchMiller, M. R. Cianciosa, D. A. Ennis, J. D. Hanson, G. J. Hartwell, J. D. Hebert, J. L. Herfindal, S. F. Knowlton, X. Ma, S. Massidda, D. A. Maurer, N. A. Roberds, and P. J. Traverso. Low edge safety factor operation and passive disruption avoidance in current carrying plasmas by the addition of stellarator rotational transform. *Physics of Plasmas*, 22(11), 2015.

[5] John Wesson. *Tokamaks.* Oxford University Press, 4th edition, 2011.

[6] F C Schüller. Disruptions in tokamaks. *Plasma Physics and Controlled Fusion*, 37(11A):A135, 1995.

[7] F. Alladio, G. Bardotti, R. Bartiromo, G. Bracco, F. Bombarda, G. Buceti, P. Buratti, E. Caiaffa, R. Cesario, F. Crisanti, R. De Angelis, F. De Marco, M. de Pretis, D. Frigione, R. Giannella, M. Grolli, R. Iacono, S. Mancuso, M. Marinucci, G. Mazzitelli, F. Orsitto, V. Pericoli-Ridolfini, L. Pieroni, S. Podda, G.B. Righetti, F. Romanelli, D. Santi, S.E. Segre, A.A. Tuccillo, O. Tudisco, G. Vlad, and V. Zanza. MHD stability limits to the operation parameters of the FT tokamak. *Nuclear Fusion*, 26(1):11, 1986.

[8] S.V. Mirnov and I.B. Semenov. Investigation of the Instabilities of the Plasma String in Tokamak-3 system by means of a correlation method. *Soviet Atomic Energy*, 30:22, 1971.

[9] H. Zohm. *Magnetohydrodynamic Stability of Tokamaks*. Wiley, 2015.

[10] T.C. Hender, J.C Wesley, J. Bialek, A. Bondeson, A.H. Boozer, R.J. Buttery, A. Garofalo, T.P Goodman, R.S. Granetz, Y. Gribov, O. Gruber, M. Gryaznevich, G. Giruzzi, S. Gnter, N. Hayashi, P. Helander, C.C. Hegna, D.F. Howell, D.A. Humphreys, G.T.A. Huysmans, A.W. Hyatt, A. Isayama, S.C. Jardin, Y. Kawano, A. Kellman, C. Kessel, H.R. Koslowski, R.J. La Haye, E. Lazzaro, Y.Q. Liu, V. Lukash, J. Manickam, S. Medvedev, V. Mertens, S.V. Mirnov, Y. Nakamura, G. Navratil, M. Okabayashi, T. Ozeki, R. Paccagnella, G. Pautasso, F. Porcelli, V.D. Pustovitov, V. Riccardo, M. Sato, O. Sauter, M.J. Schaffer, M. Shimada, P. Sonato, E.J. Strait, M. Sugihara, M. Takechi, A.D. Turnbull, E. Westerhof, D.G. Whyte, R. Yoshino, H. Zohm, Disruption the ITPA MHD, and Magnetic Control Topical Group. Chapter 3: MHD stability, operational limits and disruptions. *Nuclear Fusion*, 47(6):S128, 2007.

[11] A.D. Cheetham, S.M. Hamberger, H. Kuwahara, A.H. Morton, and D. Vender. Pre-disruption MHD activity in the LT-4 tokamak. *Nuclear Fusion*, 27(5):843, 1987.

[12] S.M. Kaye, G.L. Jahns, A.W. Morris, S. Sesnic, K. Bol, M.S. Chance, P. Couture, R.J. Fonck, G. Gammel, W.W. Heidbrink, R. Kaita, H.W. Kugel, B. LeBlanc, J. Manickam, N. Ohyabu, M. Okabayashi, M.F. Reusch, and H. Takahashi. Characteristics of low-q disruptions in PBX. *Nuclear Fusion*, 28(11):1963, 1988.

[13] P.C. de Vries, M.F. Johnson, I. Segui, and JET EFDA Contributors. Statistical analysis of disruptions in JET. *Nuclear Fusion*, 49(5):055011, 2009.

[14] DIVA Group. Very-low-q discharges in DIVA. *Nuclear Fusion*, 20(3):271, 1980.

[15] TFR Group. Low-Q MHD activity studies on TFR. *Nuclear Fusion*, 24(6):784, 1984.

[16] Pulsator Team. The pulsator tokamak. *Nuclear Fusion*, 25(9):1059, 1985.

[17] D.E. Roberts, D. Sherwell, J.D. Fletcher, G. Nothnagel, and J.A.M. de Villiers. Major disruptions induced by helical coils on the tokoloshe tokamak. *Nuclear Fusion*, 31(2):319, 1991.

[18] P Zanca, L Marrelli, R Paccagnella, A Soppelsa, M Baruzzo, T Bolzonella, G Marchiori, P Martin, and P Piovesan. Feedback control model of the m = 2, n = 1 resistive wall mode in a circular plasma. *Plasma Physics and Controlled Fusion*, 54(9):094004, 2012.

[19] P. Piovesan, J. M. Hanson, P. Martin, G. A. Navratil, F. Turco, J. Bialek, N. M. Ferraro, R. J. La Haye, M. J. Lanctot, M. Okabayashi, C. Paz-Soldan, E. J. Strait, A. D. Turnbull, P. Zanca, M. Baruzzo, T. Bolzonella, A. W. Hyatt, G. L. Jackson, L. Marrelli, L. Piron, and D. Shiraki. Tokamak operation with safety factor $q_{95} < 2$ via control of mhd stability. *Phys. Rev. Lett.*, 113:045003, Jul 2014.

[20] J. M. Hanson, J. M. Bialek, M. Baruzzo, T. Bolzonella, A. W. Hyatt, G. L. Jackson, J. King, R. J. La Haye, M. J. Lanctot, L. Marrelli, P. Martin, G. A. Navratil, M. Okabayashi, K. E. J. Olofsson, C. Paz-Soldan, P. Piovesan, C. Piron, L. Piron, D. Shiraki, E. J. Strait, D. Terranova, F. Turco, A. D. Turnbull, and P. Zanca. Feedback-assisted extension of the tokamak operating space to low safety factor. *Physics of Plasmas*, 21(7):–, 2014.

[21] Allen H. Boozer. What is a stellarator? *Physics of Plasmas*, 5(5):1647–1655, 1998.

[22] D. W. Atkinson, A. N. Dellis, R. D. Gill, D. J. Lees, W. Millar, B. A. Powell, P. A. Shatford, and D. R. A. Webb. Comparison between tokamak and ohmically heated stellarator plasmas. *Phys. Rev. Lett.*, 37:1616–1619, Dec 1976.

[23] W VII-A Team. Stabilization of the (2, 1) tearing mode and of the current disruption in the W VII-A stellarator. *Nuclear Fusion*, 20(9):1093, 1980.

[24] M. Hirsch, J. Baldzuhn, C. Beidler, R. Brakel, R. Burhenn, A. Dinklage, H. Ehmler, M. Endler, V. Erckmann, Y. Feng, J. Geiger, L. Giannone, G. Grieger, P. Grigull, H-J Hartfuß, D. Hartmann, R. Jaenicke, R. König, H. P. Laqua, H. Maaßberg, K. McCormick, F. Sardei, E. Speth, U. Stroth, F. Wagner, A. Weller, A. Werner, H. Wobig, S. Zoletnik, and for the W7-AS Team. Major results from the stellarator Wendelstein 7-AS. *Plasma Physics and Controlled Fusion*, 50(6):053001, 2008.

[25] M. C. ArchMiller, M. R. Cianciosa, D. A. Ennis, J. D. Hanson, G. J. Hartwell, J. D. Hebert, J. L. Herfindal, S. F. Knowlton, X. Ma, D. A. Maurer, M. D. Pandya, and P. Traverso. Suppression of vertical instability in elongated current-carrying plasmas by applying stellarator rotational transform. *Physics of Plasmas*, 21(5), 2014.

[26] J D Hanson, S. P. Hirshman, S F Knowlton, L.L. Lao, E.A. Lazarus, and J. M. Shields. V3FIT: a code for three-dimensional equilibrium reconstruction. *Nuclear Fusion*, 49(7):075031, 2009.

[27] R.S. Granetz, I.H. Hutchinson, and D.O. Overskei. Disruptive MHD activity during plasma current rise in Alcator A tokamak. *Nuclear Fusion*, 19(12):1587, 1979.

[28] H. Kuwahara, A.D. Cheetham, and A.H. Morton. Observation of m=7/n=3, m=5/n=2 and m=3/n=1 MHD modes during plasma current ramping in the LT-4 tokamak. *Nuclear Fusion*, 26(8):1092, 1986.

[29] T. Dudok de Wit, A.L. Pecquet, J.C. Vallet, and R. Lima. The biorthogonal decomposition as a tool for investigating fluctuations in plasmas. *Physics of Plasmas*, 1(10):3288–3300, 1994.

[30] J. L. Herfindal, J. D. Dawson, D. A. Ennis, G. J. Hartwell, S. D. Loch, and D. A. Maurer. Design and initial operation of a two-color soft x-ray camera system on the compact toroidal hybrid experiment. *Review of Scientific Instruments*, 85(11), 2014.

[31] I. H. Hutchinson. *Principles of Plasma Diagnostics*. Cambridge University Press, 2002.

Chapter 6

Discussion and future work

6.1 Discussion

MHD modes in low-β cylindrical plasmas can be expressed as Fourier harmonics of poloidal and toroidal mode numbers, m and n respectively. This is because a magnetic field line, which always lies on a given flux surface as it makes toroidal transits, has a constant pitch. However, the bending of a cylinder into a torus causes the local magnetic field pitch to depend on the poloidal angle. A single Fourier poloidal mode, m, is then insufficient to express a single MHD mode.[1] In high-β cases the structure of MHD modes is expected to be comprised of multiple poloidal harmonics.[1] CTH plasmas are low-β, low aspect ratio, and do not possess toroidal symmetry. Thus the interpretation of poloidal mode numbers is difficult.

In chapter 4 we developed current filament models for the MHD modes often observed in CTH plasmas, such as $m/n = 3/2$, $4/1$, $3/1$, $2/1$. Our model assumed field aligned perturbed currents on rational surfaces. Knowing the shape of the flux surface from equilibrium reconstruction enabled us to determine the fluctuations in the poloidal magnetic field at the location of B-dot probes due to these helical currents. Only two parameters, the amplitude and the phase of the current distribution were varied such that the modeled, δB_θ, are consistent with the measurements. Since the total fluctuations may have contributions from multiple MHD modes, we have used the biorthogonal decomposition technique to isolate fluctuations corresponding to a single mode. The model worked well for the $3/2$ mode which had its resonant surface inside the LCFS, close to the edge of plasma, implying that the perturbed currents are located at the rational surface parallel to the equilibrium magnetic field lines. Thus, its structure is flute-like, as expected for current driven long wavelength

modes.[2] Since CTH equilibria are low-β, the current driven modes may be expected to have such a structure, which is reflected in the results of the current filament model, that takes into account the 3-D magnetic field equilibrium of CTH. In high-β tokamaks the field aligned perturbed current model does not describe the perturbation well[3].

For the cases of the MHD modes observed in the current rise, the 3/1, and the 4/1 modes, the reduced χ^2 of the fit between the model and the measured signals was large when the resonant surface associated with these modes was inside the LCFS. Then, as resonant surfaces moved outside the LCFS, while being close to the edge of the plasma, the amplitude of observed perturbation increased, and also the dominant Fourier harmonics representing the spatial structure of these modes increased relative to the other harmonics of the spatial structure. The current filament model was obtained for the equilibrium when the rational surface was close to the LCFS, but inside the plasma so that we can still determine the path of the magnetic field lines from the reconstructed equilibrium; however, measured signals were chosen for the time when the surface was external to the LCFS. This resulted in much lower χ^2 values. Here, a current filament model was obtained with the assumption that shape and the position of the equilibrium flux surface does not appreciably change in the short time that it takes as the rational surface move out. This result implies that even when these 3/1, and the 4/1 modes are external to the plasma the perturbation induced by them on the edge of the plasma is well modeled by the perturbed currents along to the equilibrium magnetic field lines on the surface. When the 3/1 and 4/1 magnetic islands are internal to the plasma, they may be large enough so that the simple current filament model is insufficient; while, as the island moves outside the plasma, the perturbation induced by it on the plasma edge could be represented well by our model.

In contrast to the 3/1 and the 4/1 mode, the model for the 2/1 mode observed during the current rise did not agree with the measurements for both cases where it is located inside and outside LCFS. This could be possibly due to the presence of a large 2/1 magnetic island within the equilibrium or due to coupling with its harmonic, the 4/2 mode that is often

detected. While the 2/1 mode is not modeled well by the current filament, the fact the 3/2 mode fit well while being internal to the LCFS may indicate the corresponding magnetic island is small.

Low edge safety factor disruptions constrain the amount of toroidal plasma current in tokamaks as the equilibrium approaches the value $q(a) = 2$. The MHD instability that leads to a plasma current quench has been suppressed in axisymmetric configurations by various methods[4–7], and more recently, by applying small amounts of non-axisymmetric fields to the background axisymmetric field[8–10].

In chapter 5 low-q disruptions have been studied in non-axisymmetric 3D equilibria by varying the amount of externally applied transform, ι_{vac}. Disruption free operation with edge safety factors $q(a) < 2$ is routine on CTH if a sufficient amount of external rotational transform, ι_{vac}, is applied. It has been shown that low-q disruptions are suppressed with the application of an external rotational transform of, $\iota_{\text{vac}}(a) \geq 0.07$, or a fractional transform of $f = 0.1$. When the plasma does disrupt, for $\iota_{\text{vac}}(a) \leq 0.07$, the precursors to the disruption are $m/n = 3/2$ and $4/3$ modes observed from magnetics, and a periodic non-sawtoothing $1/1$ mode inferred from the SXR emission. This indicates the presence of three different resonant surfaces inside the plasma. In cylindrical plasma equilibria it has been shown that perturbations of two resonant modes $q = m_1/n_1$ and $q = m_2/n_2$ may couple with other modes with helicities $q = (m_1 + m_2)/(n_1 + n_2)$ and $q = (\mid m_1 - m_2 \mid)/(\mid n_1 - n_2 \mid)$.[11,12] A coupling between the 3/2, and the 4/3 modes maybe possible by the way of the observed $1/1$ mode, which has not been investigated in the present analysis.

Current driven disruptions have been suppressed in previous experiments in ohmically heated stellarator discharges.[13–15] In hybrid discharges of the W VII-A stellarator, which like CTH was an $\ell = 2$, five field-period current-carrying device, the low-q disruptions were suppressed with sufficient external rotational transform; in this case the stabilizing effect was observed for ι_{vac} between 0.14 and 0.17.[13] The MHD mode responsible for the disruption was primarily an $m/n = 2/1$, and even though a small amplitude 3/2 mode was observed, its

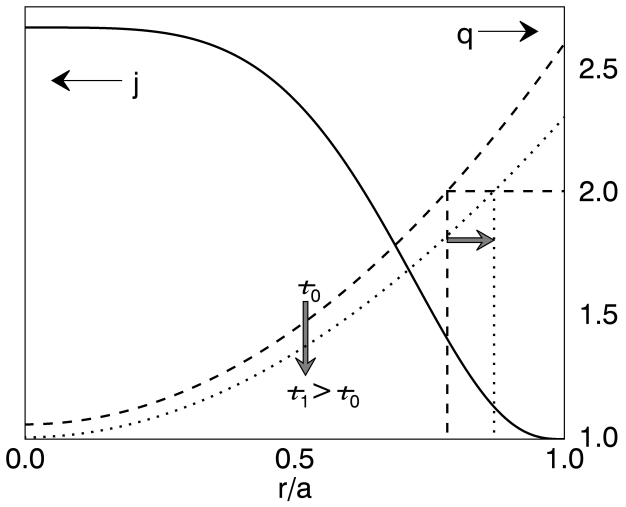

Figure 6.1: The effect of increasing vacuum transform is to shift the location of the $q = 2$ rational surface towards the edge, where the current density profile is less steep. Shown in the figure are the radial current density profile $j(r/a)$, and the profiles of edge safety factor, $q(r/a)$, for two different values of vacuum transforms, $\iota_{\rm vac} = \iota_0$ and $\iota_{\rm vac} = \iota_1 > \iota_0$.

role in disruption was not clear.[13] The reason for disruption suppression was conjectured to be a shifting of the resonant surface, in this case, the $q = 2$ surface, to a region of smaller current density gradient, as the vacuum transform is increased. This effect is illustrated in figure 6.1. Shown in figure 6.1 is the radial current density profile as a function of normalized plasma minor radius, $j(r/a)$, and the profiles of the edge safety factor, $q(r/a)$, for two different values of vacuum transforms, $\iota_{\rm vac} = \iota_0$ and $\iota_{\rm vac} = \iota_1 > \iota_0$. Recall that the edge safety factor has contributions from vacuum fields and the inductively driven plasma current, $\iota_{\rm tot} = \iota_{\rm vac} + \iota_{\rm p} = 1/q$. The profiles shown are arbitrary and are not related to either experiment or simulation; however, central and edge safety factors were chosen such that $q(r = 0) \sim 1$ and $q(a) < 2$, so that the illustration is consistent with observations of $q = 1$ in the core and the $q = 2$ surface internal to the plasma.[13] It can be seen from the figure that for a fixed radial current density profile, the effect of increasing the vacuum transform is to shift the $q = 2$ surface towards the edge of the plasma, where the current density profile is less steep; thereby increasing the stability of the equilibrium. A similar stabilization mechanism may be responsible for the disruption suppression observed in CTH plasmas. Numerical studies on the stability of kink and resistive tearing modes in a current-carrying

linear stellarator with an $\ell = 2$ helical field have been performed by Matsuoka.[16,17] That study showed an improvement in the MHD stability against kink and tearing modes with increasing levels of vacuum rotational transform when the total edge safety factor less than two, $q(a) < 2$.

6.2 Future work

In the analysis presented in chapter 4, we have established that the assumption of field aligned current perturbations is suitable for CTH plasmas. Our modeling is limited to rational flux surfaces being close to the LCFS whose shape and position are considered to be well known. This is because the equilibrium reconstructions are done only with external magnetic measurements which provide limited information about the internal rotational transform profile. Ongoing work of the CTH group to incorporate SXR[18,19] and Thomson scattering[20] data to better understand hybrid equilibria will improve the equilibrium reconstruction of CTH plasmas by incorporating the internal information. This will provide a better estimate of the current profile and thus the rotational transform profile. With this additional knowledge, it should be possible to obtain a current filament model simultaneously including more than one rational surface in the equilibrium. This should be a straight forward extension of the present analysis. The results could be compared with the non-dominant modes identified from biorthogonal decomposition, which at the moment are not considered as reliable in the absence of corroborating evidence. Additionally, one could apply the filament model to the measurements of fluctuations in the the radial magnetic field.

The mechanism for low edge safety factor disruptions was discussed earlier. It is possible that shifting of the rational surface to a location in the plasma with less steep current density gradient may be responsible for the observed low edge safety factor disruption suppression. At the moment no direct measurement of the current profile is available. To confirm this hypothesis of disruption mitigation it is essential to directly measure the current profile, either with diagnostics such as Hall probes, or derive it from equilibrium reconstructions

that use information from internal diagnostics. A periodic 1/1 mode is observed in SXR emission but a clear sawtoothing activity, which may aid in identifying central safety factor, $q(0)$, is not observed. This could be because the amplitude of the sawtooth oscillation is too small due to the low densities used in this dataset. Confirming the presence of the $q = 1$ surface by increasing the density, and/or the sensitivity of the SXR cameras, could help put a constraint on the equilibrium reconstructions,[18] thus giving a better estimate of current density profile. A correlation analysis of the 3/2, and 4/3 modes could also be investigated to determine if a coupling between these modes by the way of 1/1 mode.

An analysis technique to reconstruct observed MHD activity due to perturbed currents on a single rational surface has been developed in chapter 4. With improved understanding of the rotational transform profile, precise locations of the flux surfaces further inside the plasma could be obtained. Thus the structure of the perturbed currents on multiple rational surfaces, viz. $q = 3/2,\ 4/3$, could also be obtained. The model could then reconstruct the relative phase of the perturbed current distribution on these rational surfaces to determine any correlation between these disruption precursors.

References

[1] H. Zohm. *Magnetohydrodynamic Stability of Tokamaks*. Wiley, 2015.

[2] R.D. Hazeltine and J.D. Meiss, editors. *Plasma Confinement*. Dover Publications.

[3] M. J. Lanctot, H. Reimerdes, A. M. Garofalo, M. S. Chu, Y. Q. Liu, E. J. Strait, G. L. Jackson, R. J. La Haye, M. Okabayashi, T. H. Osborne, and M. J. Schaffer. Validation of the linear ideal magnetohydrodynamic model of three-dimensional tokamak equilibria. *Physics of Plasmas*, 17(3), 2010.

[4] DIVA Group. Very-low-q discharges in DIVA. *Nuclear Fusion*, 20(3):271, 1980.

[5] TFR Group. Low-Q MHD activity studies on TFR. *Nuclear Fusion*, 24(6):784, 1984.

[6] Pulsator Team. The pulsator tokamak. *Nuclear Fusion*, 25(9):1059, 1985.

[7] D.E. Roberts, D. Sherwell, J.D. Fletcher, G. Nothnagel, and J.A.M. de Villiers. Major disruptions induced by helical coils on the tokoloshe tokamak. *Nuclear Fusion*, 31(2):319, 1991.

[8] P Zanca, L Marrelli, R Paccagnella, A Soppelsa, M Baruzzo, T Bolzonella, G Marchiori, P Martin, and P Piovesan. Feedback control model of the m = 2, n = 1 resistive wall mode in a circular plasma. *Plasma Physics and Controlled Fusion*, 54(9):094004, 2012.

[9] P. Piovesan, J. M. Hanson, P. Martin, G. A. Navratil, F. Turco, J. Bialek, N. M. Ferraro, R. J. La Haye, M. J. Lanctot, M. Okabayashi, C. Paz-Soldan, E. J. Strait, A. D. Turnbull, P. Zanca, M. Baruzzo, T. Bolzonella, A. W. Hyatt, G. L. Jackson, L. Marrelli, L. Piron, and D. Shiraki. Tokamak operation with safety factor $q_{95} < 2$ via control of mhd stability. *Phys. Rev. Lett.*, 113:045003, Jul 2014.

[10] J. M. Hanson, J. M. Bialek, M. Baruzzo, T. Bolzonella, A. W. Hyatt, G. L. Jackson, J. King, R. J. La Haye, M. J. Lanctot, L. Marrelli, P. Martin, G. A. Navratil, M. Okabayashi, K. E. J.

Olofsson, C. Paz-Soldan, P. Piovesan, C. Piron, L. Piron, D. Shiraki, E. J. Strait, D. Terranova, F. Turco, A. D. Turnbull, and P. Zanca. Feedback-assisted extension of the tokamak operating space to low safety factor. *Physics of Plasmas*, 21(7):–, 2014.

[11] J. A. Holmes, B. A. Carreras, T. C. Hender, H. R. Hicks, V. E. Lynch, Z. G. An, and P. H. Diamond. Nonlinear interaction of tearing modes: A comparison between the tokamak and the reversed field pinch configurations. *Physics of Fluids*, 28(1):261–270, 1985.

[12] L H A Monteiro, M Y Kucinski, and I L Caldas. Coupling of modes in RFPs: an analytical approach. *Plasma Physics and Controlled Fusion*, 37(5):541, 1995.

[13] W VII-A Team. Stabilization of the (2, 1) tearing mode and of the current disruption in the W VII-A stellarator. *Nuclear Fusion*, 20(9):1093, 1980.

[14] J. Fujita, Kadota K. Itoh, S. and, K. Kawahata, Y. Kawasumi, O. Kaneko, T. Kuroda, K., K. Matsuura, K. Miyamoto, N. Noda, Y. Oka, K. Ohkubo, K. Sakurai, K. Sato, M. Sato, S. Tanahashi, Y. Terashima, and K. Toi. Confinement and additional heating (NBI and LHH) of stellarator plasma in JIPP T-II. *Proc. 8th Int. Conf. on Plasma Physics and Controlled Nuclear Fusion Research*, page 209, 1981.

[15] K. Toi, K. Sakurai, S. Tanahashi, and S. Yasue. Soft and hard major disruptions in profile control experiment of the JIPP T-II tokamak. *Nuclear Fusion*, 22(4):465, 1982.

[16] K. Matsuoka and K. Miyamoto. Stabilization of MHD-instabilities in a current-carrying stellarator. *Nuclear Fusion*, 19(6):837, 1979.

[17] K. Matsuoka, K. Miyamoto, K. Ohasa, and M. Wakatani. Magnetohydrodynamic instabilities in a current-carrying stellarator. *Nuclear Fusion*, 17(6):1123, 1977.

[18] X. Ma, D. A. Maurer, S. F. Knowlton, M. C. ArchMiller, M. R. Cianciosa, D. A. Ennis, J. D. Hanson, G. J. Hartwell, J. D. Hebert, J. L. Herfindal, M. D. Pandya, N. A. Roberds, and P. J. Traverso. Non-axisymmetric equilibrium reconstruction of a current-carrying stellarator using external magnetic and soft x-ray inversion radius measurements. *Physics of Plasmas*, 22(12), 2015.

[19] J. L. Herfindal, J. D. Dawson, D. A. Ennis, G. J. Hartwell, S. D. Loch, and D. A. Maurer. Design and initial operation of a two-color soft x-ray camera system on the compact toroidal hybrid experiment. *Review of Scientific Instruments*, 85(11), 2014.

[20] P. J. Traverso, D. A. Maurer, D. A. Ennis, G. J. Hartwell, M. M. Goforth, S. D. Loch, A. J. Pearce, and M. R. Cianciosa. Thomson scattering diagnostic system design for the compact toroidal hybrid experiment. *Review of Scientific Instruments*, 85(11), 2014.

Appendices

Appendix A

CTH coordinate system

The locations of the diagnostics installed on CTH are measured in the Cartesian coordinate system of a coordinate measuring machine (CMM), that is different from the CTH coordinate system. The relation between the CMM coordinate system and the Cartesian Coordinate system defined for CTH is given by the following set of equations:

$$\begin{aligned} x_{\mathrm{CTH}} &= x_{\mathrm{CMM}} \\ y_{\mathrm{CTH}} &= -z_{\mathrm{CMM}} \\ z_{\mathrm{CTH}} &= y_{\mathrm{CMM}} \end{aligned} \tag{A.1}$$

The subscripts for the CTH coordinates shall be dropped for the remainder of this Appendix. A top-view of the CTH laboratory indicating the local Cartesian coordinate system is shown in the figure A.1. The toroidal coordinate system is illustrated in the figure 1.1. The toroidal coordinate system are transformed to the CTH coordinates in the following manner:

$$\begin{aligned} x &= (R_0 + r\cos\theta)\cos\varphi, \\ y &= (R_0 + r\cos\theta)\sin\varphi, \\ z &= r\sin\theta, \end{aligned} \tag{A.2}$$

where, (x, y, z) are the CTH coordinates, $R_0 = 0.75$ is the major radius of the CTH vacuum vessel, r is the radial location with respect to the center for the poloidal cross-section, θ is the poloidal angle, and φ is the toroidal angle. The Z-axis is points out of the plane, while

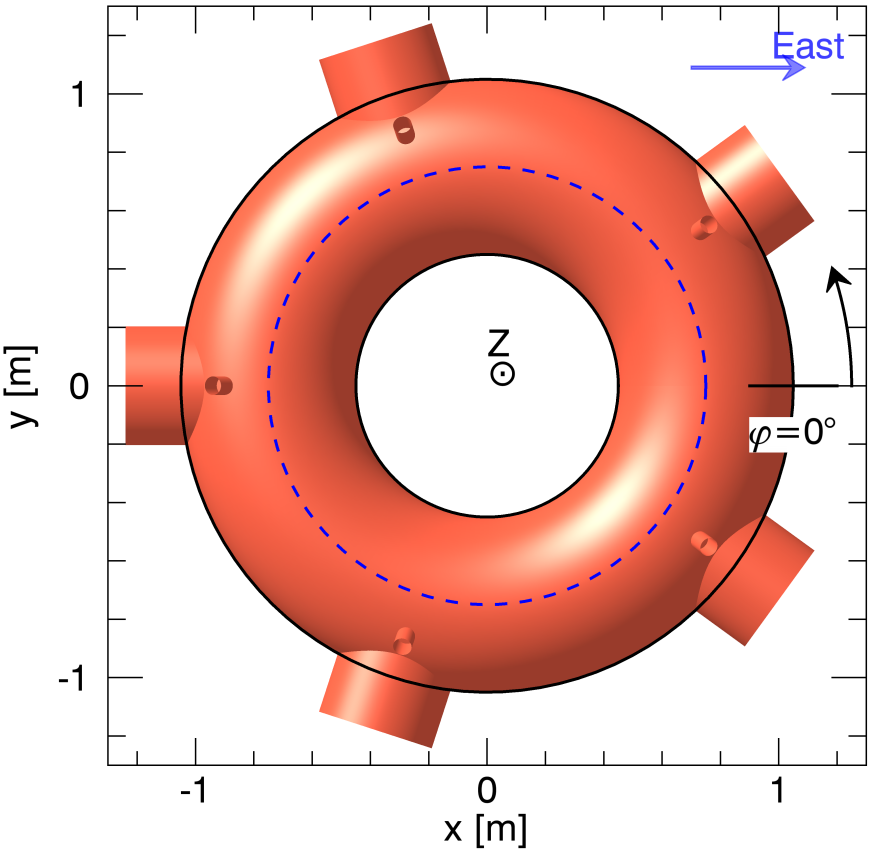

Figure A.1: The top-view of the CTH vacuum vessel is shown with its local Cartesian coordinate system. The Z-axis points out of the plane of the figure. The east wall of the laboratory is to the right in this schematic. Also shown is the $\varphi = 0°$ location with respect to the CTH vacuum vessel.

the vacuum vessel centered at $z = 0$, $\theta = 0$ at the outboard midplane and $\theta = \pm 180°$ at the inboard midplane.

Appendix B

Design and Calibration of the B-dot probes

Construction, assembly, and calibration of the poloidal array of B-dot probes located nominally at the toroidal angle of $\Phi = -117^\circ$ is presented in section 2.3.1. This array is composed of 36 probes that measure dB_θ/dt, 18 of which have dual windings that additionally measure the fluctuations in the radial magnetic field, dB_r/dt. An annotated photograph of the complete assembly is shown in the figure 2.10a. Appendix B.1 includes machine drawings for the following components of the assembly:

Fig. B.1: forms that were used to construct B-dot probes that measure B_θ;

Fig. B.2: forms that were used to construct B-dot probes that measure both B_θ, and B_r;

Fig. B.3: brackets that were built to mount the forms onto the frame;

Fig. B.4a: circular frame on which the poloidal array was assembled;

Fig. B.4b: limiters that were attached to this frame.

Section B.2 provides the following details of individual probes of the poloidal array and both the toroidal arrays:

1. measured sensitivity of the probes in terms of effective NA, where N is the number of turns of the wire, and A is the cross-section area;

2. measured position in toroidal coordinates (R, θ, Φ), which can be transform to the CTH coordinates using the set of equations given in appendix A, and the corresponding area-normals $(\hat{x}, \hat{y}, \hat{z})$.

The details of the way the B-dot probes are connected to feed-throughs on the vacuum vessel are given in appendix B.3 and the amplifier-filter circuitry is given in appendix B.4.

B.1 CAD designs

The B-dot probes are wound on circular cross-section forms machined out of Teflon. The CAD drawing for the form designed to measure the poloidal magnetic field is shown in the figure B.1. The form has dimensions, $1.3'' \times 0.5'' \times 0.5''$. The magnet wire is wound on the central part of the form $0.38''$ in diameter, and $0.78''$ in length. All the dimensions shown in the design are in inches. Additionally, there are two 4-40 tapped holes on both the ends along the axis of the form, which facilitate mounting these forms onto the motor used to wind the magnet wire on these forms. A vertical 4-40 tapped hole was made to hold the coil form onto a bracket, which was then mounted to the circular frame shown in figure B.4a.

The form used to wind the dual probes shown in figure B.2 is similar to the B_θ probe, with an additional notch along the horizontal direction to enable a rectangular winding for the B_r probe. The axis of this winding is orthogonal to the circular cross-section of the form.

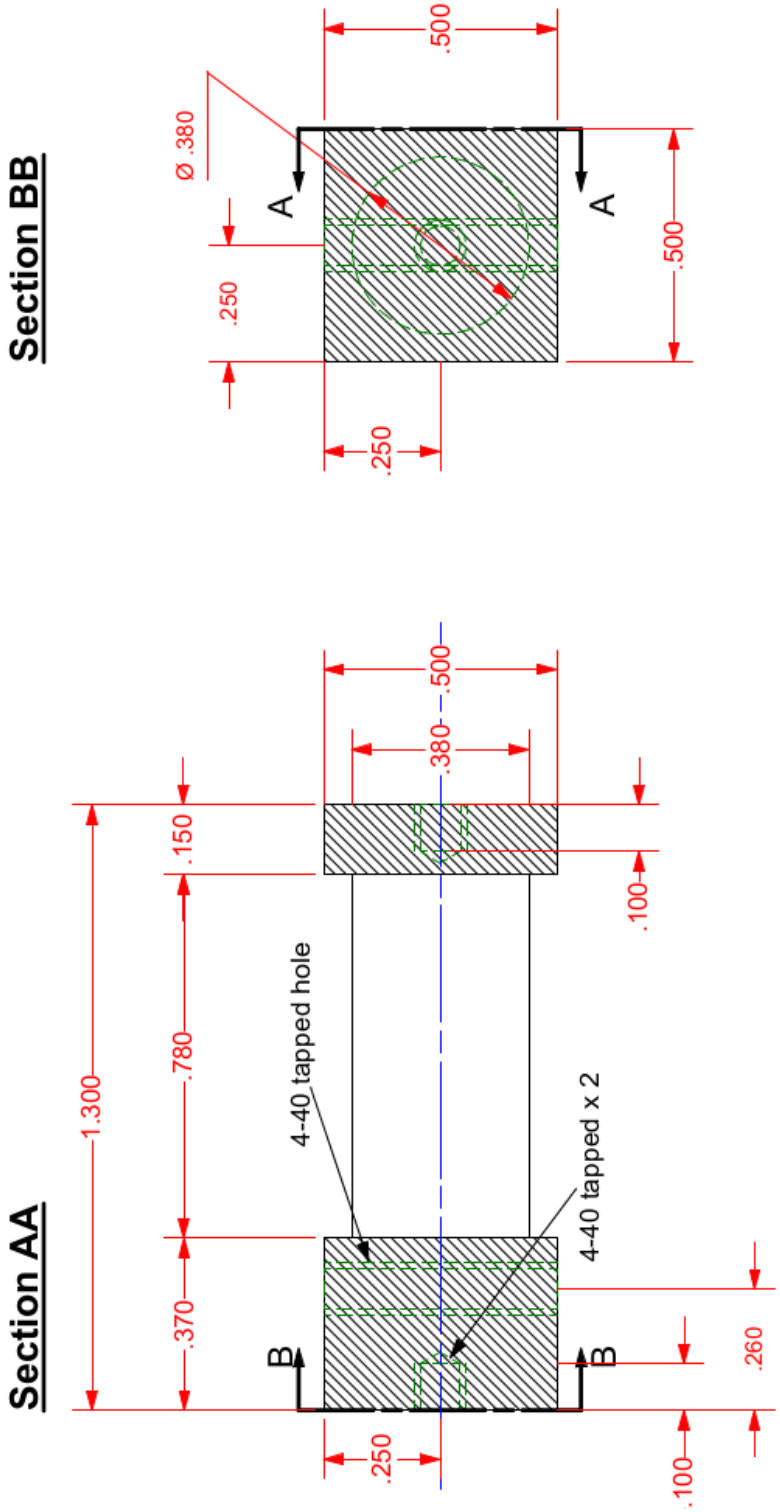

Figure B.1: B_θ probe design.

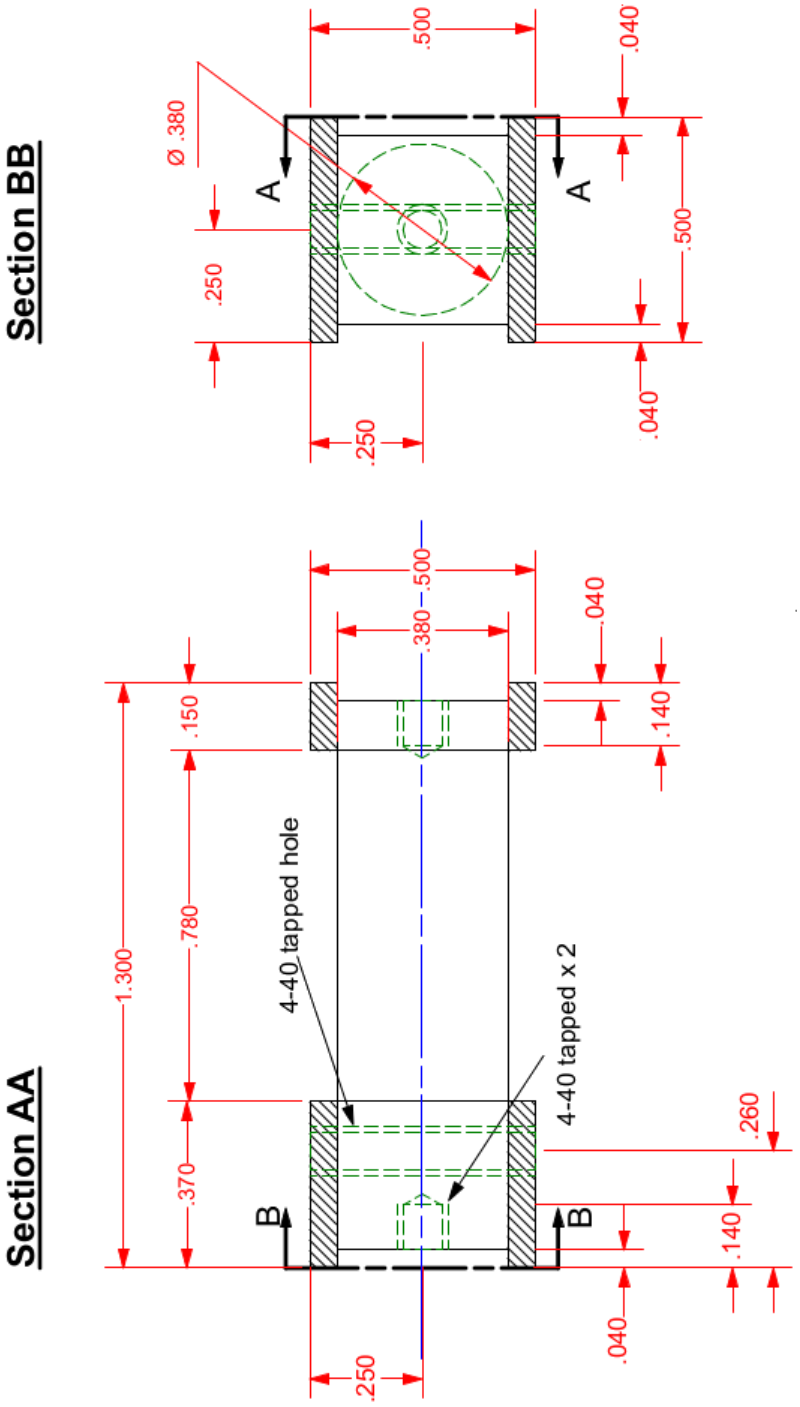

Figure B.2: Design of the dual probe that measures B_θ, and B_r.

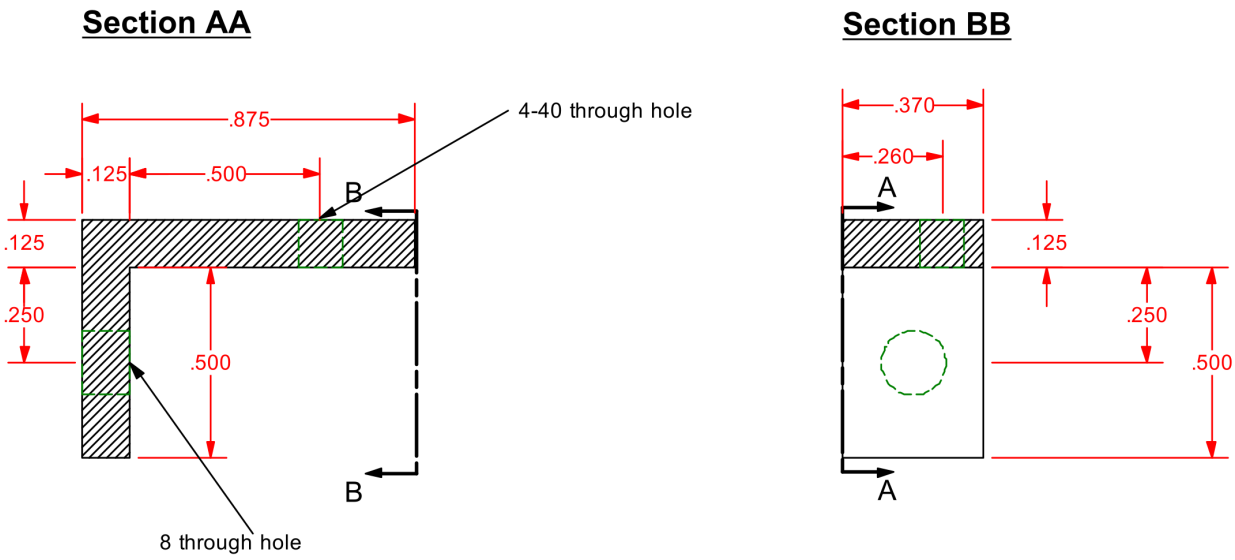

Figure B.3: Bracket made out of SS316 material was used to attach the forms to the circular frame.

B.2 Probe position and calibration data

The measured positions, and calibration information for the poloidal array located at the toroidal angle , $\Phi = -117°$, is given in the table B.1. The table lists toroidal coordinates, (R, θ, Φ), of the center of the wound portion of the coil forms previously shown. There are thirty-six probes in the array that measure B_θ, labeled, P01, ..., P36, placed 10° apart. Additionally, the direction of the axis is given in terms of unit vectors in CTH coordinates, $(\hat{x}, \hat{y}, \hat{z})$. The sensitivity of each probe is given in terms of measured effective NA in the units of cm^2; the negative sign of NA indicates that the polarity of the measured signal is to be switched to get the appropriate direction of the measured poloidal field. The measured output voltage of the probe can be converted into the units of magnetic field fluctuation, T/s, using the equation 2.3.

The table B.2 shows the position, and the calibration information for the toroidal array nominally located at $\theta = 90°$.

The 18 probes that measure the radial field, B_r were labeled with odd numbers, R01, R03, R05, ..., R35. The pair of B_θ and the B_r probes labeled with same number such as,

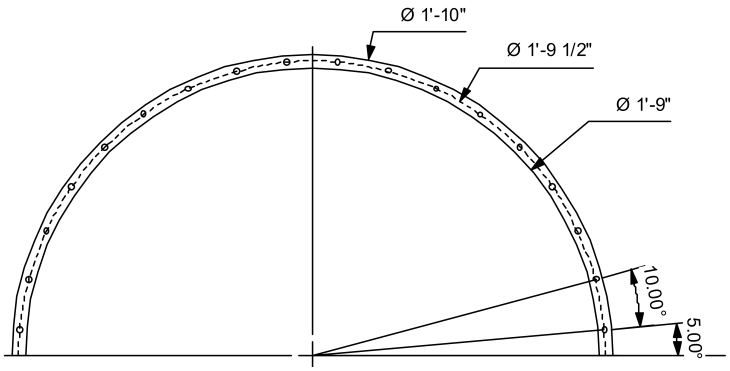

(a)

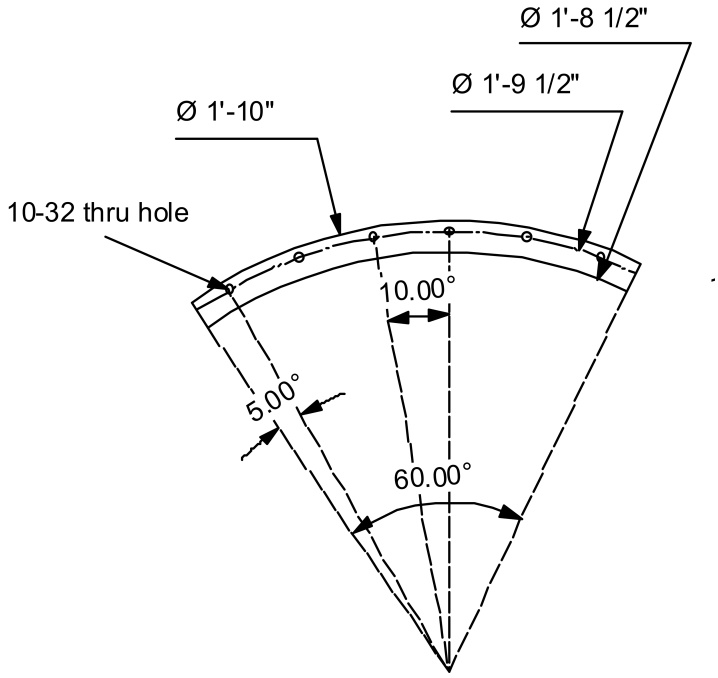

(b)

Figure B.4: (a) One half of the circular frame made out from SS316 material that was used to mount the poloidal array of B-dot probes. (b) The 3/16″ thick SS316 limiter was attached to a section of the circular frame. Six such limiters spanned the circular frame.

P01-R01, P03-R03, ..., P35-R35, were wound on the same coil form, the design of which is shown in the figure B.2.

Probe label	R [m]	θ [deg.]	Φ [deg.].	$\hat{x}$	$\hat{y}$	$\hat{z}$	$NA(cm^2)$
P01	0.810	76.919	-117.322	-0.447	-0.865	-0.226	-93.320
P02	0.764	86.985	-117.372	-0.459	-0.887	-0.053	-92.550
P03	0.717	97.201	-117.380	-0.456	-0.881	0.125	-92.460
P04	0.671	107.352	-117.365	-0.439	-0.848	0.298	92.490
P05	0.627	117.497	-117.436	-0.409	-0.787	0.462	91.250
P06	0.588	127.585	-117.531	-0.366	-0.703	0.610	93.100
P07	0.553	137.713	-117.561	-0.311	-0.596	0.740	-91.530
P08	0.524	147.812	-117.531	-0.246	-0.472	0.846	-92.980
P09	0.502	157.935	-117.417	-0.173	-0.333	0.927	-95.910
P10	0.488	167.985	-117.307	-0.095	-0.185	0.978	92.050
P11	0.482	177.749	-117.293	-0.018	-0.035	0.999	-95.310
P12	0.484	-172.309	-117.297	0.061	0.119	0.991	95.940
P13	0.493	-162.171	-117.317	0.141	0.272	0.952	91.420
P14	0.512	-152.057	-117.321	0.215	0.416	0.883	-92.500
P15	0.536	-142.066	-117.264	0.282	0.546	0.789	92.610
P16	0.569	-132.121	-117.217	0.339	0.660	0.671	-94.540
P17	0.605	-122.218	-117.233	0.387	0.752	0.533	92.400
P18	0.647	-112.295	-117.273	0.424	0.822	0.379	94.790
P19	0.692	-102.400	-117.314	0.448	0.868	0.215	95.000
P20	0.739	-92.384	-117.269	0.458	0.888	0.042	93.570
P21	0.786	-82.362	-117.208	0.453	0.881	-0.133	-94.340
P22	0.832	-72.440	-117.151	0.435	0.848	-0.302	-92.220
P23	0.876	-62.611	-117.115	0.405	0.790	-0.460	101.490
P24	0.914	-52.757	-117.093	0.363	0.709	-0.605	92.760
P25	0.950	-42.779	-117.082	0.309	0.605	-0.734	95.300
P26	0.978	-32.816	-117.070	0.247	0.483	-0.840	95.760
P27	1.000	-22.957	-117.001	0.177	0.348	-0.921	-93.970
P28	1.013	-13.133	-117.018	0.103	0.202	-0.974	92.130
P29	1.020	-3.482	-117.208	0.028	0.054	-0.998	-93.820
P30	1.018	7.144	-117.104	-0.057	-0.111	-0.992	-91.960
P31	1.008	17.562	-117.250	-0.138	-0.268	-0.953	-94.690
P32	0.989	27.645	-117.436	-0.214	-0.412	-0.886	-92.260
P33	0.965	37.184	-117.344	-0.278	-0.537	-0.797	-94.480
P34	0.934	46.758	-117.213	-0.333	-0.648	-0.685	91.630
P35	0.896	56.853	-117.206	-0.383	-0.745	-0.547	94.760
P36	0.855	66.930	-117.251	-0.421	-0.818	-0.392	92.840

Table B.1: Position and calibration information for the toroidal array of B-dot probes located nominally at $\Phi = -117°$.

Probe label	R [m]	θ [deg.]	Φ [deg.].	$\hat{x}$	$\hat{y}$	$\hat{z}$	$NA(cm^2)$
TA198T	0.764	87.137	-162.349	-0.966	-0.255	0.043	52.897
TA234T	0.736	92.912	-126.279	-0.532	-0.845	0.049	-48.575
TA270T	0.775	84.882	-89.275	-0.008	-1.000	-0.017	56.381
TA306T	0.737	92.599	-54.912	0.663	-0.748	-0.020	-56.749
TA342T	0.762	87.498	-17.542	0.955	-0.296	-0.029	53.165
TA018T	0.743	91.373	18.101	0.960	0.279	-0.028	52.260
TA054T	0.742	91.630	53.924	0.552	0.831	0.074	-51.322
TA090T	0.737	92.741	89.575	-0.091	0.994	0.062	-52.561
TA126T	0.765	86.870	126.079	-0.624	0.780	0.038	52.863
TA162T	0.732	93.799	161.801	-0.960	0.277	0.047	49.412

Table B.2: Position and calibration information for the toroidal array of B-dot probes located nominally at $\theta = 90°$.

B.3 Pin diagrams for connectors

The leads of the B-dot probes at the vacuum side are connected to a 4.5″ CF flange on the machine. This section describes how the poloidal array of B-dot porbes are connected to this flange. Three 4.5″ CF feed-through was sourced from the company Accu-Glass Products Inc, having model number *25D2-450*. Each flange has two male 25 pin sub-miniature D connections. Twisted pairs of the B-dot probes were connected to the feed-through using a vacuum compatible 25-pin female connector, that was sourced from the same company, model number *25D-PKS*. Since there are a total of 54 probes in the poloidal array, these connections were made on 6 such CF flanges. Figure B.5 shows the vacuum side view of one such connector with pin-labels 1 through 25. The pin-connections corresponding to each probe are listed in the table B.3.

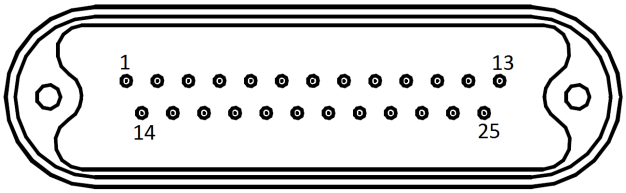

Figure B.5: Vacuum side view of a 25-pin sub-miniature D connector. Pins in the top row are labeled 1 through 13, and the ones in the bottom row are labeled 14 through 25.

Pin #	Sub-D connectors for B_θ probes			Sub-D connectors for B_r probes	
	C2-Poloidal	C4-Poloidal	C6-Poloidal	C1-Radial	C3-Radial
1,2	P01	P13	P25	R01	R19
3,4	P02	P14	P26	R03	R21
5,6	P03	P15	P27	R05	R23
7,8	P04	P16	P28	R07	R25
9,10	P05	P17	P29	R09	R27
11,12	P06	P18	P30	R11	R29
13	-	-	-	-	-
14,15	P07	P19	P31	R13	R31
16,17	P08	P20	P32	R15	R33
18,19	P09	P21	P33	R17	R35
20,21	P10	P22	P34	-	-
22,23	P11	P23	P35	-	-
24,25	P12	P24	P36	-	-

Table B.3: The poloidal array contains 54 probes out of which, 36 probes that measure B_θ use connectors labeled, C2-Poloidal, C4-Poloidal, and C6-Poloidal. The 18 probes that measure B_r use connectors labeled C1-Radial, and C5-Radial. The details of pin assignment for each B-dot probe is listed in this table.

B.4 Amplifier circuitry

The voltage output between the twisted pair of each B-dot probe is connected to an amplifier box which then connects to the data acquisition (DAQ) system in the CTH laboratory as shown in the schematic diagram in the figure B.6. Each subminiature-D (sub-D) connector has 12 twisted pairs connected on the vacuum side of the CF flange. On the air-side, a 12-pair twisted shielded cable connects to the amplifier box, the output of which is connected to the SCSI input of the DAQ system. The amplifier circuitry, shown in figure B.7a, consists of an instrumentation amplifier, *INA03*, manufactured by Texas Instruments, designed for low impedance loads such as our B-dot probes. The pin connections for the amplifier are shown in the figure. The output of the amplifier circuit is connected to a filter circuit shown in the figure B.7b. The filter circuit uses the operational amplifier, NE5532, also manufactured by Texas Instruments. The two operational amplifiers on the chip form a two-pole Sallen-Key Butterworth filter configuration designed to provide a flat response

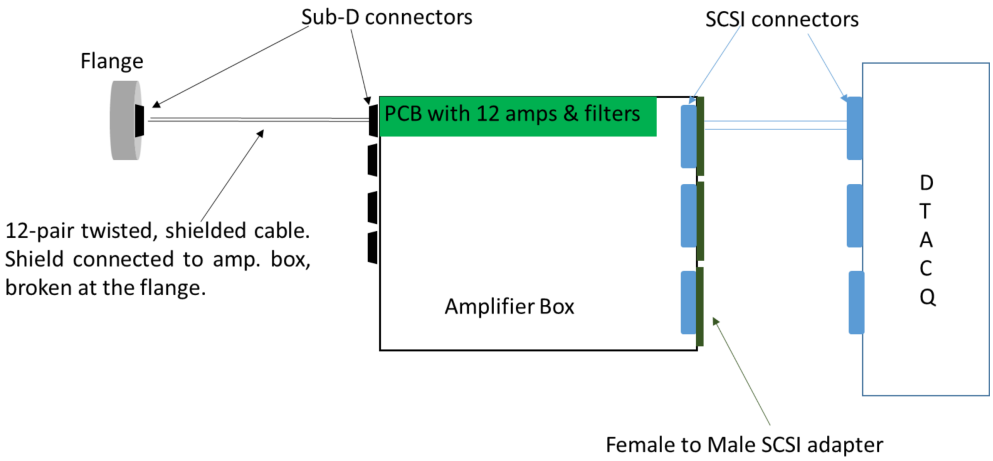

Figure B.6: This schematic shows how output voltage from the B-dot probes is transferred to the data acquisition (DAQ) system.

up to a frequency of $50kHz$. The measured gain, and frequency response of the amplifying circuit is shown in the figure 2.11.

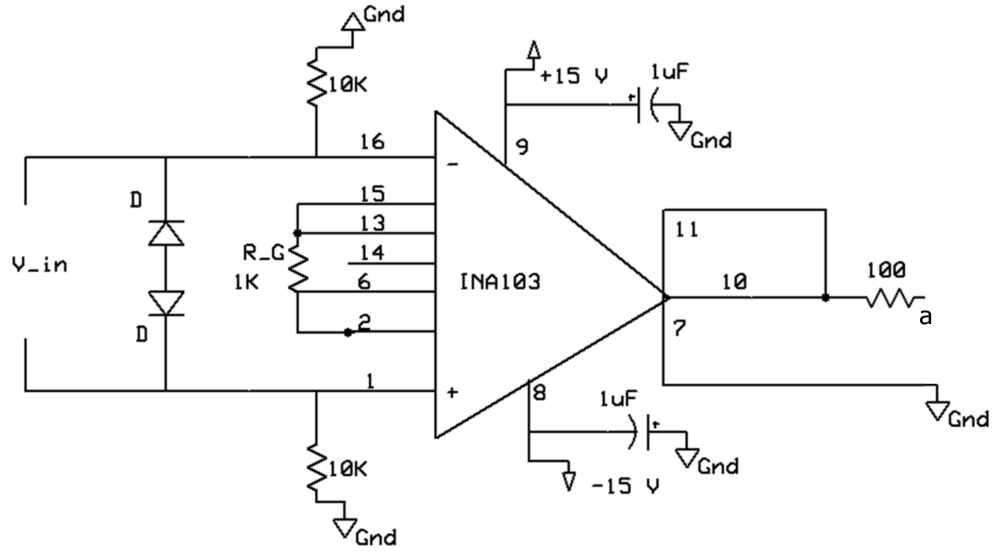

(a)

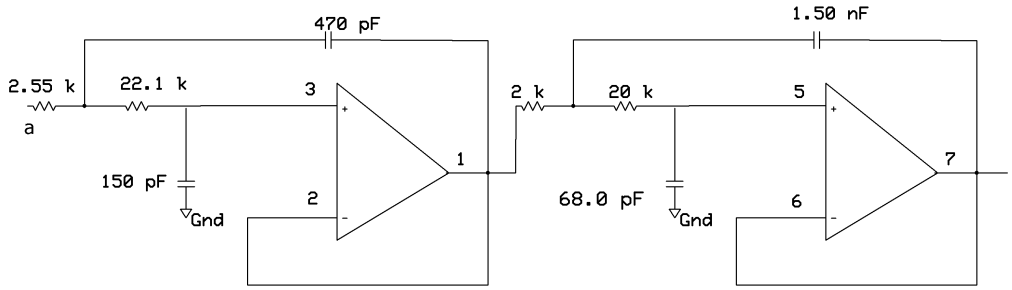

(b)

Figure B.7: (a) The output of the B-dot probes is connected to an instrumentation amplifier. (b) The output of the amplifying circuit is connected to a filter circuit shown in the figure.

Appendix C

V3RFUN input files

V3RFUN is used to compute the mutual inductances between the B-dot probes and the current filaments in section 4.3. It is also used to compute mutual inductances between the CTH magnet coils such as the HF, TVF, TF, SVF, etc. and the B-dot probes installed in CTH, which are described in appendix D. The goal here is to describe the format of the input files required to execute the V3RFUN code and give some example files used in the actual computation.

V3RFUN execution requires three input files: A *namelist* input file, which contains a set of input variables to the code, the *diagnostic_dot* file which contains descriptions of the diagnostic coils, with the name of the file specified as a variable in the *namelist* file, and the *coils_dot* file which contains descriptions of the field coils and is also specified as a variable in the *namelist* file. A sample of input files used in this example are given in appendix C. The Cartesian coordinates of points along the path of the current filaments are specified in the *coils_dot* file. The position of the B-dot probes and their area-normals are supplied via the *diagnostic_dot* file. The sample files used in the execution of the V3RFUN code for the analysis presented in chapter 4 are placed on CTH share drive as detailed in the following:

V3RFUN Documentation: This file contains Cartesian coordinates for 36 current-carrying filaments placed on the rational flux surface initialized on a poloidal cross-section. The magnetic field lines return to their starting location after making three toroidal circuits.

Path: `Z:\_Users\Mihir\public\v3rfun_inputfiles\Currentfilament_coilsdot\fil_coilsdot_140214733_32mode.dot`

Diagnostics_dot file for CTH B-dot probes: This file contains the location and the normals for the B-dot probes used in simulations presented in chapter 4.

Path: `Z:\_Users\Mihir\public\v3rfun_inputfiles\Bdotprobes_diagnosticsdot\bdot_diagdot`

Coils_dot file for current filaments on $m = 3/n = 2$ rational surface: This file contains Cartesian coordinates for the 36 current-carrying filaments placed on the rational flux surface initialized on a poloidal cross-section. The magnetic field lines return to their starting location after making three toroidal circuits.

Path: `Z:\_Users\Mihir\public\v3rfun_inputfiles\Currentfilament_coilsdot\fil_coilsdot_140214733_32mode.dot`

Coils_dot file for CTH magnet coils: This file contains the Cartesian coordinates for all the magnet coils on CTH. This file along with the *diagnostics_dot* file mentioned above is used to compute the mutual inductance between the B-dot probes and the CTH magnet coils shown in appendix D.

Path: `Z:\_Users\Mihir\public\v3rfun_inputfiles\CTHcoilsdot\coils.cth.18b.mo.f5sa`

Appendix D

Mutual inductances between the B-dot probes and the magnet coils

The B-dot probes described in this dissertation are used to make local measurements of the fluctuating component of the poloidal magnetic field, δB_θ, and to model the fluctuations in the equilibrium poloidal magnetic field modeled by current filaments superimposed within a reconstructed equilibrium, as presented in chapter 4. The determination of the poloidal magnetic field due to the current filaments requires accurate knowledge of the calibration, location, and orientation of these probes inside the vacuum vessel. A comparison of measured and computed mutual inductances between the B-dot probes and the magnet coils such as the HF, TVF, TF, etc. helps determine the accuracy of the known properties of the B-dot probes. Experimentally, this mutual inductance between a magnetic coil and the B-dot probes is determined by measuring the magnetic field at the location of the coil generated by a known current in the magnet coil, while open circuiting the other magnet coils. The V3RFUN code, described in chapter 4 uses the known information of the B-dot probes to compute mutual inductance with the magnet coil. This procedure is outlined in detail in previous work done to optimize the calibration of the Rogowski coils used in equilibrium measurement.[1]

This appendix presents a comparison of measured and computed mutual inductances between the B-dot probes and the HF, TVF, TF, and SVF. The mutual inductances for the B-dot probes in the poloidal array and the toroidal arrays are shown in figures D.1 and D.2 respectively.

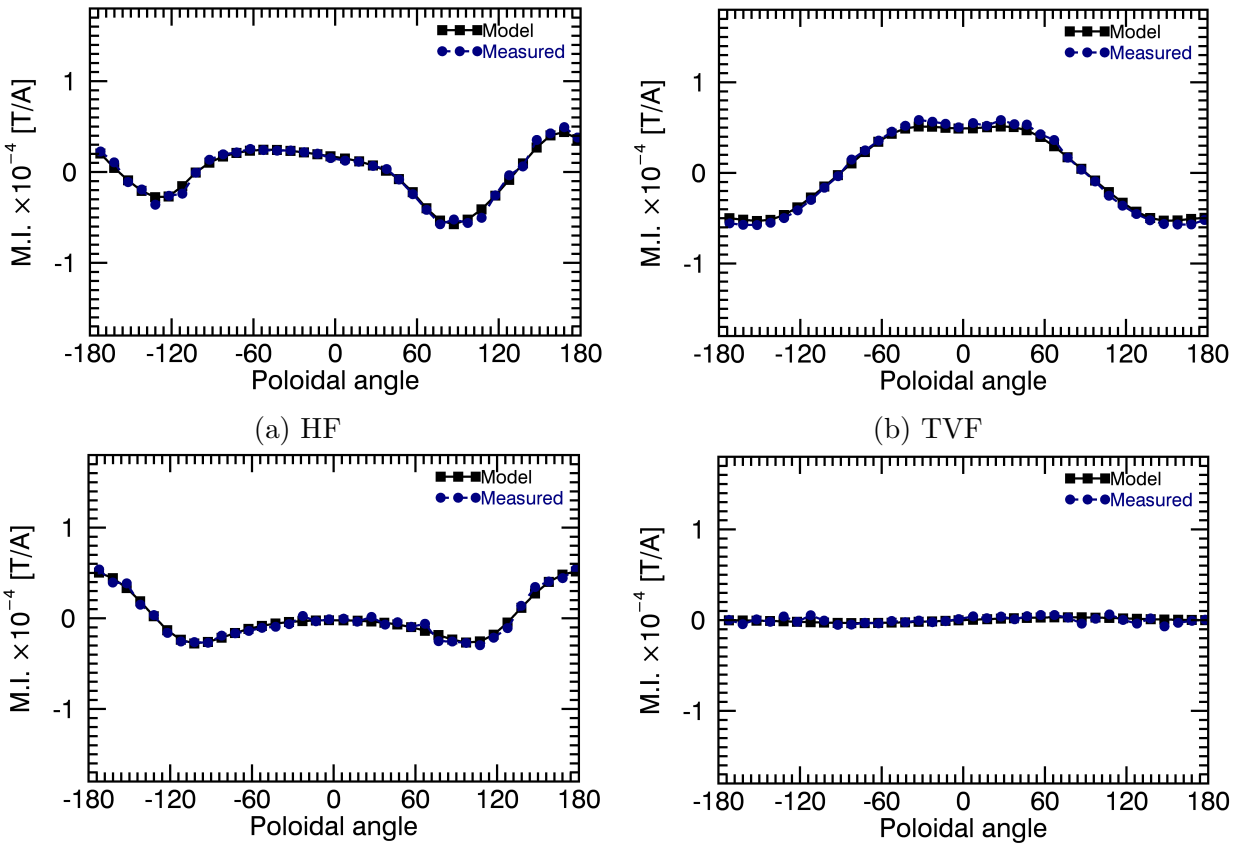

(a) HF

(b) TVF

(c) SVF

(d) TF

Figure D.1: The mutual inductances between the B-dot probes in the poloidal array and the magnet coils, (a) HF, (b) TVF, (c) TF, and (d) TF are shown. The black squares represent the measured values of the mutual inductances, while the blue circles represent the computed values.

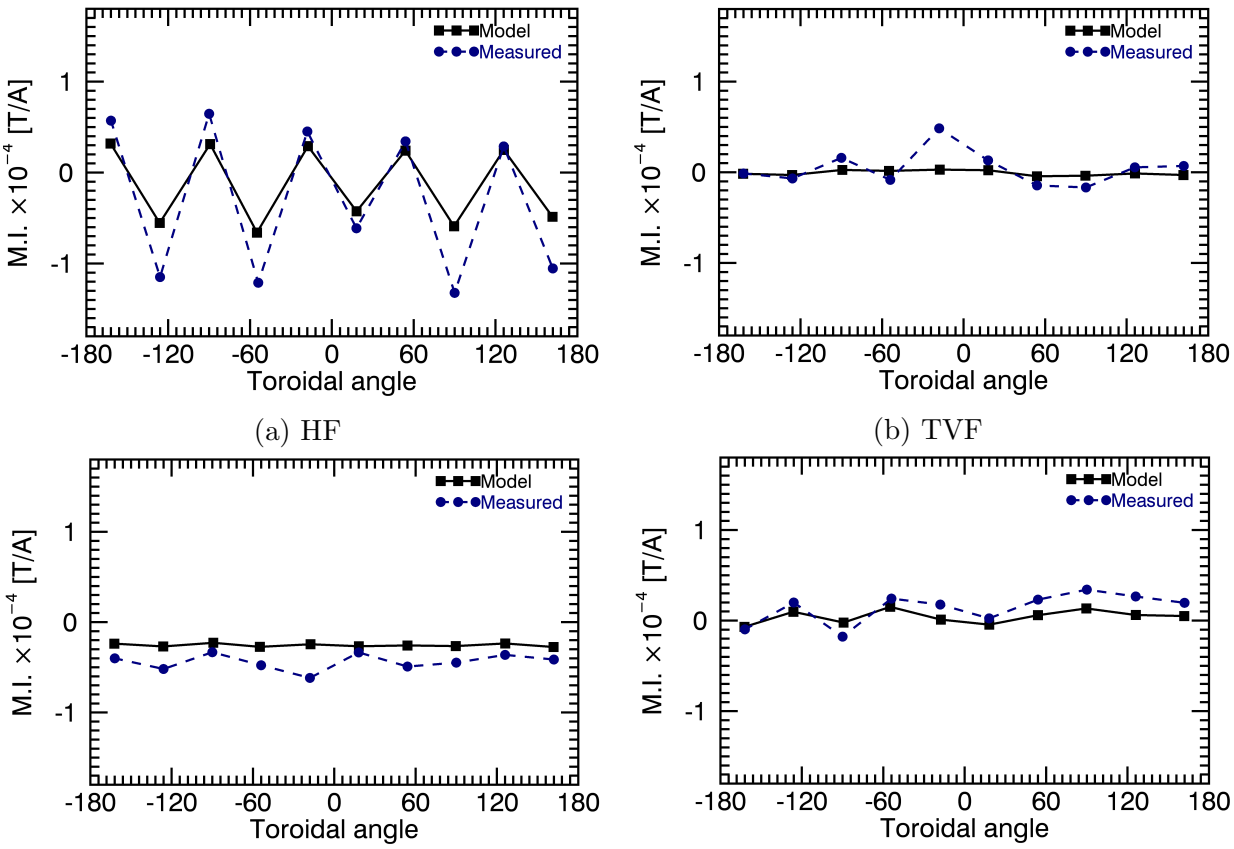

(a) HF

(b) TVF

(c) SVF

(d) TF

Figure D.2: The mutual inductances between the B-dot probes in the toroidal array and the magnet coils, (a) HF, (b) TVF, (c) TF, and (d) TF are shown. The black squares represent the measured values of the mutual inductances, while the blue circles represent the computed values.

References

[1] B. A. Stevenson. *3D Reconstruction of Plasma Equilibria using Magnetic Diagnostics on the Compact Toroidal Hybrid*. PhD thesis, Auburn University, 2011.

Appendix E

H_α detector array

A seven-chord array of H_α detectors has been installed to view a poloidal cross-section of the plasma. Each H_α detector assembly consists of collection optics, filter optics, and amplifying circuitry. The collection optics are mounted on 2.75 in windows as shown in the photograph in figure E.1 . Unfiltered light from the plasma is focused onto an optical fiber in the collection assembly and is coupled to the filter optics that collimate the light onto an interference filter. The filtered light is focused onto a photo-diode detector and the resulting signal is amplified and digitized. The signal from the midplane H_α chord is shown in figure E.2a. The initial spike at 1.6 s corresponds to the beginning of the ECRH phase of the discharge and a second increase at 1.62 s occurs when the ohmic system is discharged. A contour plot of all seven H_α channels in E.2b shows the emission is updown symmetric until well into the shot when the plasma drifts upward.

The line of sight of each detector is constrained in the poloidal and toroidal directions by a rectangular slit installed on the vacuum side of the flange, 0.75″ wide and 0.375″ tall. The collection optics consists of a one inch diameter plano-convex lens that focuses the H_α emission onto an optical fiber which carries the light to the optical filter assembly. The optical filter assembly consists of one collimating lens, one interferences filter, and one focusing lens, in that order. The focused light is collected by the active area of the photodiode positioned at the focal length of the focusing lens in the filter assembly. The collection and the filter optics are held within custom-designed holders made out of black Delrin; their assembly is shown in figure E.3. The machine design for individual components is shown in figures E.4a and E.4b. The details of the components used in each channel of the H_α detector are listed in table E.1.

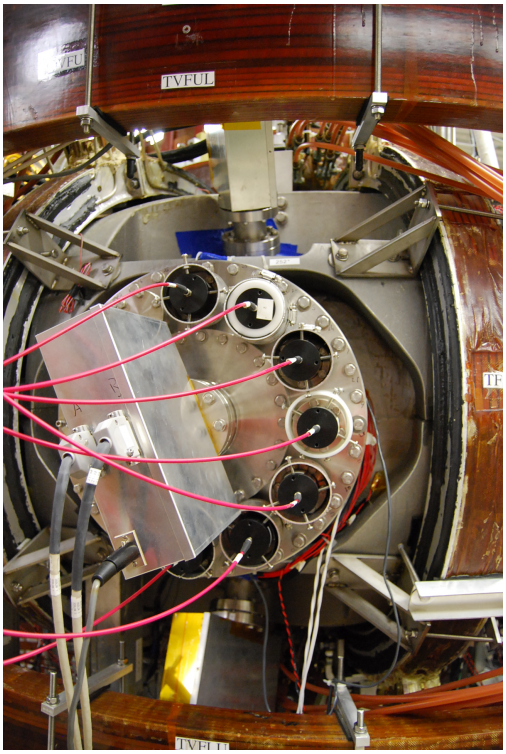

Figure E.1: The photograph shows collection optics of the seven channel H_α detector array installed at a horizontal port on CTH. The collection optics for each channel consists of a set of seven plano-convex lenses held within custom-made holders made out of black Delrin. Optical fibers transport the light to the filter optics.

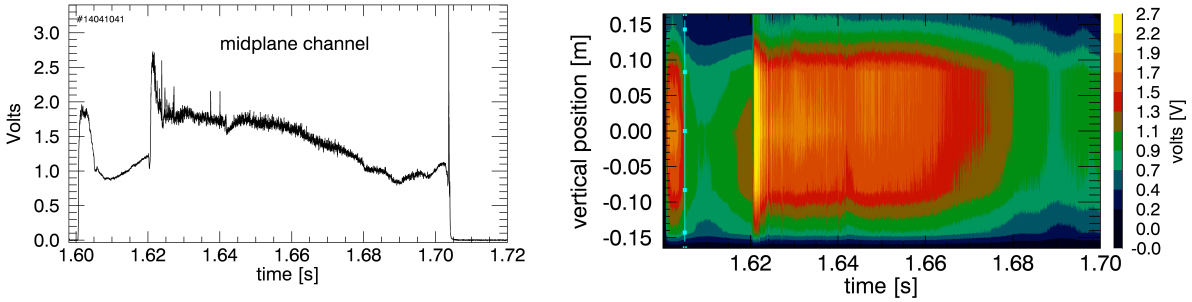

(a) (b)

Figure E.2: (a) The signal during an ohmic CTH discharge as measured by the mid-plane channel is shown in the figure. The ECRH phase of the discharge is recognized by a breakdown spike at 1.6 s, while the ohmic phase can be seen by another voltage spike at approximately 1.62 s. (b) The contour plot shows signals measured by all the seven channels of the detector. The mid-plane channel measures H_α signal along a horizontal line of sight at $y = 0$ m. The vertical positions of the other chords are indicated by blue squares.

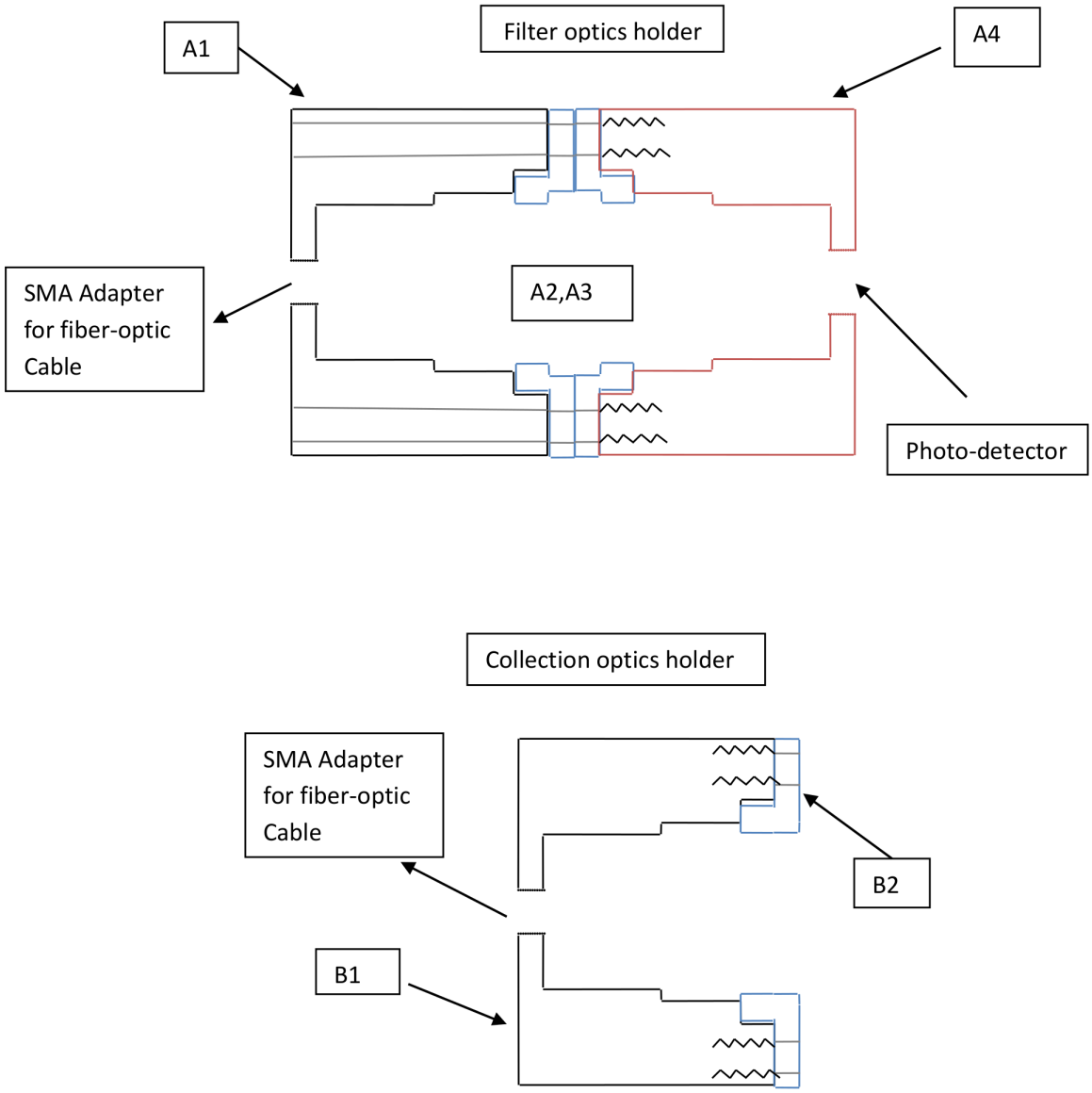

Figure E.3: The assembly of custom designed holders for the collection and filter optics is shown in this figure. The lens held within the collection holder, B1, focuses the light onto the optical fiber, that connects to the fiber optics holder. The component labeled A1 holds the collimating lens; and the interference filter is held sandwiched between the components A2, and A3; the focusing lens A4 focuses the light onto a photodetector.

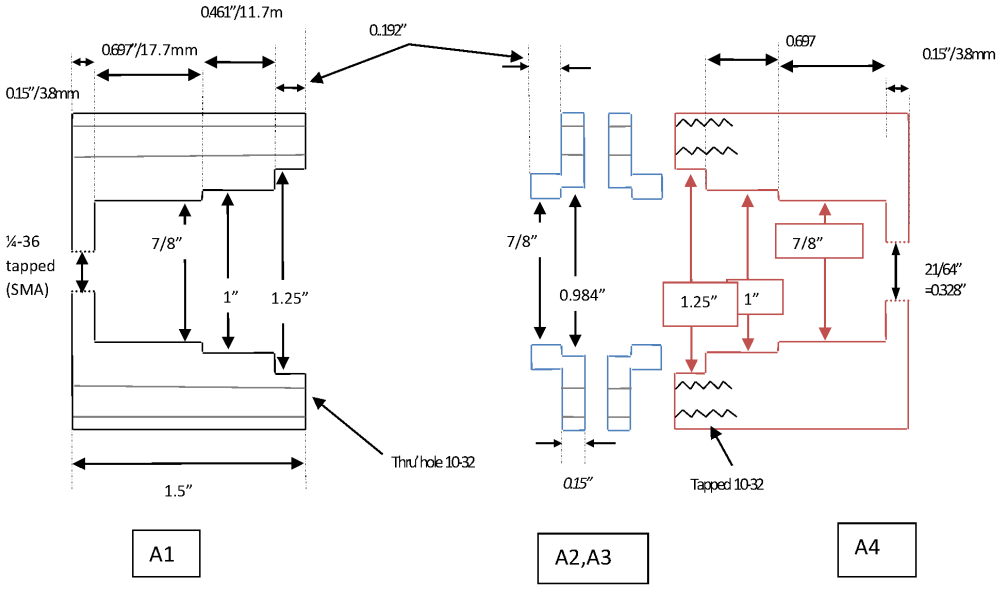

(a)

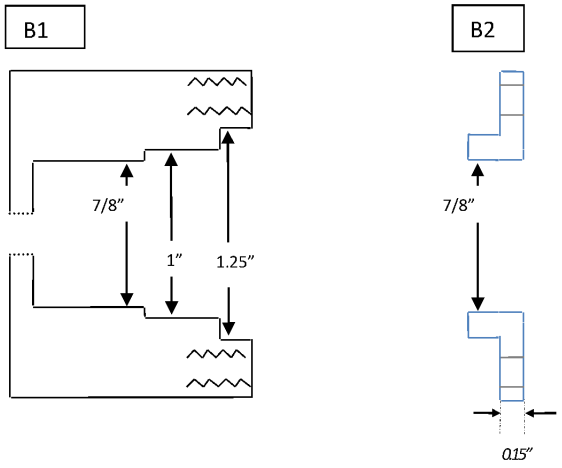

(b)

Figure E.4: The design specifications of the optics holders for (a) filter optics, and (b) collection optics are shown in this figure. The dimensions of the components are decided keeping in mind the focal lengths of the lenses used. Note that the components A1 and B1 are identical.

Component	Specification
Optical fiber (1 nos.)	Numerical aperture:0.39 Diameter: 1000 μm, Part number: FMT1000UMT, Thorlabs Inc.,
Plano-Convex Lenses (3 nos.)	Diameter: $D = 25.4$ mm, focal length,$f = 25.4$ mm, material: N-BK7, part number: LA1951, Thorlabs, Inc.
Interference filter (1 nos.)	Mounted diameter: $D = 25.0$ mm, clear aperture: 21 mm, Central wavelength (CWL): 656 nm, FWHM:10 nm , transmission: $\geq 50\%$, part number: NT65-716, Edmund Optics
Photo-diode with inbuilt amplifier (1 nos.)	Responsivity: 0.4 Amps/Watt, Active area: 2.54 mm, part number:SD 100-41-21-23, Advanced Photonix Inc.

Table E.1: Specifications of various components used in each detector

The trans-impedance amplifier circuit converts the output of the photodiode in the units of current to a voltage which is recorded by the data acquisition system. The amplifying circuitry is shown in the figures E.5

A relative calibration was performed using a hydrogen gas discharge lamp for each H_α channel, which includes the collection optics, optical fiber, filter optics, and the photodetector circuitry. The calibration data relative to channel number 2 is given in table E.2.

H_α channel	Relative calibration
1	0.993
2	1.000
3	0.954
4	0.947
5	0.826
6	0.677
7	0.915

Table E.2: Relative calibration of the H_α detector channels

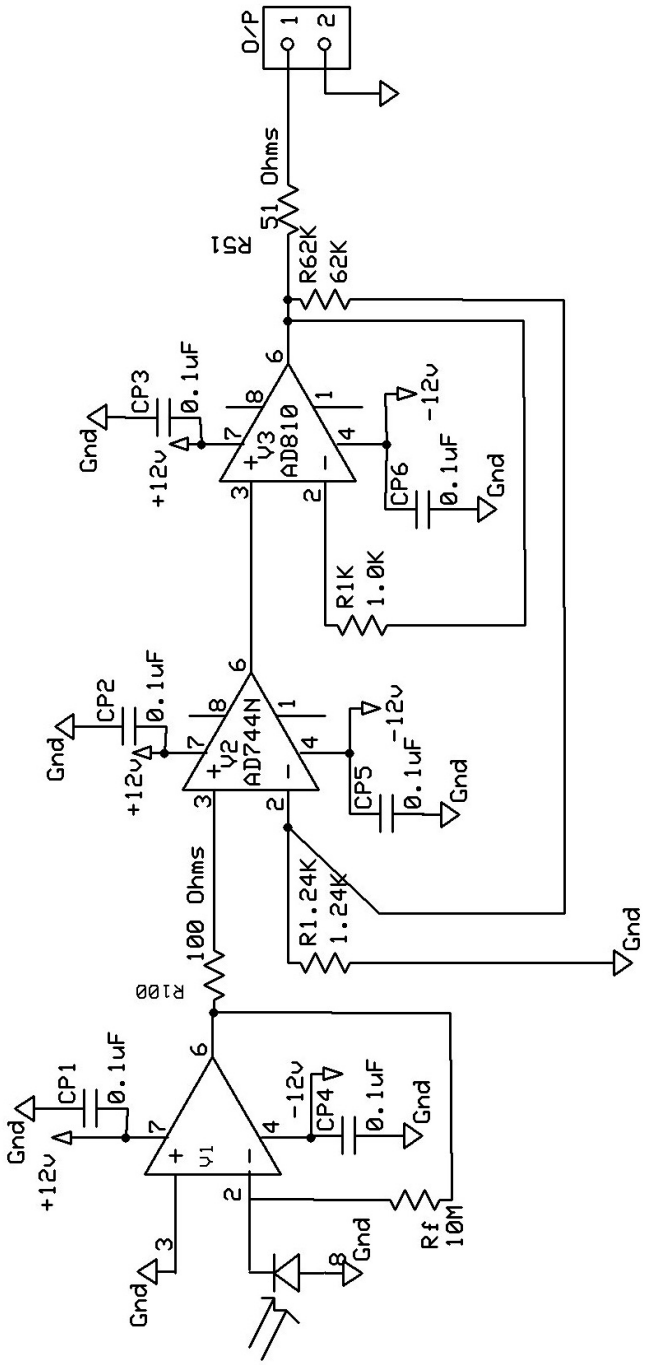

Figure E.5: The photodiode-amplifier circuit which was used for each H_α detector is shown in this figure. The light incident on the photodiode is indicated on the left, while the built-in operational amplifier is labeled V1. Amplification is done in two more stages, indicated by V2, and V3.